Summer 2019

Synthesis of Amorphous Hydrogenated Boron Carbide from Orthocarborane Using Argon Bombardment: A Reaxff Molecular Dynamics Study

Nirmal Baishnab
Missouri State University, Nirmal098@live.missouristate.edu

Follow this and additional works at: https://bearworks.missouristate.edu/theses

Part of the Ceramic Materials Commons, and the Structural Materials Commons

Recommended Citation

SYNTHESIS OF AMORPHOUS HYDROGENATED BORON CARBIDE FROM

ORTHOCARBORANE USING ARGON BOMBARDMENT: A REAXFF

MOLECULAR DYNAMICS STUDY

A Master's Thesis

Presented to

The Graduate College of

Missouri State University

In Partial Fulfillment

Of the Requirements for the Degree

Master of Science, Materials Science

By

Nirmal Baishnab

August 2019

SYNTHESIS OF AMORPHOUS HYDROGENATED BORON CARBIDE FROM

ORTHOCARBORANE USING ARGON BOMBARDMENT: A REAXFF MOLECULAR

DYNAMICS STUDY

Physics, Astronomy and Materials Science

Missouri State University, August 2019

Master of Science

Nirmal Baishnab

ABSTRACT

In this study, the synthesis process of a-$B_xC:H_y$ using argon bombardment from the orthocarborane precursor was modeled by using reactive molecular dynamics (MD). Utilizing the MD simulations, the formation of free radicals as a result of ion bombardment was identified and quantified. Then, the densification process that is aided by the mixture of free radicals and orthocarborane was analyzed. The densification process by creating the initial structure composed of free radicals and orthocarborane with active sites created by partially removing some of the hydrogen atoms from the icosahedral cage was also modelled. Overall, a better understanding of the mechanism of the densification of hydrogenated boron carbide and the roles of Ar bombardment and radical species toward the deposition process were obtained.

SYNTHESIS OF AMORPHOUS HYDROGENATED BORON CARBIDE

FROM ORTHOCARBORANE USING ARGON BOMBARDMENT: A

REAXFF MOLECULAR DYNAMICS STUDY

By

Nirmal Baishnab

A Master's Thesis
Submitted to the Graduate College
Of Missouri State University
In Partial Fulfillment of the Requirements
For the Degree of Master of Science, Materials Science

August 2019

Approved:

Ridwan Sakidja, Ph.D., Thesis Committee Chair

Kartik C. Ghosh, Ph.D., Committee Member

Tiglet Besara, Ph.D., Committee Member

Julie Masterson, Ph.D., Dean of the Graduate College

ACKNOWLEDGEMENTS

I dedicate this thesis to my mother Varasha Rani.

TABLE OF CONTENTS

LIST OF TABLES

LIST OF FIGURES

INTRODUCTION

Boron Carbide

Ceramics like boron carbide, silicon carbide, and alumina have numerous potential useful applications. Compared to metals these ceramics possess greater strength. Boron carbide, in particular, is the third hardest material found in nature, following only diamond and cubic boron nitride [1]. Its extreme hardness and very low density make it an ideal material where weight and strength come into consideration. In addition, it has high chemical and thermal stability, high melting temperature (above 2500K) [1] and high abrasion resistance. These novel properties have made it widely useful for armor making and abrasion. Boron-10 has a high cross section for neutron absorption and, consequently, boron carbide is useful in neutron detection and nuclear reactors [2], [3]. Thin-film boron carbide has become a candidate material for intra/interlayer dielectrics [4] and for semi-insulating nano-electronics for neutron detectors [2], [5] due to a bandgap range from 2 to 4 eV. It also has potential applications in specialized coating using ion beam deposition, pulsed DC magnetron sputtering, and more [6]–[9].

A wide variety of growth techniques have been developed to synthesize boron carbide-based solids [1], [10], such as sintering, hot isostatic pressing, and hot pressed pellet [11]–[13]. These techniques involve high temperatures and are typically used to produce B_4C for popular applications such as armor and abrasives. However, applying these bulk growth techniques in semiconductor device applications exhibits a lower tenability and is prone to yield undesirable electronic properties [14], [15]. Chemical vapor deposition (CVD) or physical vapor deposition techniques have been found useful in the production of B_xC thin films that have similar mechanical, thermal and chemical properties to bulk production, while also having improved

1

electronic properties [16]–[20] with tunability. In particular, thin films derived from

orthocarborane (o-$C_2B_{10}H_{12}$) using plasma-enhanced chemical vapor deposition (PECVD)

technique have demonstrated promising properties for device applications with wide-range

tunability [21]–[26]. This particular approach usually produces amorphous hydrogenated boron

carbide (a-$B_xC:H_y$) which is comparatively new in the field of electronics materials. In thin films

of a-$B_xC:H_y$ electronic, optical, chemical and mechanical properties have been extensively

investigated, particularly the hydrogen influence on these properties in Nordell et al [27].

Crystal Structure. Boron-rich materials have a characteristic icosahedron crystal

structure. In geometry, a polyhedron with 20 faces is called icosahedron. One icosahedron has 20

equilateral triangles and 30 edges, with 5 faces coming to a point at each of the 12 vertices. The

geometry of a regular icosahedron is shown in figure 1.
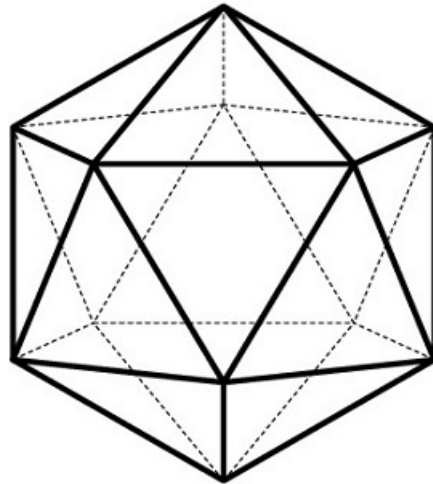
Figure 1. Geometry of a regular icosahedron

The B-B and B-C bonds in boron carbide play the decisive role for the physical and

properties and crystal structure of the material. Boron carbide can exist as a variety of

compositions of boron and carbon. From $B_{10.4}C$ (8.8 at.-%C) to B_4C (20 at.-%C) it exists as the rhombohedral phase [1], [10]. The amount of carbon in the crystal plays an important role in the properties of the material. Among different types of boron carbide, B_4C exhibits greater hardness and thermal properties. The most common crystal structure of boron carbide is a rhombohedral unit cell ($R\overline{3}m$ space group). In each corner, there is a 12-atom icosahedron, connected by 3-atom chains in the longest diagonal. The first and third atoms of the chain are each connected to three different icosahedra. The icosahedron typically consists of 11 boron and 1 carbon atoms ($B_{11}C$) or 12 boron atoms (B_{12}). Both B-B and B-C bonds are covalent, and due to the valence electron deficiency of boron, the structure exhibits the formation of icosahedral configuration. In a single icosahedron, there are 6 polar sites, 3 in each opposite end and 6 equatorial sites between them. The atoms in the polar sites are directly bonded with a two-center bond to the neighboring icosahedra parallel to the cell edge. The equatorial atoms can be connected in two ways: directly to the neighboring icosahedra or to the chains. For $B_{11}C$, the carbon atoms remain mostly in the polar sites. For $B_{11}C_p$ the chain is C-B-C and for $B_{12}C_3$ the chain is C-C-C. The crystal structure is shown in figure 2. These theoretical configurations may not accurately reflect real samples, where differences in substitution may manifest [28].

Experimentalists have been using carboranes as an organic precursor to produce hydrogenated boron carbide [21], [24]–[26]. The basic chemical formula of carboranes is $B_{10}C_2H_{12}$. There are three possible isomers: orthocarborane, paracarborane and metacarborane. All of these molecules have a slightly distorted icosahedral structure. Ten boron atoms and two carbon atoms form the inner cage, and twelve surrounding hydrogen atoms pointing outwards, each bonded with an atom of the inner cage [29]. These three molecules are shown in figure 3. Among these three, the most prominent is orthocarborane.
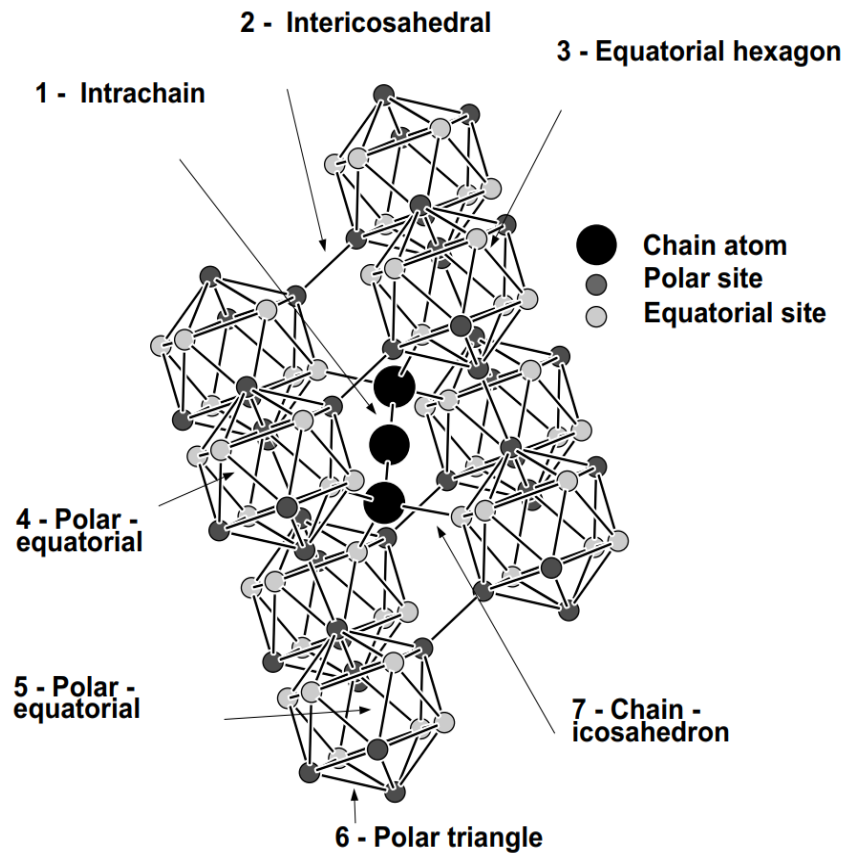
Figure 2. Crystal Structure of Boron Carbide [28].

At room temperature and pressure, all three isomers are solid. All crystals have FCC structure, with unit cell dimensions of 9.86 Å and Z=4 [30]. The melting points of o-, p-, m-carboranes are 570K, 534K and 546K respectively. Carborane molecules form a crystal structure due to the presence of weak van der Waal forces. Each isomer has three different crystalline phases. The phase transitions of o-carborane occur at 274K and 167K, m-carborane at 277K and 165K, and p-carborane at 303K and 240K [31]. For all of the three compounds, phase I and phase II, which are high-temperature phases, are orientationally disordered. Phase III, the lowest temperature phase, is orientationally ordered [30], [31].
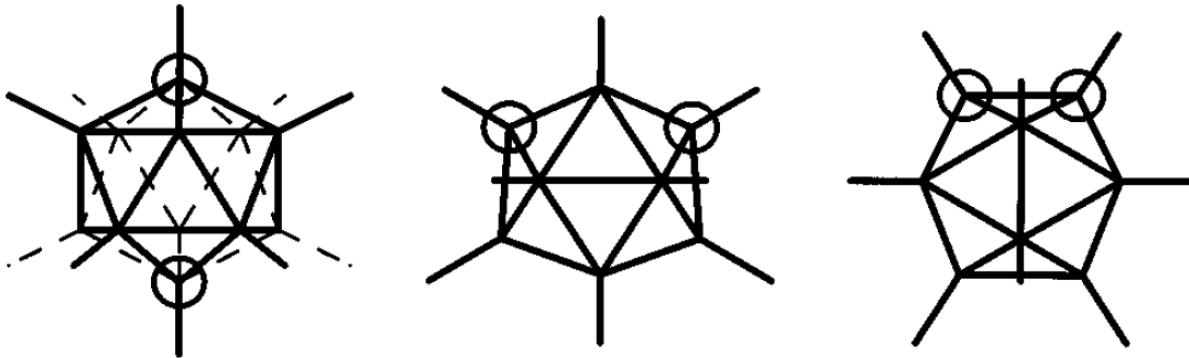
Figure 3. p-carborane, m-carborane and o-carborane molecules. The circles refer to the location of the C atoms [26].

Amorphous Hydrogenated Boron Carbide. Fabrication of thin films of boron carbide using plasma-enhanced chemical vapor deposition technique from the sublimed vapor of organic precursor orthocarborane produces amorphous hydrogenated boron carbide [22], [27]. Films produced from this method have a wide range of hydrogen contents [21], [26] with distinct mesostructures, [32]–[35] which can be altered by tuning the fabrication and post-fabrication conditions. The optimized geometries for the calculated molecules are show in figure 4. All short, intermediate and long-range physical orders have distinct impacts on the mechanical and electrical properties of the films. To train these properties for device applications, it is imperative to understand the complex relationship between the fabrication process and the final product.

It is not yet well-understood what chemical reactions occur when orthocarborane in the gaseous phase is subjected to reactive argon plasma. It is more probable that the thin films grown from the PECVD are different from the bulk production for two key reasons: firstly, the presence of 50% atomic percentage hydrogen and secondly, the presence of two neighboring carbon atoms in orthocarborane. Some reasonable possibilities are the rejection of some hydrogen atoms and
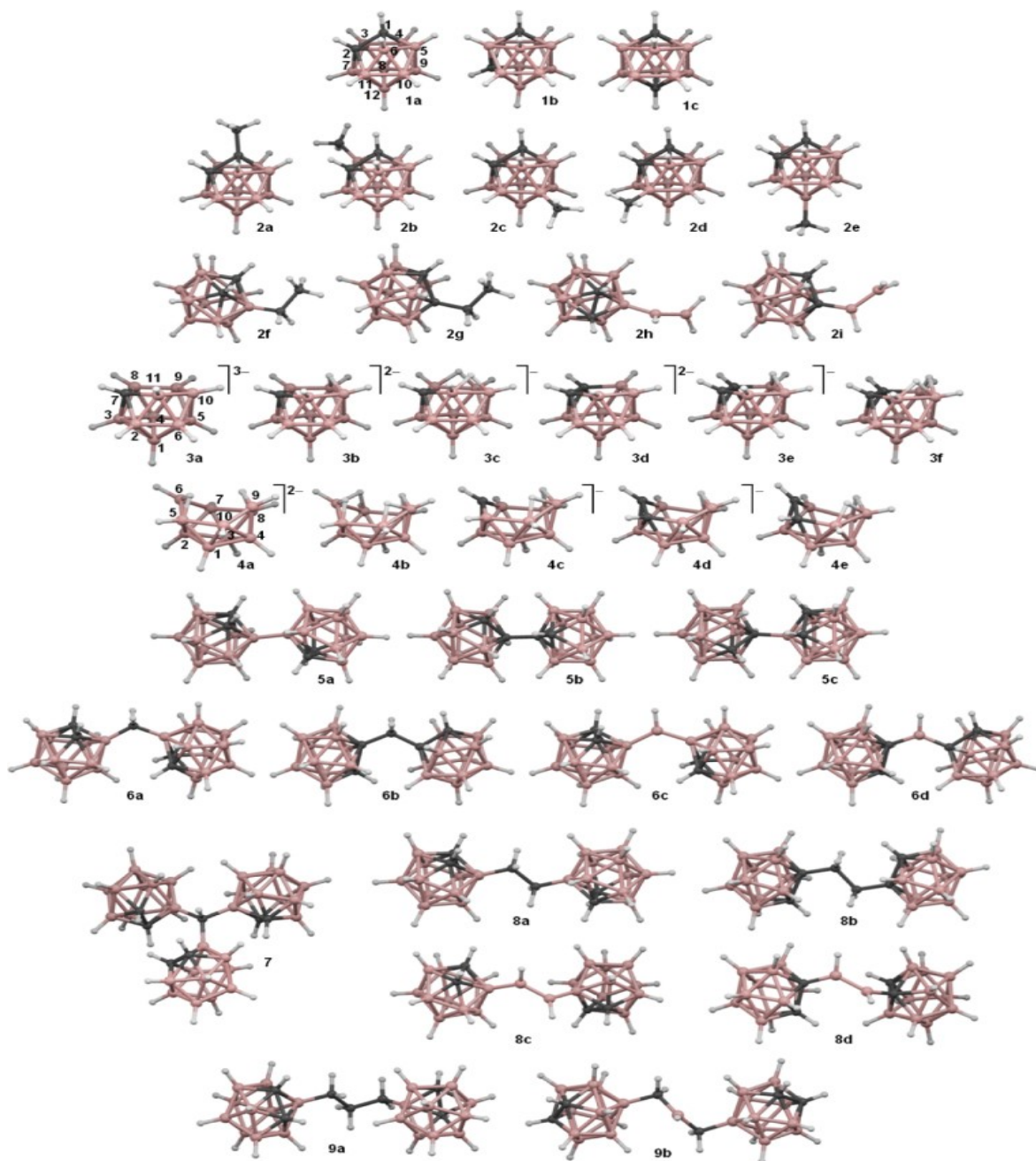
Figure 4. Optimized geometries of orthocarborane-based model compounds calculated using DFT [41].

creation of active sites in the closo-icosahedral species, broken or open-cage species, isolated

atoms or smaller molecular fragments [34], [36]–[38]. In the next phase, densification, the

icosahedral base or the open cage species connects directly with the other or through chains of different length from single molecules to small fragments. It is also possible to form bigger molecular networks with lower total energy.

Classical Molecular Dynamics Simulation

The sole purpose of any modeling is to mimic real-life scenarios. From realistic modeling, the difficulties, expense, and limitations in experimental studies can be avoided. Faster and more rigorous analysis can be done through computer modeling. In materials science, modeling can be in different time and length scales. Briefly it is shown in figure 5. From the figure 5 we can see where the molecular dynamics (MD) can be fitted into the whole picture, and this also partially explains why we chose to apply this approach in our study. In this part we have presented a short description and theory of MD simulation.

The purpose of the MD simulation is to replicate atomic interactions in real life using computer modeling. For a system within a certain region of space, atoms are allowed to interact in a predetermined period of time that provides insight into the dynamic evolution of the corresponding system. In Classical molecular dynamics (CMD) simulation, we can obtain the trajectory of a system by solving Newton's equation of motion with the object's initial position, velocity and force information.

$$m_i \frac{\delta^2 r_i}{\delta t^2} = F_i$$

$$F_i = - \frac{\delta U(r_1, \dots \dots, r_n)}{\delta r_i}$$

Here the m_i is the mass and r_i is the position of the ith object of a system with n objects in total. U is the potential of the system in a given configuration. Using the correct potential U to

7

solve the equation, one can calculate the trajectory of a system having atoms, grains, mesoscale particles or huge planets. Force information, for example, forces on i^{th} particle F_i can be calculated from the derivative of U. For n objects, there will be n differential equations to solve in each iteration. In practice, instead of solving a huge set of coupled differential equations, integration is used over a small time step (typically fraction of a femtosecond).
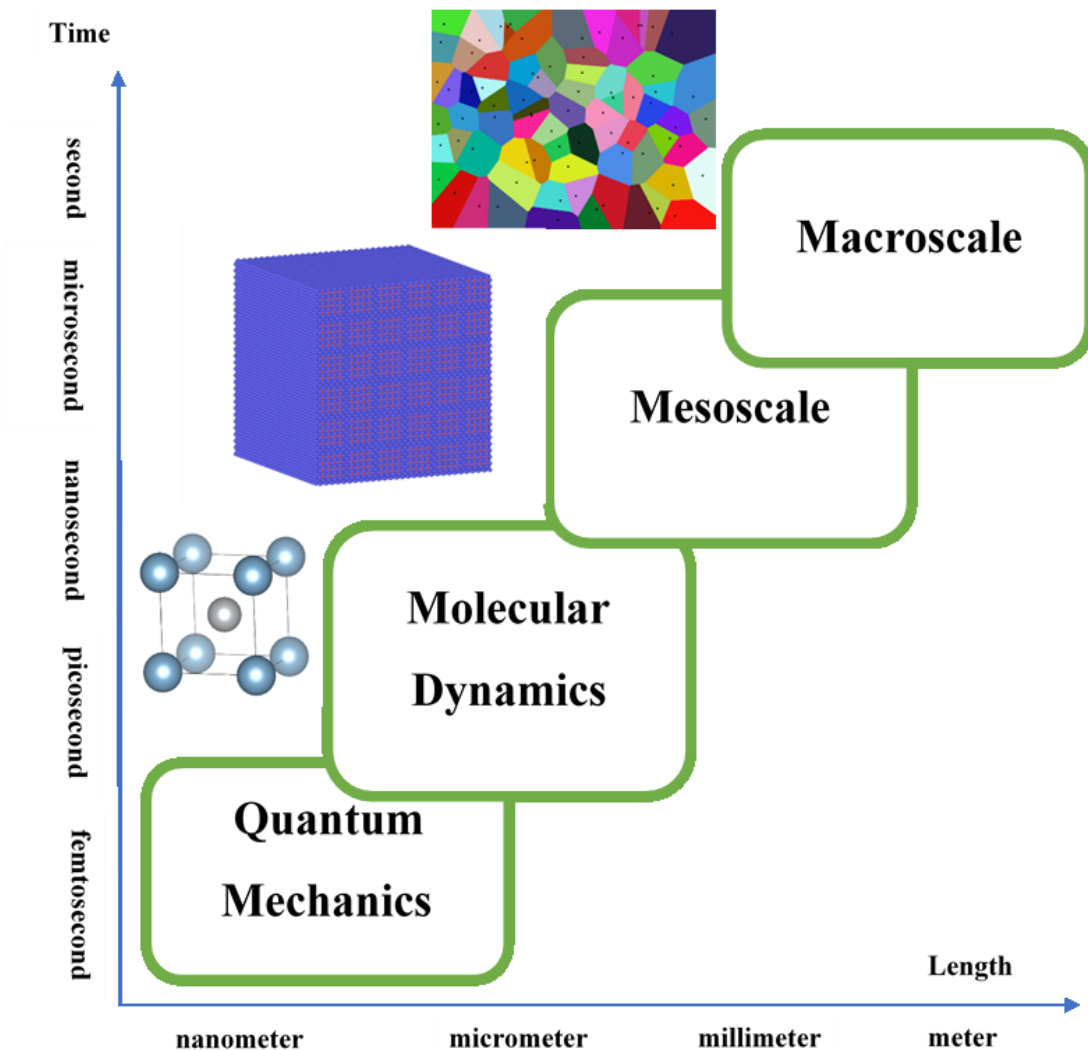
Figure 5. Modeling time and length scales

$$-m_i \frac{dv_i}{dt} = \sum_j F_2(r_i, r_j) + \sum_{j,\ k} F_3(r_i, r_j, r_k) + \cdots \ldots \ldots$$

$$\frac{dr_i}{dt} = v_i$$

Here, F_2 is the force between two atoms and F_3 is between 3 atoms. After each iteration, positions of the atoms are adjusted as well as the force information.

In reality, the atoms always continue to vibrate; in any non-zero temperature, atoms will not stay at rest at their energy minimum. If the simulation goes on for a sufficient time span, it samples the Boltzmann distribution. The distribution refers to the probability of having a particular arrangement of atoms which is correlated with the energy of the system. Sampling the Boltzmann distribution is a very effective way to explore the energy surface. The first computer simulation work was published in 1957 by Alder and Wainwright [39]. It consists of 32 atoms with square potential showing the phase transition through the hard sphere model. The hard sphere model describes that atoms are not allowed to overlap, just like macroscopic metal balls. Now directly from solving Newton's force equation, we obtain a system with three constant quantities: number of atoms, volume, and energy. The energy does not change because the system is isolated and at the same time the total momentum and angular momentum is constant. This system is referred to as NVE ensemble or microcanonical ensemble. Microcanonical ensemble does not have any pressure and temperature control.

However, in actual experiments, quantities like volume, pressure or temperature are the synthesis or characterization parameters. Often the pressure is kept constant, such as synthesis in a vacuum chamber, high vacuum or atmospheric conditions; volume, such as in measuring bulk modulus; or temperature, such as in annealing of samples. Most of the experiments are related to these easily measurable quantities. Different statistical ensembles can be generated to mimic

experimental conditions other than NVE, including constant temperature, constant volume (NVT), constant temperature, constant pressure (NPT), constant temperature, constant stress (NST), constant pressure, and constant enthalpy (NPH). A short description of these ensembles is given below:

NVT Ensemble. This constant-temperature and constant-volume ensemble is also called canonical ensemble. This might be the best option to equilibrate system pressure initially. In other words, equilibrating initial structure with NVT allows one to fix the system pressure for materials at any phase. NVT without periodic boundary conditions is a good way to perform conformational exploration of molecules. This is often useful working with chemical reaction in gaseous material as system pressure is irrelevant.

NPT Ensemble. A constant-temperature and constant-pressure ensemble enables the user to tune both system pressure and temperature by allowing the volume to change and energy to flow in and out of the system. In every step, the unit cell vectors are adjusted in order to achieve the targeted pressure. This can be the best option to fix the system equilibration volume and densities under predetermined system pressure. It is a good practice to equilibrate the initial structure using NPT or NVT before performing any kind of simulation with any materials or interatomic potentials.

NST Ensemble. The constant-temperature and constant-stress (NST) ensemble can be considered as a specific type of NPT ensemble. It enables to tune the stress tensor for xx, yy, zz, xy, yz, and zx components. This ensemble can effectively be applied to analyze the stress-strain correlation of materials.

NPH Ensemble. Enthalpy, H is the sum of internal energy and product of system pressure and volume. Interestingly, constant-pressure and constant-enthalpy (NPH) ensemble is

equivalent to NVE ensemble but NPH is a way out to control the system pressure without controlling the system volume.

In terms of simulation, maintaining a constant volume and pressure is very straightforward. To change pressure, one simple approach is a piston-like mechanism. However, controlling temperature is tricky, and careful consideration and extensive calculation are required. The temperature depends on the velocity of all the particles and controlling the velocity might introduce further constraints on volume and pressure. To explain further the control of temperature, the concept behind the thermostat should be explained. Thermostats can be compared to a heat bath. Heat bath entity regulates the temperature of the material. In molecular dynamics, the temperature can be defined by the following equation [40]:

$$\frac{kT_{MD}}{2} = \frac{1}{6N} \sum_{i=1}^{N} \sum_{j=1}^{3} m_i v_{ij}^2$$

k = Boltzmann constant

T_{MD} = temperature

N = number of particles

m = mass of the particles

v = velocity of the particles

for three-dimensional velocity components j=3.

The summation is for creating a distribution. Controlling the temperature in simulation can be done by restricting the average velocity within the proper distribution. In common practice, the beginning temperature can be set by assigning velocities at random under Maxwell-Boltzmann distribution. One strategy to move further is using the Anderson approach [41]. In this approach, in every timestep, one particle is allowed to interact with the heat bath, and a new

11

velocity is assigned under the Gaussian distribution. In this particular approach, the time it takes

to reach the intended temperature is sensitive to the number of collisions per unit time. This can

be overcome by including an additional force (Langevin thermostat [42]). This approach may

cause overcorrection.

The Nosé-Hoover thermostat is another approach which is more robust and offers a better

solution. In this method, an additional degree of freedom is added for heat bath.

$$H_{nh} = \sum_i \frac{p_i^2}{2m_i s^2} + U(r,q) + \frac{p_s^2}{2Q} + LkT.\ln(s)$$

H$_{nh}$= heat bath

L = the number of independent momentum degrees of freedom

Q = An imaginary mass (should be taken carefully)

p$_s$ =momentum of heat bath variable

the original Hamiltonian is associated with four interrelated equations when s(t)=1,

$$\dot{r}_i = \frac{m_i v_i}{s}$$

$$\dot{v}_i = -\frac{1}{m_i}\frac{\delta U}{\delta r_i}$$

$$\dot{s} = \frac{p_s}{Q}$$

$$\dot{p}_s = \sum_i m_i s \dot{r}_i^2 - LKT$$

It should be noted that the last two equations refer to velocity control. The equation for

velocity control can be rewritten as,

$$\frac{ds}{dt} = \frac{Lk(T - T_{target})}{Q}$$

In molecular dynamics, the most commonly used algorithm for time integration of the

equation of motion is the Verlet algorithm. This can be explained from Taylor expansion up to

the third order. If the position of any particle for a certain time t is known (r) and the time step is

δt, according to Taylor expansion the equations of next and previous steps are (respectively):

$$r_i(t + \delta t) = r_i(t) + \dot{r}_i(t)\delta t + \frac{1}{2}\ddot{r}_i(t)\delta t^2 + O(\delta t)^3$$

$$r_i(t - \delta t) = r_i(t) - \dot{r}_i(t)\delta t + \frac{1}{2}\ddot{r}_i(t)\delta t^2 - O(\delta t)^3$$

Summing up these two equations:

$$r_i(t + \delta t) \approx 2r_i(t) - 2r_i(t - \delta t) + \frac{F_i(t)}{m_i}\delta t^2 + O(\delta t)^3$$

The above equation is the Verlet algorithm.

It has been studied that the computation of force expression is the costliest calculation

and most time-consuming [40]. For a group of particles, theoretically, each of the particles is

interacting with all other particles. For n particles, the interaction equations would be n^2. But it

should be noted that after a certain number of nearest neighbors, most of the interactions can be

negligible. The common approach is choosing a suitable cutoff distance r_c for any particle,

considering only the forces on that particle of the particles lying within the cutoff distance r_c.

Cutoff distance mostly defines how many nearest neighbors' interactions should be considered.

A sensible choice of the cutoff distance creates a balance between the desired accuracy and

simulation cost in CMD. Simulation load for long range forces like Coulomb interaction can be

reduced by approximation methods, the particle-mesh algorithm for example [43].

It should be kept in mind that of many different tools in modeling, CMD is commonly

used; yet, like others, this approach has its own limitations. It is beyond the scope of this thesis to

discuss its entirety, but a few should be mentioned here. Firstly, in CMD, atoms are treated as a

point mass. Without considering the quantum effect, CMD often has a certain level of minimal

errors. According to de Broglie, all particles can be treated as matter waves and the wavelength

can be found as $\lambda=mv/h$. For most of the atoms at room temperature, the wavelength is around

0.2 angstrom, whereas atomic distance is mostly 1-3 angstrom. For very light atoms like

hydrogen or helium or for ultra-high temperature calculations, ignoring the quantum effect may

lead to erroneous results. Secondly, for a desirable level of accuracy using the Verlet algorithm,

in CMD the time step should be at maximum 1-2 femtoseconds. Mostly, a fraction of a

femtosecond time step is used. With available modern computational resources, one can continue

simulation for a few billion steps, a highly ambitious goal, which would compute a system

response for a few microseconds only. For atomic scale modeling with CMD, even though one

can work with hundreds of millions of atoms, it should be noted that in reality, it would be a

cube with sides of a few hundred nanometers. Periodic boundary conditions can be used for a

homogenous system like crystalline materials to suppress this issue, but for non-homogenous

like amorphous materials, this is a big challenge [44]. Due to these limitations, modeling results

are often highly misleading. For example, one can do heating or cooling of material with a

heating rate of 1K/ns which is considered extremely slow in modeling, [45] but in reality, it is

impossible to achieve a heating rate of 10^9K/s. Similarly, for compression taste in simulation, a

commonly used strain rate is 10^{-4}/ps which converts a rate of 10^8/s [46], [47], whereas, in the

experiment, an extremely high strain rate is considered 10^4-10^6 s^{-1} [48]. Finally, CMD works

with Born–Oppenheimer approximation, where lighter electrons adjust instantaneously with the

changes in the position of heavier nuclei. This is described by the potential energy surface.

That's why traditional CMD cannot model chemical bond breaking and forming (there are

alternative methods for that). The interatomic potential is obtained mostly by some fitting

techniques [49]–[51] for important parameters like elastic constants, thermal expansion from

highly accurate density functional theory (DFT) calculations, or experimental data. One big

problem with these potentials is they lack transferability. For example, the Ni parameters for Ni-Al might not be suitable for Ni-Al-Co. Even one potential for any element might be applicable for only very specific studies. Making a single potential itself can be time-consuming, even with limited applicability. This might raise the question of justifying the approach. For our study, we have used the reactive force field (ReaxFF) as interatomic potential which has several advantages over traditional force field. Later, a discussion on ReaxFF will be given in greater detail.

All of our CMD simulations have been performed using LAMMPS code [43], [52] which is developed by Sandia National Laboratories, a US Department of Energy laboratory. This is a code for a CMD system on different scales. The full name is Large-Scale Atomic/Molecular Massively Parallel Simulator. Although there are other notable codes like IMD [53], MDACP [54], [55], MDSPASS [56], [57], GULP [58] and others, LAMMPS was chosen as it is most widely used and have all our required methods. Codes like AMBER [59], CHARMM [60] and NAMD [61] were developed especially for the biomolecular study.

LAMMPS

LAMMPS can model particles or atoms in solid, liquid or gaseous phase and also the combinations of these phases. The number of particles can be anywhere between a few to few hundred million in both two-dimension and three-dimension systems. It can potentially usable for modeling of an atomic, microscopic, mesoscopic or continuous scale. Because of these versatile potential applications, it has been used for a wide range of materials including both hard and soft materials. Starting from metals and semiconductors to polymeric, biomolecular, and granular systems, LAMMPS has been extensively used [43].

15

LAMMPS can be compiled and run in serial in one core on our desktop computer or laptop, but it is designed for efficient parallel computing in supercomputers or shared memory boxes using message-passing techniques. In fact, it runs on any computing systems that support the Message Passing Interface (MPI) library.

LAMMPS is written in C++ language, whereas previous versions were in Fortran (F77 and F90). The code is developed in such a way that modification for new and extended applications can easily be done. This enables it to remain compatible with the continuous development of new force fields, particle types and pair styles or aspects of analysis. General programmers can also contribute to adding more features in the existing code as part of a user package or standard package depends on the potential application of the contribution. LAMMPS usually utilizes Newton's equations of motion for defining the interactions among a group of particles. It should be noted that a particle can be either an electron, an atom/molecule/radical (charged/uncharged), or a macroscopic grain. LAMMPS can model both short- and long-range interactions among particles.

PACKMOL

Most of our simulation started with random initial structures in different sizes of simulation cells. PACKMOL code was very useful in the creation of different-sized initial structures with randomly placed molecules to model gaseous mixture and amorphous structures [62].

PACKMOL can produce initial coordinate points for molecules in a predefined simulation cell. While producing these coordinates, wide ranges of spatial restriction can be incorporated to produce the desired structure. The minimum intermolecular distance and its

relative orientation in the three-dimensional space is an example. The minimum distance constraint can ensure limiting the large repulsive van der Waals interaction at the beginning of the simulation. It is possible to pack millions of molecules for making complex mixtures or interfaces of different material phases. The user needs only to provide coordinates of one molecule or unit. This code supports PDB, TINKER, XYZ and MOLDY formats, which is enough for our purpose because conversion between LAMMPS data format and XYZ or PDB is quite simple and straightforward.

ReaxFF

Atomic-scale modeling has provided modern researchers with a more affordable way to study novel materials in greater detail, which is often expensive and sometimes not possible with available experimental resources. Quantum mechanics-based simulation methods have been widely used for all kinds of materials because of their higher accuracy, user-friendly packages, and easy access. However, the computational expense associated with this approach has made it only applicable for smaller (few tens of atoms) systems. This scale of small systems is often inadequate to understand the overall behavior of a material, such as in a system with larger molecules or amorphous structures. In order to overcome this limitation with quantum mechanics (QM), empirical force fields (EFF) have been developed. The parameters of EFFs are fitted either against the data sets obtained from QM, experimental, or both. Consequently, the parameters from fitted data are less reliable than the fitting data itself. But this EFF demands lower computational resources in several orders of magnitude, which seems to be a fair trade-off.

EFF methods have been successfully applied in condensed phase systems. But they failed to describe reactive systems and bond energy to the dissociation limit. This is because EFFs are

mostly trained where bonds remain close to their equilibration. Reactive force field (ReaxFF) has been developed to bridge the gap of quantum chemical and empirical force field-based chemical computational methods. This is a bond order-based force field which allows continuous bond breaking and forming. The bond order is obtained from interatomic distances empirically. Compared to other empirical force fields, ReaxFF has higher transferability and can be used for all three phases of matter and the interfaces of the phases. Primarily the general guidelines in its development include (1) continuous forces and energy including reactions, (2) one particular element has only one force field atom type, (3) no pre-defined reactive site is required [40]. Highly flexible transferability offered by ReaxFF now provides us a pathway to a different scale of modeling which was previously unachievable with available computation resources. For example, oxygen atoms have the same parameters set as in solid metal oxide, liquid water or gaseous O_2 molecules [63]. This new feature enables modeling and study focusing on diversified aspects of more complex systems with multiple phases. For example, in our studies, initially, we started with a system including the gaseous phase (a gaseous mixture of argon and orthocarborane) and then we continued our studies to the solid phase (amorphous hydrogenated boron carbide).

Methodology. ReaxFF can describe both reactive and non-reactive interactions by eschewing both bond order formation and polarizable charge description. Thus, ReaxFF can describe both covalent and Coulombic interactions for a wide range of materials. The energy equation of ReaxFF is

$E_{system} = E_{bond} + E_{over} + E_{angle} + E_{tors} + E_{vdwaals} + E_{Coulomb} + E_{Specific}$ [63]

E_{bond} = associate with bond forming energy; obtained directly from bond order; related to interatomic distance.

E_{over} = Over coordination energy; prevents over coordination of atoms.

E_{angle} = Angle strain; a three-body parameter; equilibrium angles between angles depends on the bond order of the central atom

E_{tors} = torsional energy; four-body interaction

$E_{vdwaals}$ = van der Waals energy for every atom

$E_{Coulomb}$ = Coulombic interaction

$E_{Specific}$ = specific energy terms; not related to above listed term

In ReaxFF, the calculation of bond order is performed empirically direct from interatomic separation. Additionally, the potential has both bond order-dependent and independent components. The equation for bond order calculation is as follows

$$BO_{ij} = BO_{ij}^{\sigma} + BO_{ij}^{\pi} + BO_{ij}^{\pi\pi}$$

$$or, BO_{ij} = \exp\left[p_{bo1}\left(\frac{r_{ij}}{r_o^{\sigma}}\right)^{p_{bo2}}\right] + \exp\left[p_{bo3}\left(\frac{r_{ij}}{r_o^{\pi}}\right)^{p_{bo4}}\right] + \exp\left[p_{bo5}\left(\frac{r_{ij}}{r_o^{\pi\pi}}\right)^{p_{bo6}}\right]$$

Here, BO is the bond order between i and j atoms and r_{ij} is the distance between them. P_{bo} terms are empirically obtained and r_o is the bond length at equilibrium. The transitions between these pi and sigma bonds are continuous. This continuity has made it possible to calculate forces between atoms from derivatives of the potential energy surface. This formula can describe long distance covalent interactions (5 A and beyond) which enables the force field to accurately provide reaction barriers. Along with this long-distance covalent interaction over valency may occur with atoms, such as bonding between neighboring hydrogen atoms in methane molecules. This issue is checked by bond order correction. Bond order correction also provides bond energy and angle strain information. The Coulombic interaction is calculated in every iteration from a charge equilibration feature. The overview of ReaxFF energy component is shown in figure 6.
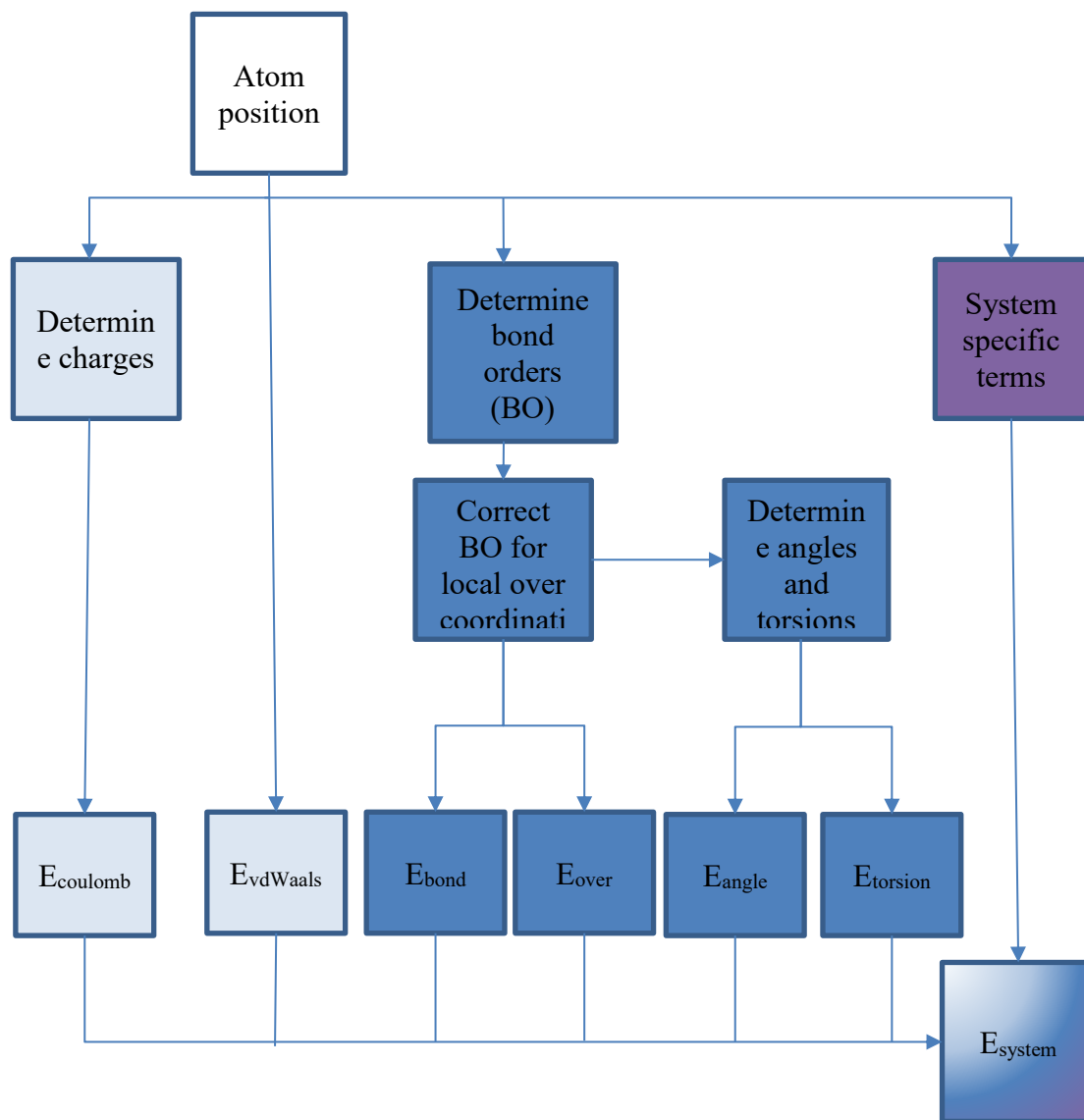
Figure 6. Overview of the ReaxFF energy components [66]

Quantum Calculation

We previously discussed the limitation of the application of quantum mechanical (QM) calculation in our study as for QM with our available computational resources we would be able to simulate a model of few tens of atoms. Therefore, our study mostly based on classical MD

using a reactive force field. However, we carried out some QM calculation to determine the extent of application of our force field for hydrogenated boron carbide. Regarding QM calculations, density functional theory (DFT) [64]–[66] was adopted in substitution of core nuclei and valence electron exchange-correlation term calculation. To elaborate, in DFT the multiple electron interactions in atoms can be defined by the use of spatially dependent electron density functionals- functions of another function. DFT has been widely used since the 1970s in physics, chemistry, and materials science to study electronic structures. However, the accuracy of the approach was not up to the desired level. From the 1990s after some major modifications in the theory, the accuracy increased along with the decrease of computational costs.

Compare to classical MD, DFT is highly accurate and the potential files are available for every single element in the periodic table. Furthermore, details of the electronic structure can be obtained using DFT which is not possible in classical MD. However, even the computational costs decrease over time for DFT, the expense is still several order of magnitude more than CMD. To understand the basic theory behind DFT let us consider the following equation of the Hamiltonian

$$H_{NVE} = \frac{1}{2}\sum_{i=1}^{N} m_i r_i^2 + E[\varphi(r_1, r_2, \ldots, r_N)]$$

The key idea behind the equation is, the potential energy of a system can be determined from its electronic structure at each step. Here, φ ($r_1, r_2, \ldots, r_N$) describes the Kohn-Sham single-electron wavefunctions for the ground state. The ground state energy data will provide information about force. From the force information, the atoms can be moved to the next step and thus one iteration can be completed. This DFT-based approach is referred to as ab-initio molecular dynamics (AIMD). Car-Parrinello method [66] is the first AIMD approach is based on the equation –

$$H_{CP} = H_{NVE} + \frac{1}{2}\sum_j \mu \int |\dot{\psi}_j(r)|^2 dr + L_{ortho}$$

The term H_{NVE} is from the previous equation and the next term is for the kinetic energy of imaginary mass μ, which refers to the electronic degrees of freedom. The term L_{ortho} for maintaining the orthogonality of the single electron wave function. The equation of motion becomes

$$\begin{cases} \mu\ddot{\psi}_i(r) = -H_{CP}\psi_i(r) + \sum_j \psi_j(r)\Lambda_{j,i} \\ m_i\ddot{r}_i = F_i \end{cases}$$

Thus, avoiding solving Kohn-Sham equations by self-consistent computation, the same level of accuracy can be achieved. Nevertheless, at present, popular codes adopt more efficient diagonalization algorithm of Kohn-Sham matrix. This newly invented algorithm also offers self-consistent computation. Similar to CMD, several open-source and commercial codes are available. VASP [67], Gaussian [68], Wein2K [69], CPMD [70] are some of the most common commercial codes available and ABINIT [71], Siesta [72] and Quantum ESPRESSO [73] are the open source codes. For our studies, we have used the Vienna Ab-initio Simulation Package (VASP). The VASP code largely depends on fast Fourier transform (FFT) and linear algebra libraries, such as BLAS, LAPACK, ScaLAPACK. VASP is written in Message Passing Interface (MPI) and Open Multiple Processing (OpenMP) directives. VASP has pseudopotentials developed for almost every element in the periodic table. Obviously, it can be used to study metal, semiconductors, insulators in solid, liquid and vapor phases. Furthermore, it can be used for the surfaces and interfaces of these phases.

COMPUTATIONAL DETAILS

Energy Minimization and Bond Dissociation Energy

We compared the energy data calculated from ReaxFF and DFT at the beginning of our studies. It is previously mentioned that the QM calculations were performed using commercial code Vienna Ab-initio Simulation Package (VASP) [67]. Plane wave basis set and projector-augmented wave (PAW) based pseudo-potentials were implemented in VASP software [67], [74]–[76]. In substitution of core nuclei and valence electron exchange-correlation term calculation, we have used the ultra-soft pseudopotential. As we studied insulator type materials, the pseudopotentials were with Perdew Burke Ernzerhof (PBE) version of generalized gradient approximation (GGA) exchange-correlation functional of DFT. We used the Monkhorst-Pack [77] scheme to create the k-space matrix. The plane wave basis set energy cut off was set to 520 eV and the tetrahedron method with Blöchl corrections smearing was selected with sigma value 0.2. The input script is available in the appendix.

The QM calculations included the bond dissociation energies of different bonds of an orthocarborane molecule, ground state energies of different relevant compounds- such as orthocarborane, BH_3, CH_4, B_2H_4, H_2 and so on. To calculate the ground state energies, we chose simulation cells large enough to fit a single molecule of the above compounds with negligible interaction between the molecule and its periodic image. For example, for orthocarborane molecule, we chose 12 A edged cubic simulation cell, whereas for BH_3 the edge was 6 A and so on. The K-points were used 4 4 4 for most of these energy minimization calculations.

To obtain a bond dissociation energy curve, we first took the structurally minimized molecule. Then one atom of the relevant bond was gradually moved far enough so that the bond

can be considered completely broken. We calculated the total energy of the whole system at different distances of the particular atom and thus obtain the sample points of distant vs energy. It should be noted that during this whole process all other atoms of the molecule kept fixed in the initial position. For example, while calculating B-H bond dissociation energy in orthocarborane molecule, we obtained the structurally minimized orthocarborane molecule first. We varied the distance between one hydrogen atom connected with one of the boron atoms while keeping all other atoms fixed in their respective positions and calculated total energy at all distance. Similar calculations have been done using the ReaxFF potential we chose to use as well.

Argon Bombardment

Our primary focus was to understand the outcomes of ion bombardment on orthocarborane molecules. It should be noted that in the experiment, ion bombardment occurs in the gaseous phase, a mixture of bombarding ion and Orthocarborane [26], [27]. To model this, the first challenge was to create the initial structure. The process started with making a single orthocarborane molecule. From a uniform icosahedral structure of B_{12}, two boron atoms were replaced by two carbon atoms. 12 hydrogen atoms pointing outwards of each atom were added, forming the icosahedra as shown in figure 7a. But due to the presence of carbon, the structure of the orthocarborane molecule is slightly distorted icosahedra figure 7b. Additionally, the length of the BH and CH bond is not identical, which also distorts the overall symmetry of the structure. The second structure was obtained by structural minimization of the first structure at 0K. The command for executing the structural minimization in LAMMPS is –

minimize 0.0 1.0e-8 1000 100000

minimize etol ftol maxiter maxeval

etol = stopping tolerance for energy (unitless)

ftol = stopping tolerance for force (force units)

maxiter = max iterations of minimizer

maxeval = max number of force/energy evaluations [78]
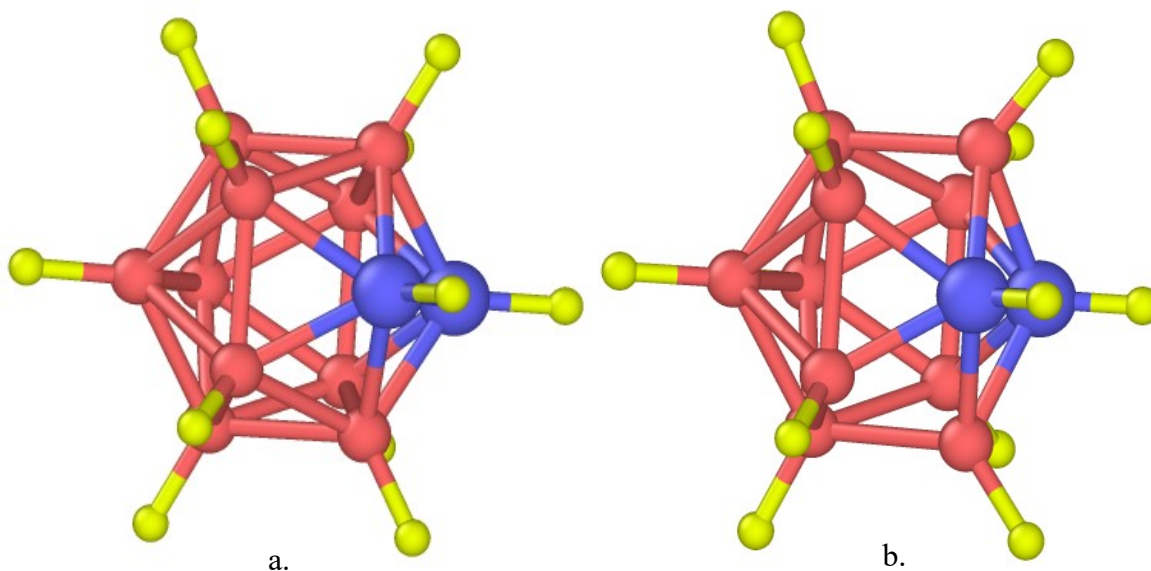
Figure 7. Orthocarborane molecule: (a) before relaxation, and (b) after relaxation

The approach of structural minimization is straightforward: iteratively the coordinates of the atoms were changed in order to find the local potential energy minimum. The minimizer limits the movement of atom coordinates in one iteration to enable relaxation of overlapping atoms where very large energy and forces are involved. The minimization finishes when any of the stopping conditions are fulfilled. The input scripts can be found in the appendix.

In the next step, we created the bigger structure of the gaseous mixture of argon atoms and orthocarborane molecules. Initially, a cubic simulation cell was taken with 100-angstrom edge length. One thousand orthocarborane relaxed units and a varied number of argon atoms (1-25) were packed randomly inside this cell. The minimum distance between the molecules was kept at 2 angstroms. The initial structure is shown in figure 8. We have used PACKMOL code to build the structure. The latest version of PACKMOL does not currently support periodic
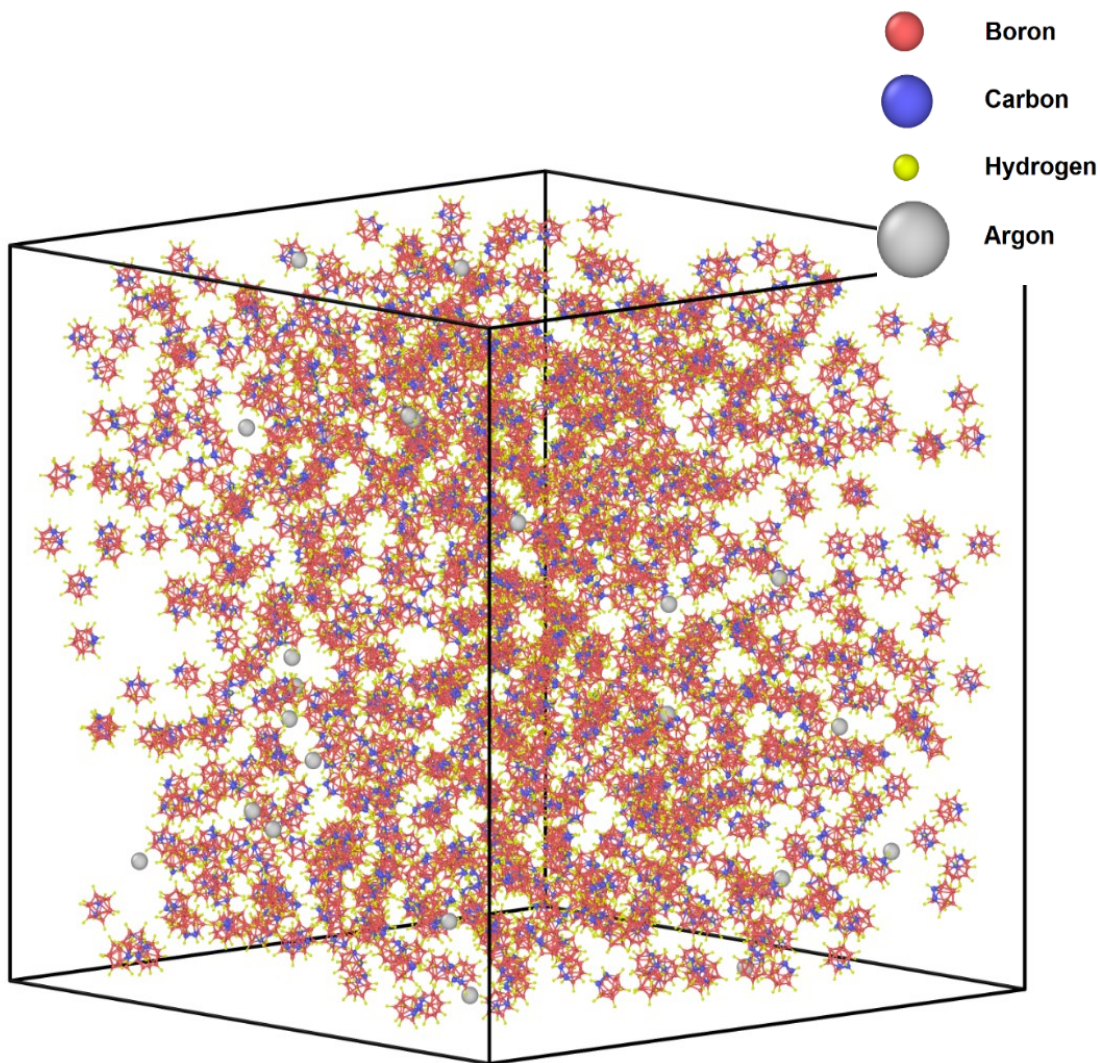
Figure 8. Initial structure for argon bombardment (atoms are not represented with their relative sizes)

boundary conditions while packing. But our intended simulation was with periodic boundary conditions. In order to avoid the overlapping of the atoms at the edge of the simulation cell, we extended the cell in all six directions by 1 angstrom. Before the bombardment simulation, another structural minimization was performed. Figure 9 shows the edge correction in 2D view.
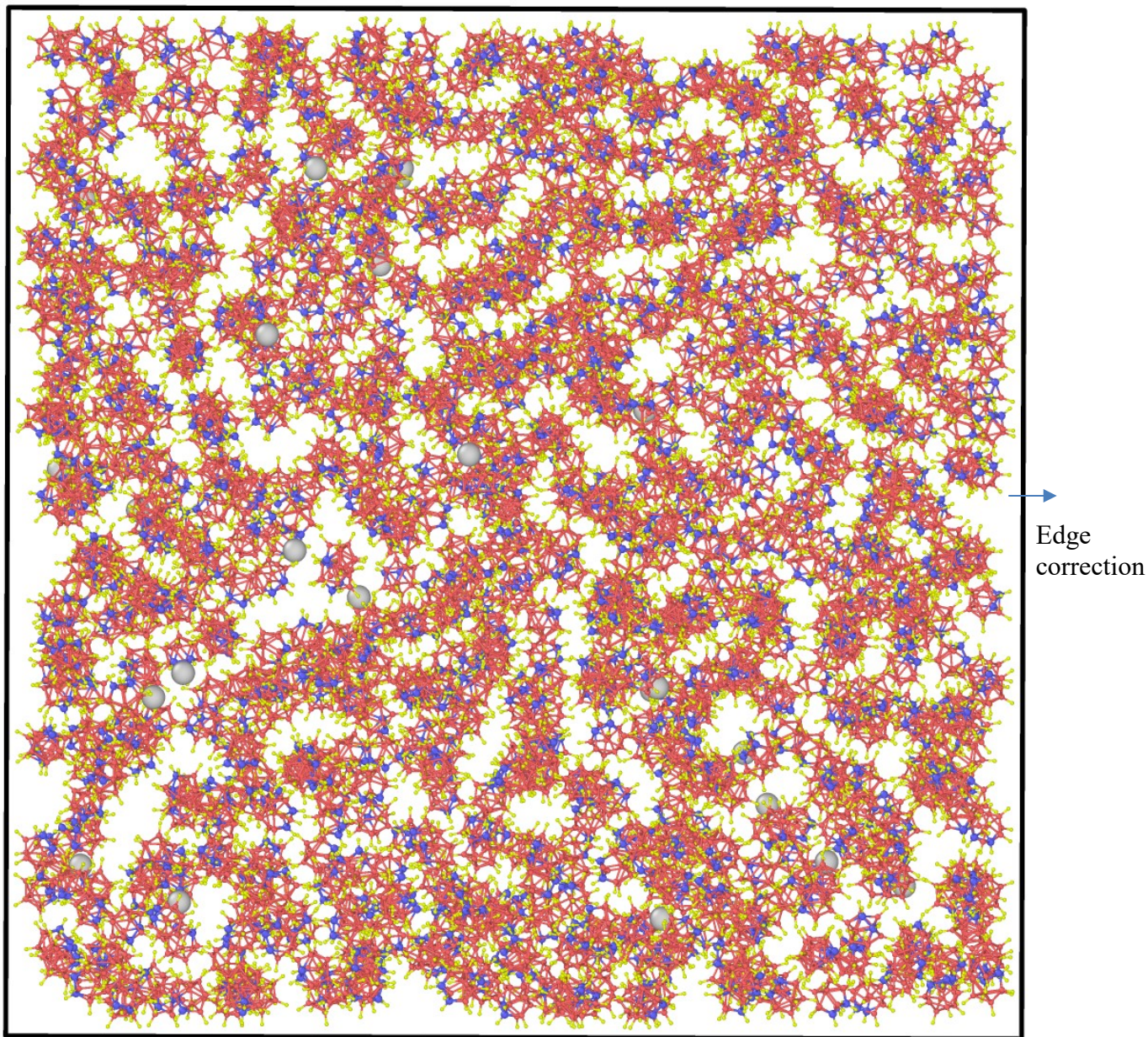
Edge correction

Figure 9. Initial simulation cell 2D view with after the edge correction (atoms are not represented with their relative size)

Choosing the initial kinetic energies of argon atoms was another big consideration. At first, we tested the outcomes of after the collision of single argon into a single orthocarborane. We started from a few electron volts and increased up to a few hundred electron volts. Below 30 eV the bombardment results showed only the formation of a cluster of distorted orthocarborane molecules, as shown in figure 10a. no hydrogen or other species ejected at this lower energy of argon. However, for 100 eV and beyond, the orthocarborane molecule was broken into smaller clusters and ejected different species, including hydrogen atoms. In figure 10b snapshot after 150 fs is shown for 190 eV argon energy. When the energy is a few hundred electron volts, single argon can damage several molecules through secondary, tertiary and beyond collisions. Additionally, the high energy ejected species can also cause significant damage to neighboring molecules. From these results, the argon energy was varied from 50 eV to 600 eV with 50 eV steps. 600 eV is around the upper limit of argon kinetic energy of conventional experimental setup. This argon energy distribution was found from previous theoretical studies [79], [80]. To model this high kinetic energy interaction, the time step should not be more than 0.1 fs [81]. In our study we have used 0.05 fs as this showed higher accuracy over 0.1 fs. All of the simulations were performed for 5 ps which is 200000 steps under the periodic boundary condition in X, Y, and Z direction. 5 ps was long enough for the argon atoms to transfer the kinetic energy to the orthocarborane molecules. The constant number of particles, constant volume and constant energy ensemble (NVE) was used. At the end of NVE simulation in each case, NVT ensemble which is constant particles, volume and temperature simulation, has been performed to cool down the structure to room temperature (300K). During the cooling down process temperature was controlled using Noose-Hoover thermostat in LAMMPS.
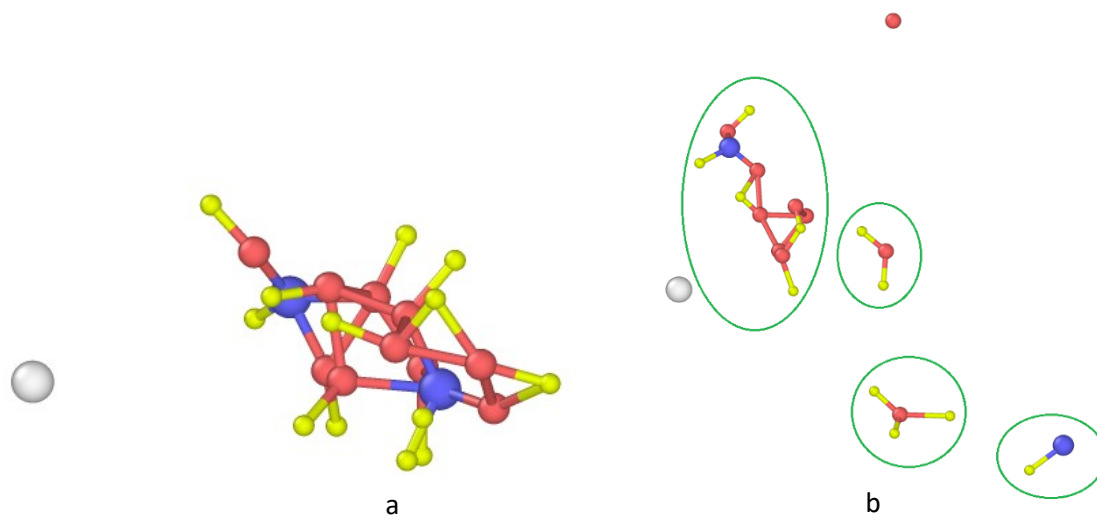
Figure 10. Snapshot after 150 fs of collision (a) 30 eV, (b) 190 eV

In order to analyze the results, we started with the calculation of pair distribution function (PDF) analysis of different pairs, including boron-hydrogen (BH), hydrogen-hydrogen (HH) and carbon-hydrogen (CH) pairs at different times. We calculated the time evolution of the number of species created due to the bombardment. Different cut-off distances were used in counting the number of species as the distance naturally changed with temperature change at different stages of the simulation.

Interaction between Free radicals and Orthocarborane

From the analysis of argon bombardment, we got the guidance of our future study. As previously mentioned, due to the time and simulation size limitation, it is impossible with the available computation resources to date model the experimental process as a whole. In every step of our studies, we had to find a way around these challenges.

In the next step of our studies, we wanted to analyze the interactions between the free radicals and the undamaged orthocarborane molecules. From our previous study, we observed

29

that there was a wide range of different species formed depending on argon energy and place of impact with the molecules. The species included BH, CH, BH_2, CH_2, BH_3, CH_3, H_2 and so on. Right after the bombardment, within a few hundred femtoseconds, there were free boron, carbon and hydrogen atoms too. Except for H_2 and BH_3, all other species are not neutral in charge and they are active at different levels. To keep our studies systematic, we took 1000 randomly packed units of orthocarborane molecules and a varied number of free radicals and equilibrated them at different temperatures. We started with isolated boron and carbon atoms randomly placed in the simulation cell. The size of the simulation cell was (92X92X92) angstrom^3 and the minimum distance between the atoms and molecules were kept 2 angstroms. The simulation cell is shown in figure 11. The ratio of boron and carbon was kept at 5 to 1, as this is the ratio of B and C in orthocarborane molecules. The number of B and C were varied from 50 to 2000 and 10 to 400, respectively. All of the simulations were done at three different temperatures: 300K, 500K, and 800K.

In order to make this study systematic and more detailed, we continued with BH and CH free radicals, BH_2 and CH_2 free radicals, and BH_3 and CH_3 free radicals. That means similar to isolated B and C as described before, we took 1000 orthocarborane molecules and replaced isolated B and C with either BH and CH, or BH2 and CH_2, or BH_3 and CH_3 respectively. In all cases, we maintained the ratio between boron and carbon 5 to 1 and we varied the number of the radicals similar to before, from 50 to 2000 and 10 to 400 for boron and carbon, respectively. Prior to packing, each of the free radicals was relaxed at 0K individually using ReaxFF. Each of them was equilibrated at 300K, 500K, and 800K. The simulations were under periodic boundary conditions, using canonical ensemble (constant volume and constant temperature- NVT). A time step of 0.25 fs was used, and the total steps were 10^6 giving a total time span of 250 ps.
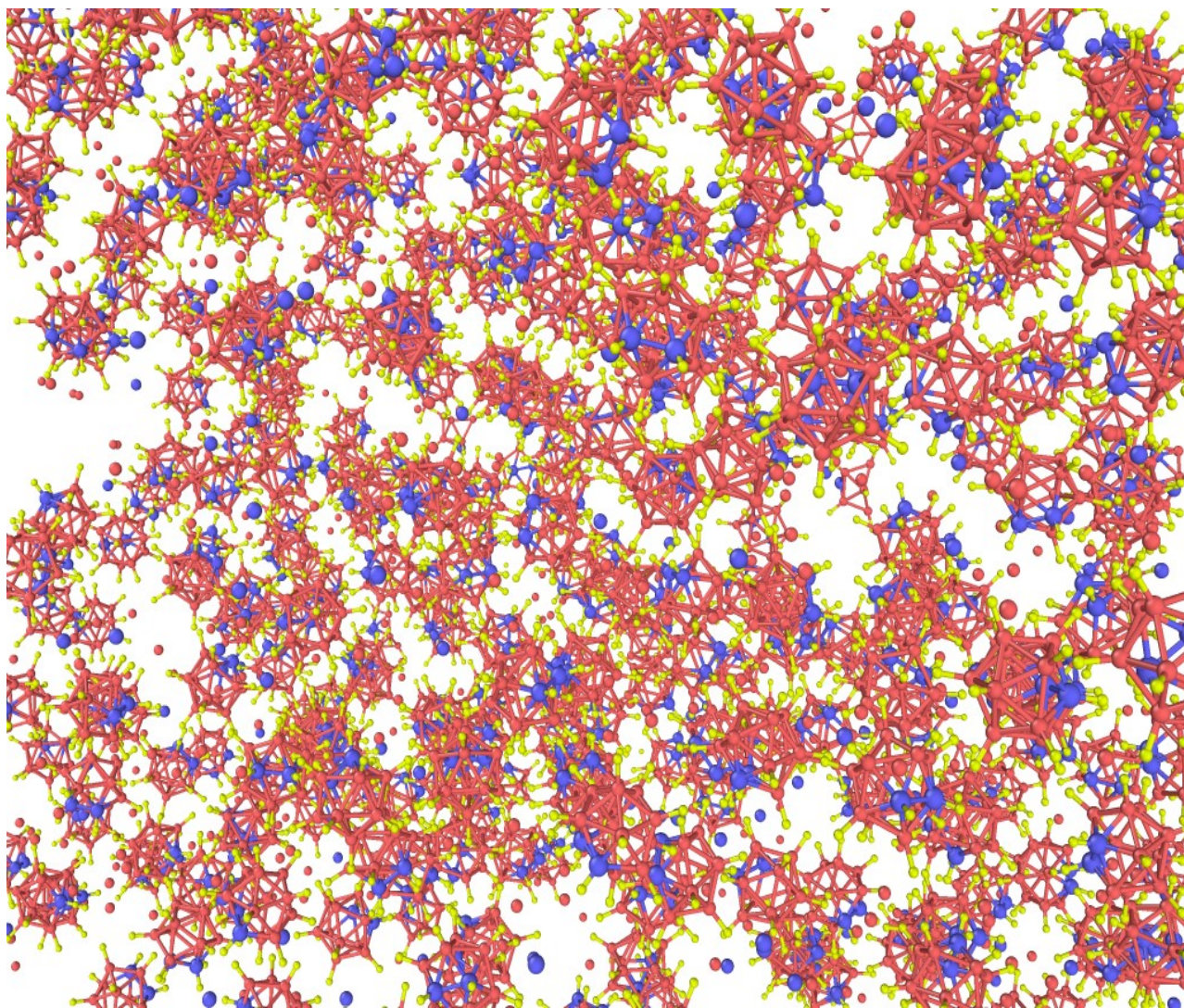
Figure 11. Initial structure for orthocarborane and free radicals (free boron and carbon atoms)

Amorphous Hydrogenated Boron Carbide

Study on amorphous hydrogenated boron carbide was the last part of our study. From the

analysis of previous works, we found out the possible species that can be created from the ion

bombardment and also the interaction between the active species with themselves and with other

orthocarborane molecules. Another important finding of ion bombardment study is the release of hydrogen from orthocarborane. Presumably, this release of hydrogen leads to the densification of the hydrogenated boron carbide thin films. The purpose of this study is to understand the densification process of thin films. One possible approach was to continue equilibration of the simulation cell of ion bombardment at a suitable temperature. The temperature could have been chosen from substrate temperature during experimental studies. This continuation could have been done after removing the Ar and other stable gaseous compounds for more realistic modeling. However, one big problem in this approach is the limited time span in modeling. We can only model for up to a few hundred picoseconds with our computational resources, which is not enough to show the complete reconstruction of hydrogenated boron carbide from bombarded orthocarborane. Therefore, we adopted an alternative route in this aspect knowing the fact that hydrogenated boron carbide also has an icosahedral structure as boron carbide [26], [82]–[85].

The key differences between orthocarborane and hydrogenated boron carbide are, for orthocarborane, each of the boron and carbon atoms is connected with a hydrogen atom, which is not true for hydrogenated boron carbide and there is no linker between molecules in orthocarborane. The biggest challenge was to create a hypothetical transitional structure falling between orthocarborane and hydrogenated boron carbide. To elaborate, the hypothetical initial structure we aimed to create, should produce a final structure close to the amorphous hydrogenated boron carbide after equilibration under the limited time span. At the same time, the structure should be close to the outcome of the bombarded orthocarborane. As there is no ideal single solution to this challenge we did as follows.

First, we considered two different crystal structures of boron carbide. One is B_{12} icosahedra connected by C-C-C chains and another is $B_{11}C$ icosahedra connected by C-B-C

chains as shown in figure 12. Our study was based on the assumption that these chains/linkers would have a significant contribution to the densification process. We took an isolated icosahedron from each of the structure and systematically added hydrogen in it. The atoms in the icosahedron were hydrogenated at varying percentages, including, 0%, 25%, 50%, 75%, 100%. We took one hydrogenated icosahedron and a chain (CBC or CCC) as one unit and randomly packed 1000 units of these in a cubic simulation cell with edge length 77 angstroms. The units for $B_{11}C$ icosahedron with CBC chains are shown in figure 13. Similar units were also created for B_{12} icosahedron and CCC chains. For each case, NPT simulations were done at three different temperatures: 300K, 1000K and 1500K for 50 Picoseconds with 0.25 femtoseconds timesteps.

(a)   (b)
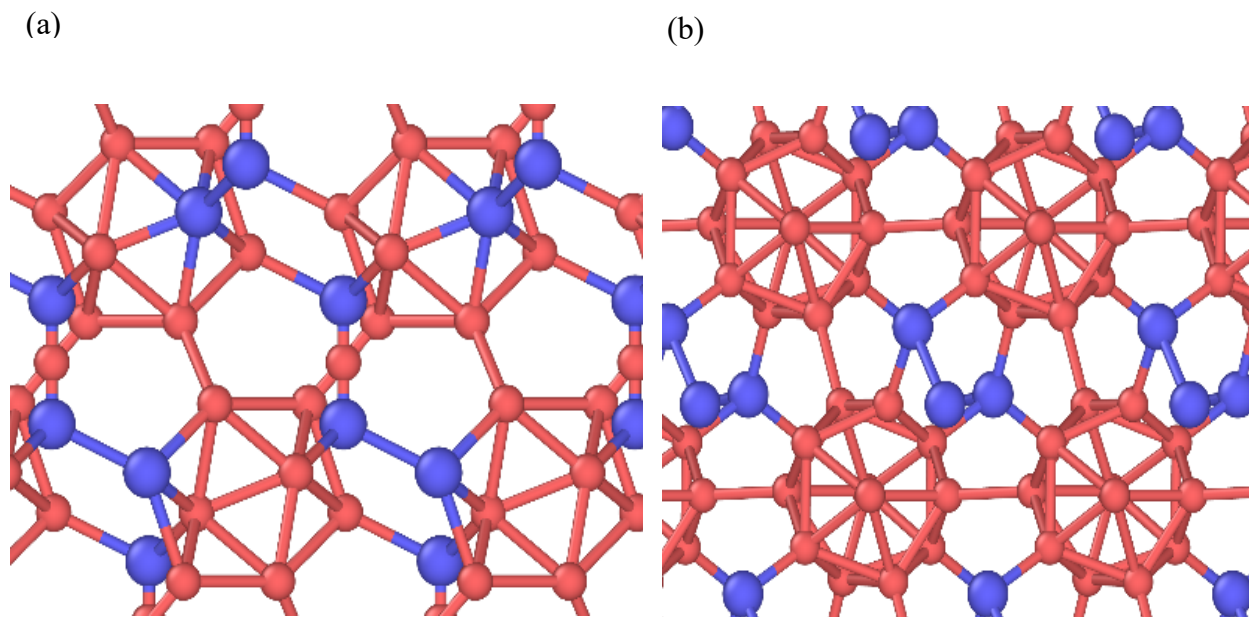
Figure 12. Crystal structure of boron carbide. (a) With CBC chain (B11-CBC), (b) With CCC chain (B12-CCC)
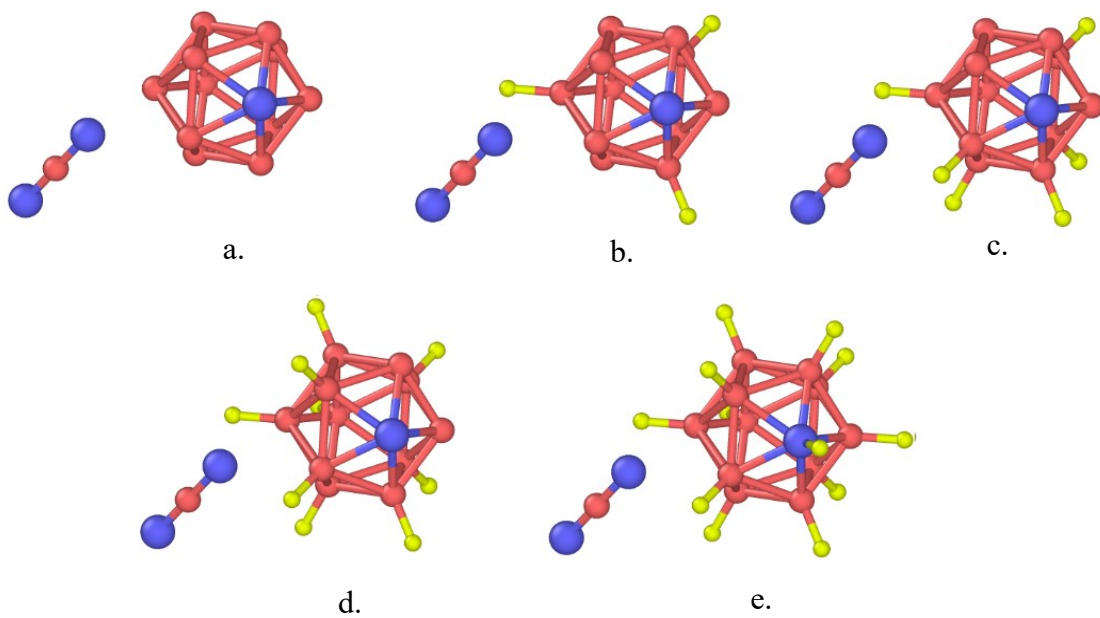
Figure 13. Unit cells of hydrogenated boron carbide with varying amount of hydrogen. a. 0%, b. 25%, c. 50%, d. 75%, e. 100% atomic percentage of hydrogen in the icosahedra with CBC chain

RESULTS & DISCUSSION

DFT Calculations and ReaxFF Potential Verification

Energy Minimization and Structural Analysis. The reactive force field we opted to use has been previously parameterized from the Quantum Mechanics (QM) calculations to reproduce structure, energy and reaction barriers [86]. It has been successfully used to analyze the mechanisms of brittle failures of non-hydrogenated crystalline and amorphous boron carbide. However, in our studies, we have orthocarborane and hydrogenated boron carbide. Additionally, one of our main focuses was investigating the chemical reactions that involved boron, carbon, and hydrogen. We started with performing energy minimization of different common and important species.

Table 1 shows the energy comparison between DFT and ReaxFF of different species. Hundreds of different species and molecular clusters were created during the ion bombardment at different times for different kinetic energy of ions. Therefore table 1 is not exhaustive but it indicates that ReaxFF provides a good description of this energy data.

Table 1. The total energy in Kcal/mole of different molecules found during bombardment as calculated by DFT and ReaxFF

Species	DFT	ReaxFF
Orthocarborane	-2986.766	-2730.7208
H2	-156.1239	-108.26742
BH3	-366.4476	-329.2619
CH4	-554.41	-428.45397
B2H4	-578.1819	-523.73947

Figure 14 shows the comparison of radial distribution function (RDF) of one orthocarborane molecule between DFT and ReaxFF. The RDF data was obtained from the relaxed structures at 0K. The figure indicates that for ReaxFF the bond lengths are slightly higher (<7%) than that of for DFT which is reasonable.

Bond Dissociation Energy. Bond dissociation energy is one of the key entities to model chemical reaction. ReaxFF has been proven useful to model chemical reaction by allowing continuous bond creation and bond breaking [87], [88]. Figure 15a and 15b show the bond dissociation curves of BH and CH respectively, of ReaxFF and DFT calculation. For both bonds, the distances were taken up to 5 angstroms. From the figures, we see that the ReaxFF data are in
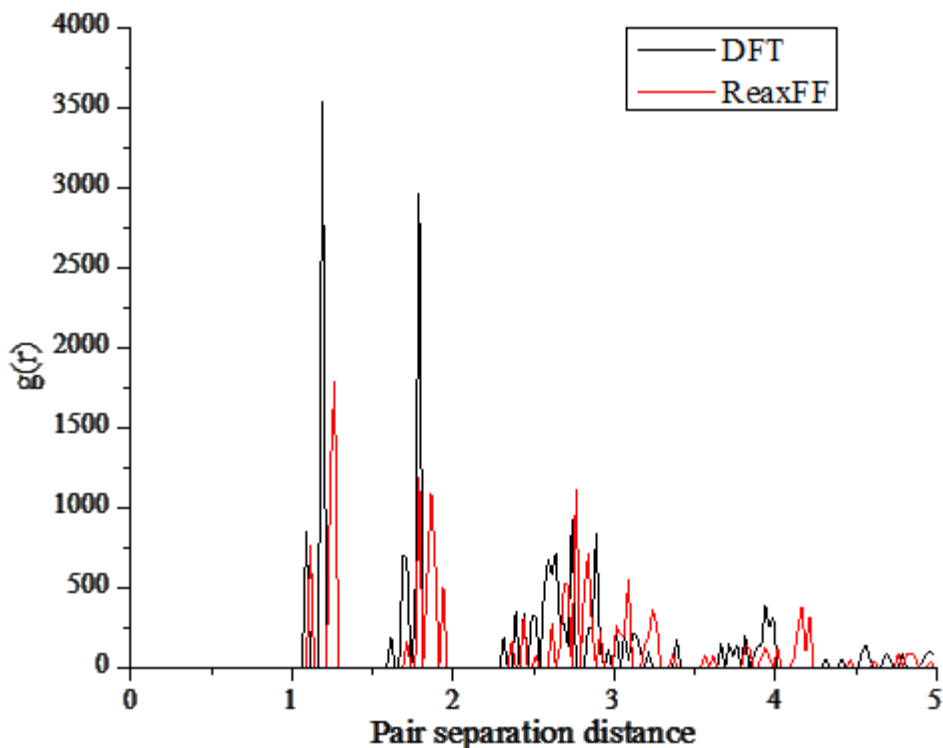
Figure 14. Radial distribution function analysis of single orthocarborane molecule using DFT and ReaxFF

good agreement with DFT results. These energies are plotted as relative energy which obtained from calculating the total energy of the system.

(a)

(b)
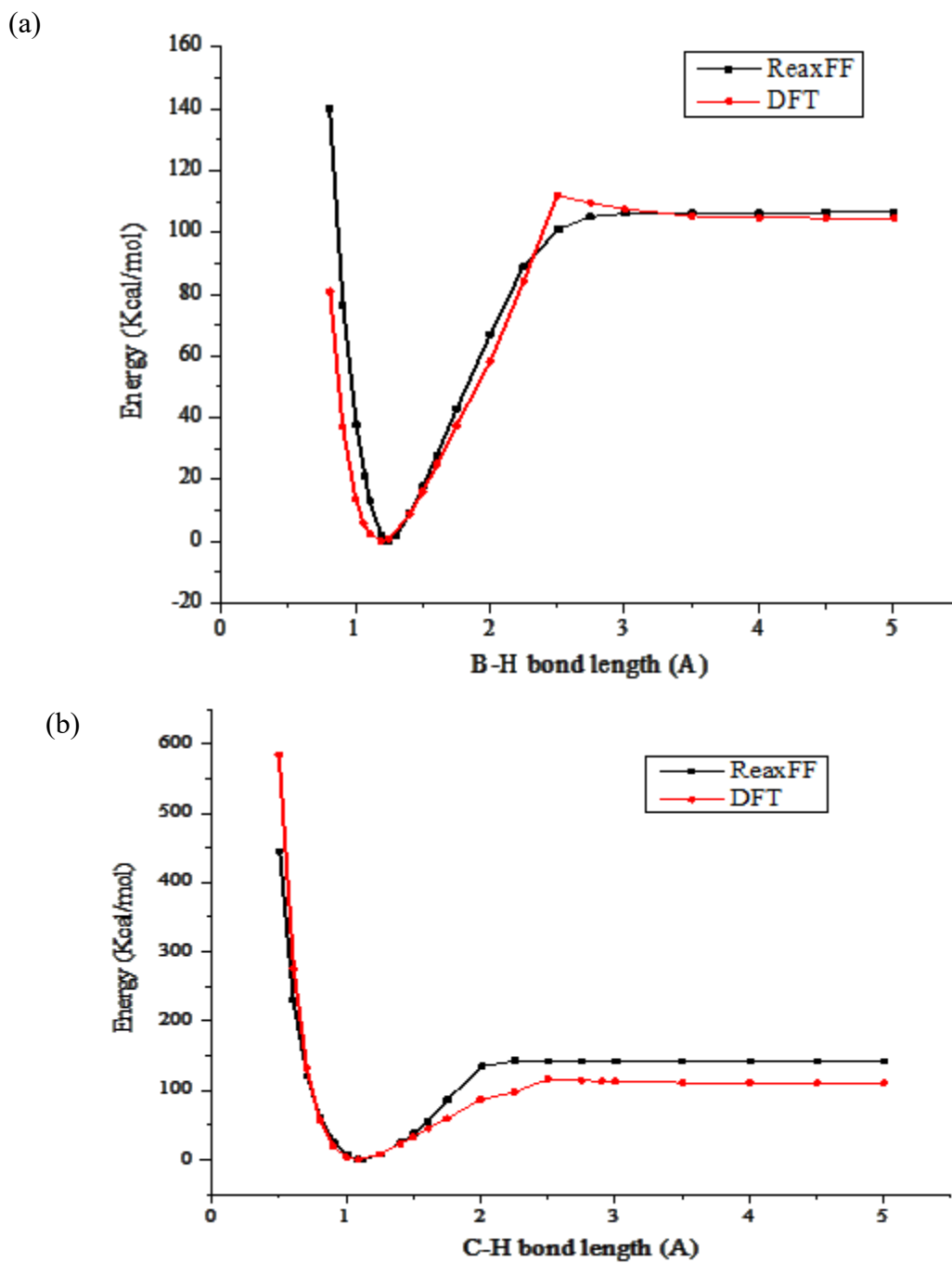
Figure 15. Bond dissociation energies calculated using ReaxFF and DFT. (a) BH, (b) CH

In additional testing, we obtained structural stability of the model of the solid crystalline phase of orthocarborane using ReaxFF. As shown in figure 16, we were able to stabilize the FCC crystal structure of orthocarborane at room temperature with a unit cell dimension ~10.9 Å, which is in good agreement with the experimental findings [30]. It should be noted that our argon bombarding structures were gaseous mixtures. However, after the bombardment, we equilibrated the bombarded structure and observed aggregation through cluster formation. The outcomes of force field testing in the solid phase of orthocarborane indicates that the force field is applicable for modeling the big clusters as well. An interesting aspect of the condensed phase of carboranes is that the phase exists due to the presence of van der Waals force [89], [90]. That implies the force field we used for our study has good van der Waals parameters.
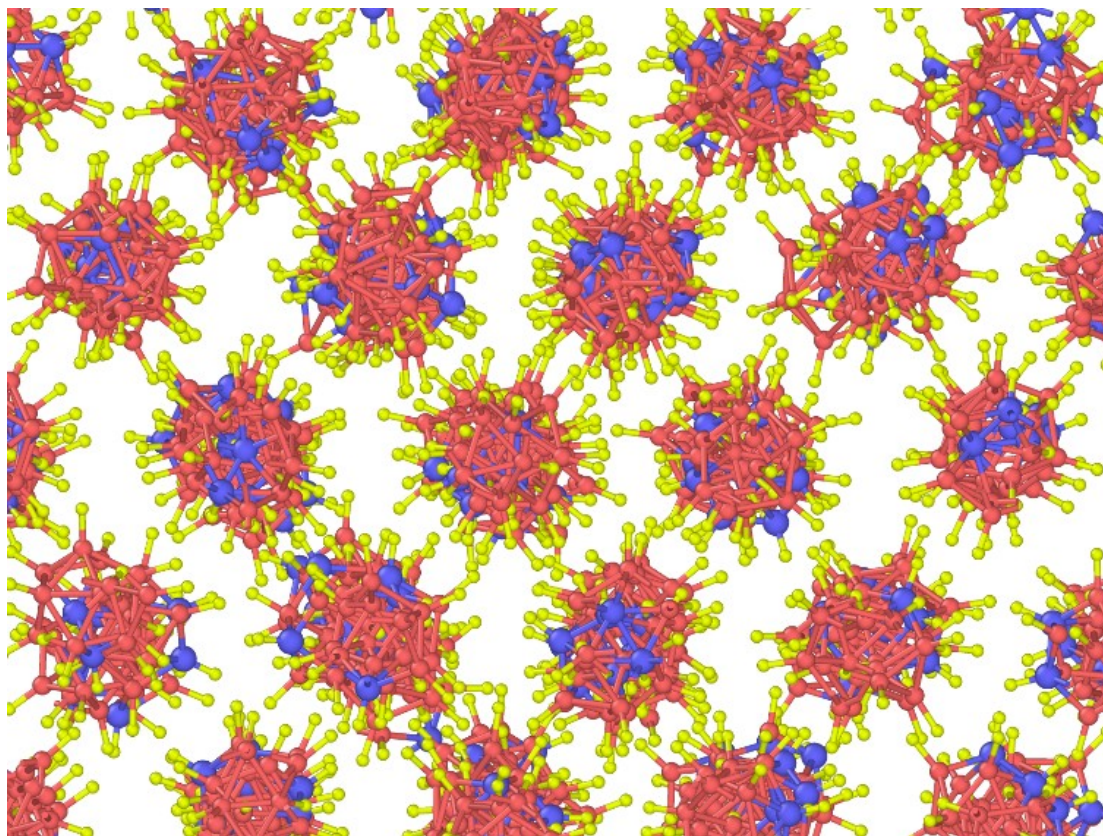
Figure 16. Crystal structure of orthocarborane obtained at room temperature using ReaxFF.

Argon Bombardment

Previously, the formation of different species due to the collision between argon and orthocarborane molecule has been shown. The types of species depend on the place of contact of the molecule and the kinetic energy of argon. For example, if an argon atom with particular kinetic energy hits directly on the boron riched area of the icosahedron, the results would be different if it hits on the carbon riched area. Similarly, if it hits in the same area of the molecule with different kinetic energy, obviously the result would be different. Mathematically, a countless number of different possibilities and outcomes exists in the process. If we keep the sample size large enough, it mostly would cover the statistics for the places of contact.

Considering the simulation resources, we chose a mixture of 1000 orthocarborane with 25 argon. In figure 17 it has been shown the different outcomes with changing the kinetic energy of argon while keeping the place of contact same. It should be noted that in the structure of amorphous hydrogenated boron carbide the icosahedral structure is found in abundance along with carbon-boron chains of different length [27], [82], [84], [85], [91]. Therefore, in our model, our goal was not to destroy all the icosahedral structure, rather destroy some of them and hence produce some active species that would lead to making connections between the icosahedral species. Figure 18 depicts the destruction of icosahedral species quantitatively with time for varying argon energy. The figure 18 shows for 100 eV around 10% orthocarborane molecules were broken or damaged after 5 ps. Whereas, more than 800, i.e. 80% were collapsed for 600 eV. For both quantitative and qualitative understanding of the formed species, we did several analyses. We started from the pair distribution function (PDF) analysis.

PDF Analysis. We took the structural data of simulation cells at different times and performed PDF analysis. In figure 19a and 19b the PDF of HH pairs has been presented at
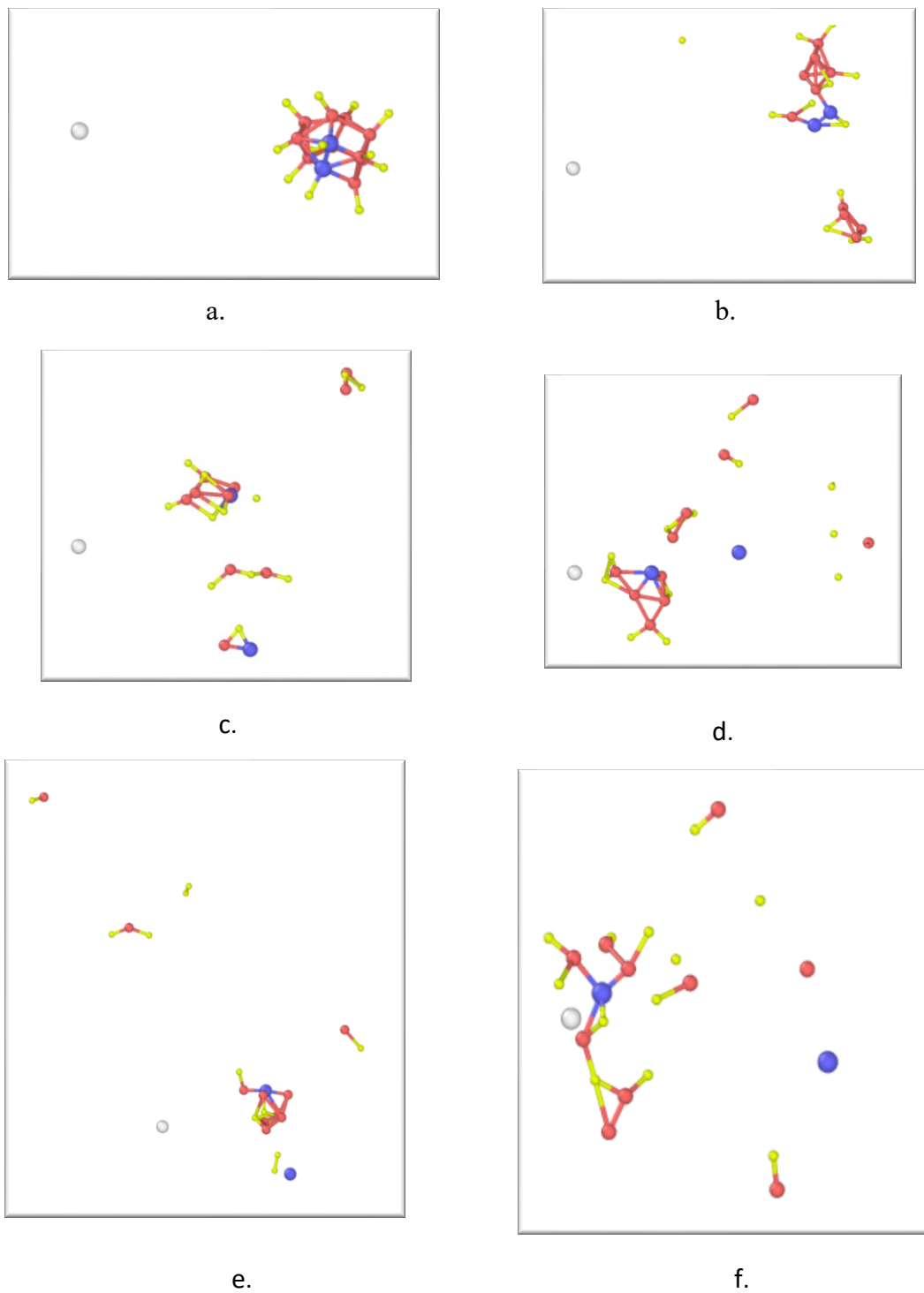
Figure 17. Comparative results after collision for different argon kinetic energies: a) 20 eV, b) 50 eV, c)100 eV, d)200 eV, e)400 eV, f) 600 eV.

different times for 25 argon atoms with 600 eV and 200 eV kinetic energy respectively. Initially, at 0 ps, a few groups of dominant peaks were observed. The BH and CH bond lengths are not the same (~1.27 angstrom and ~1.13 angstroms). This alters the distances between hydrogens of two neighboring BH, or BH and CH, or neighboring CH, and it explains the three peaks in a group. In addition, the icosahedral structure in orthocarborane is slightly distorted from regular icosahedron due to the presence of carbon atoms in the molecule. The other peak is due to the distortion of the icosahedral structure. It should be noted that the first group is between 2-4 angstrom and the second group is 4-6 angstrom. After the bombardment began, the gradual attenuation of these peaks refers to the destruction of part of the icosahedral structure. The high-energy argon atoms increased the temperature of the simulation cell, and this resulted in the delocalization of the predominant peaks. Additionally, a previously absent peak was formed at
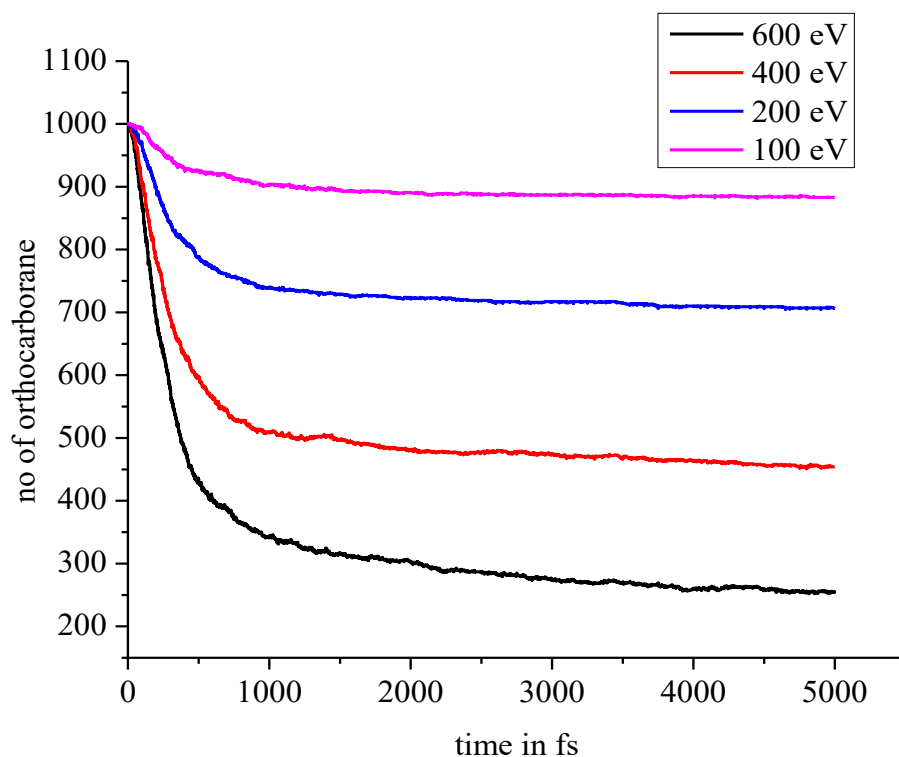
Figure 18. Time evolution of no of orthocarborane molecules for different argon energy

around 0.75 angstroms. This peak was due to the presence of hydrogen molecules resulting from

bombardment. It should be noted that no hydrogen-hydrogen bond was present initially. Another
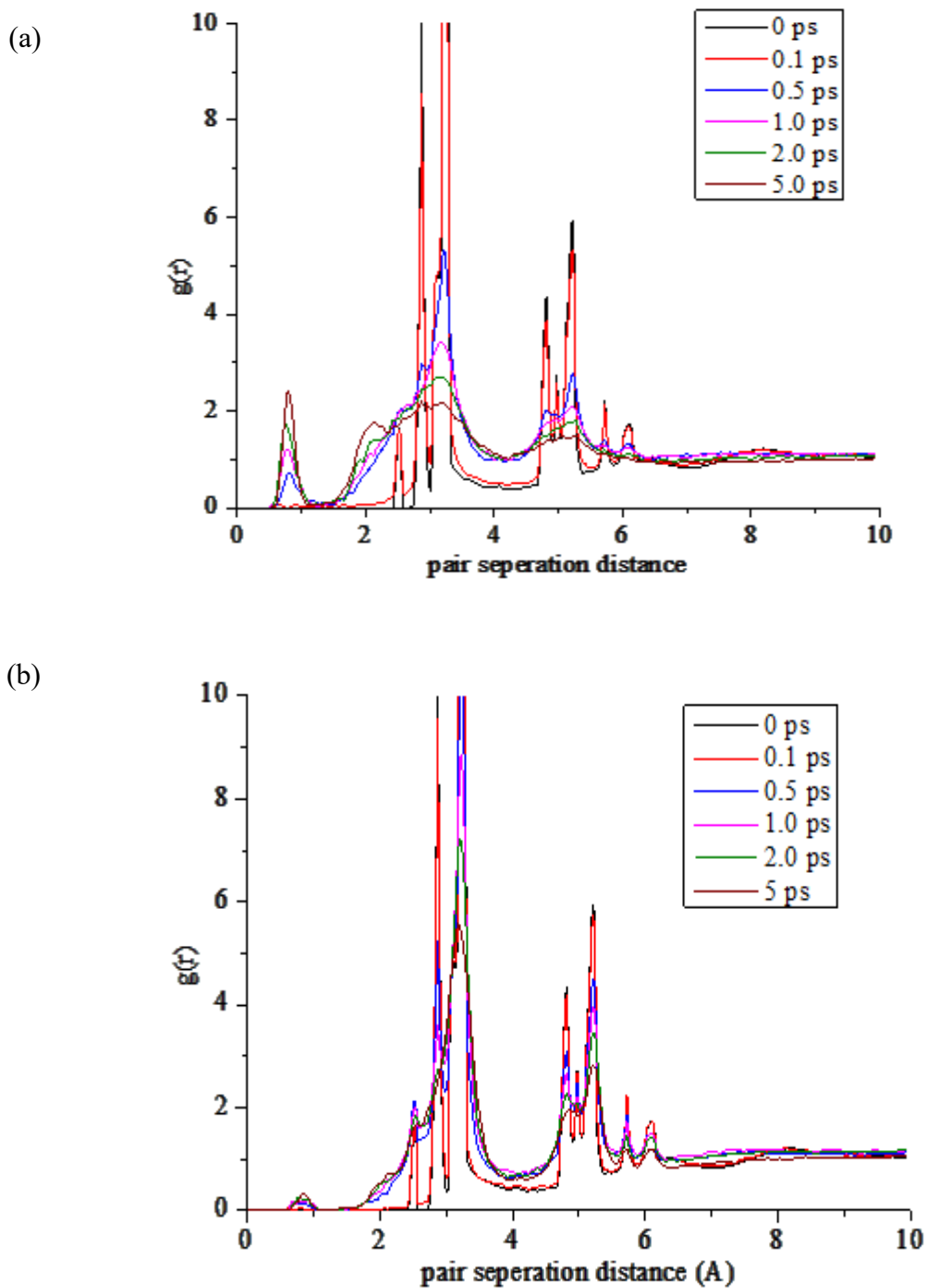
Figure 19. Time evolution of PDF of HH pair for different kinetic energy of argon: (a) 600 eV, (b) 200 eV

peak, more obvious in figure 19a, was less localized and shorter, at around 2.1 angstroms. This

peak came from the hydrogen neighbors of BH_3 [92]. This peak became more obvious after

chilling it to room temperature, as shown in figure 20. This gaseous BH_3 could be one of the

missing species predicted in experimental research [27]. Compared to 600 eV for 200 eV the

newly formed peaks are significantly shorter and almost indistinguishable prior to equilibration.

The first group of peaks became one wide peak but remained dominant. Even the second group

of peaks are more distinguishable than H_2 and BH_3 peaks. Both results indicate the relative

damage done with 200 eV argon energy with 600 eV. For 200 eV energy, the shapes of

orthocarborane molecules were distorted, but most of the icosahedra were intact; very few were

broken and produced hydrogen and other species. In figure 20 we observed four distinguishable
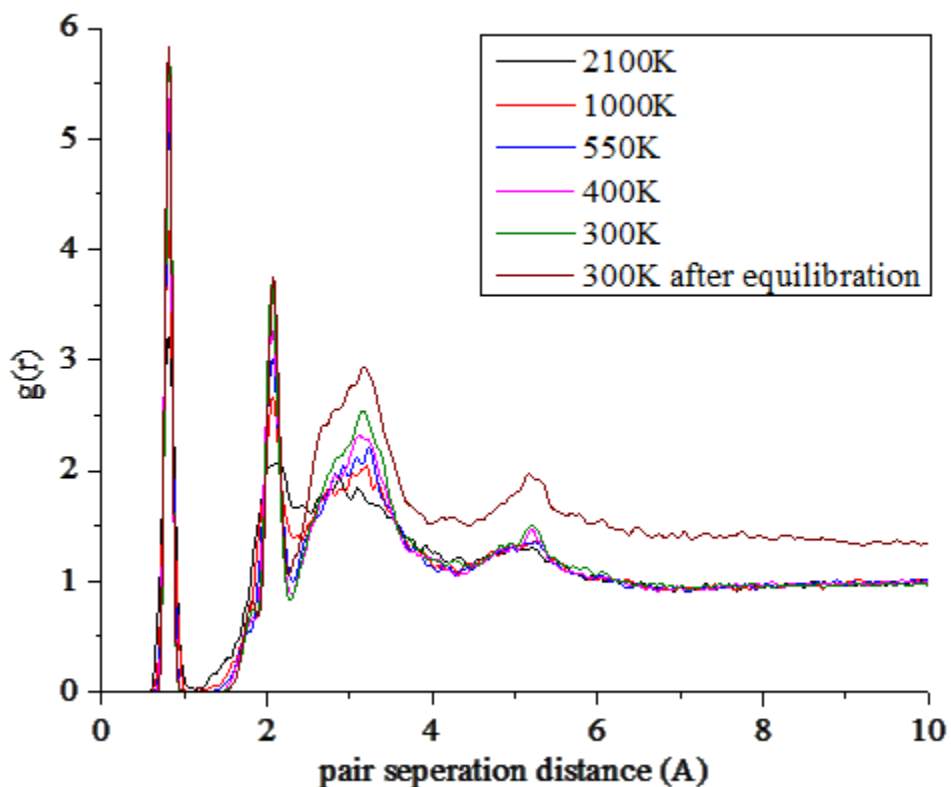
Figure 20. PDF of HH pair during cooling down at room temperature for 600 eV

peaks in total. The first and second peaks became dominant after chilling, whereas the third and fourth peaks became wider and shorter. Another important aspect of the figure 20 can be seen in the PDF curve following equilibration. This curve is higher than other lines, both at the peaks and elsewhere within the range, indicating densification of the structure as a whole upon equilibration.

For the PDF of the BH pair, the smaller peaks around 2.5 and 3.8 angstroms, as shown in figure 21 can also be explained by the distortion in the icosahedral structure and the length of BH and CH bonds. This analysis supports our previous analysis with the HH pair. Excluding the first peak, all other peaks gradually attenuated with time for 600 eV argon energy. These results refer to the extent of damage of the icosahedral structure after bombardment happens for the particular
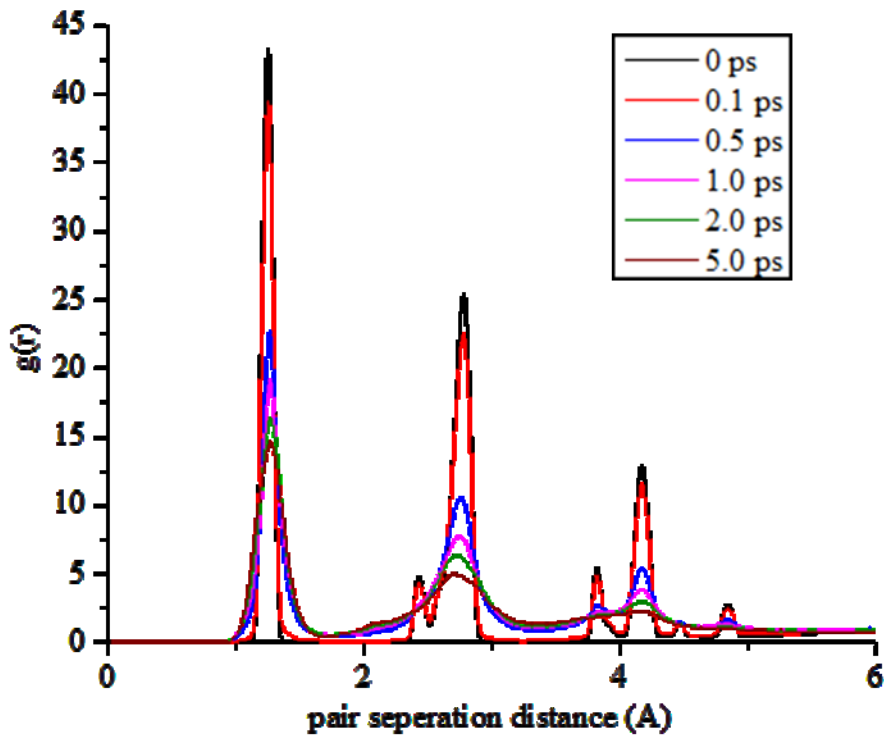
Figure 21. Time evolution of PDF of BH pair for 600 eV

argon energy. Presence of the first peak refers to the presence of significant amounts of BH

bonds in the structure, and attenuation of other peaks refers to the breakage of the cage structure.

From the BH pair distribution, similar conclusions can be drawn to HH pair for 200 eV

argon energy as shown in figure 22. After 5 ps of bombardment with 200 eV initial energy

level of argon, the attenuation of the peaks is significantly less when compared to 600 eV. This

shows that the cage structure remained intact after the bombardment, but the significant

attenuation of the smaller peaks at 2.4 and 3.8 angstrom demonstrates that the energy was strong
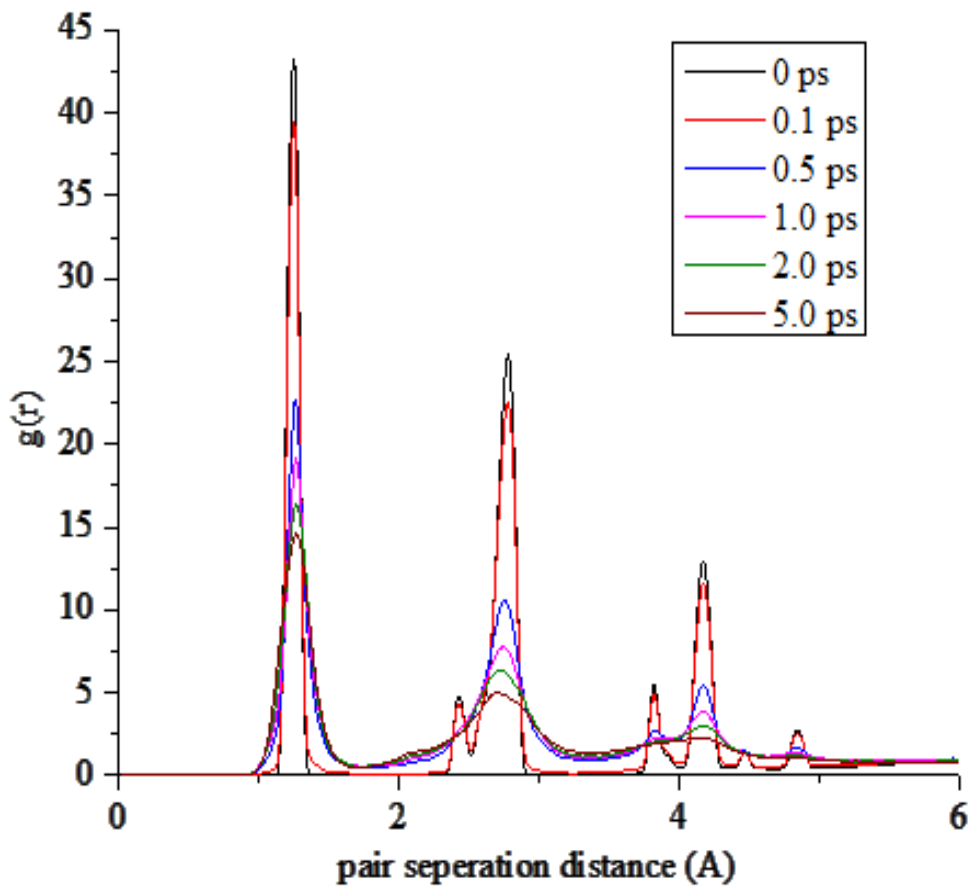
Figure 22. Time evolution of PDF of BH pair for 200 eV

enough to delocalize the bond length of BH and CH. The energy was strong enough to distort the

cage structure of most of the molecules but could not break a significant number of those.

The figure 23a and b shows the result of the HH and BH pair's PDF analysis respectively

with changes in argon energy. These two figures summarize the impact of the change in argon

energy in the bombardment process. For HH pairs, with the change in energy, the peak for H_2

and BH_3 increased around 0.8 and 2.1 angstrom, respectively. A small peak just below 2

angstroms was found for 600 eV, which was formed from clusters where carbon atoms

connected with multiple hydrogen atoms. The other peaks attenuated as per the previous

explanation: breakage of the cages. Similarly, for BH, the peaks around 2.75 and 4.2 angstroms

attenuated with increased energy. A tiny peak just above 2 angstroms was formed only for higher

energy argon (400 to 600 eV). The three-dimensional orientation of hydrogen atoms connected

with boron and carbon is different in orthocarborane and other smaller clusters. The bond angle

between CBH, BBH, CCH or BCH changed slightly in the smaller clusters compared to

orthocarborane. This results in a smaller peak above 2 angstroms, as mentioned above.

Other pair distribution analyses, namely on BC, CH, BB, and CC, showed results that can

lead to similar conclusions as those from BH and HH. Yet these results have their own

importance. For example, as shown in figure 24 the graph of PDF of CC pair after the NVT

equilibration at 300 K for all energies, a new peak around 1.22 angstrom was observed. It should

be noted that the most dominant peak for CC here was around 1.67 angstrom. In fact, this was

the only peak initially for CC pair at the beginning of the bombardment. This was due to the

absence of second or higher order nearest neighbors of carbon atoms in the orthocarborane

molecule. Surprisingly, the newly formed peak was found far below the initial peak. This peak

increased in height with an increase in argon energy. This points to a quite plain and illuminating

(a)

(b)
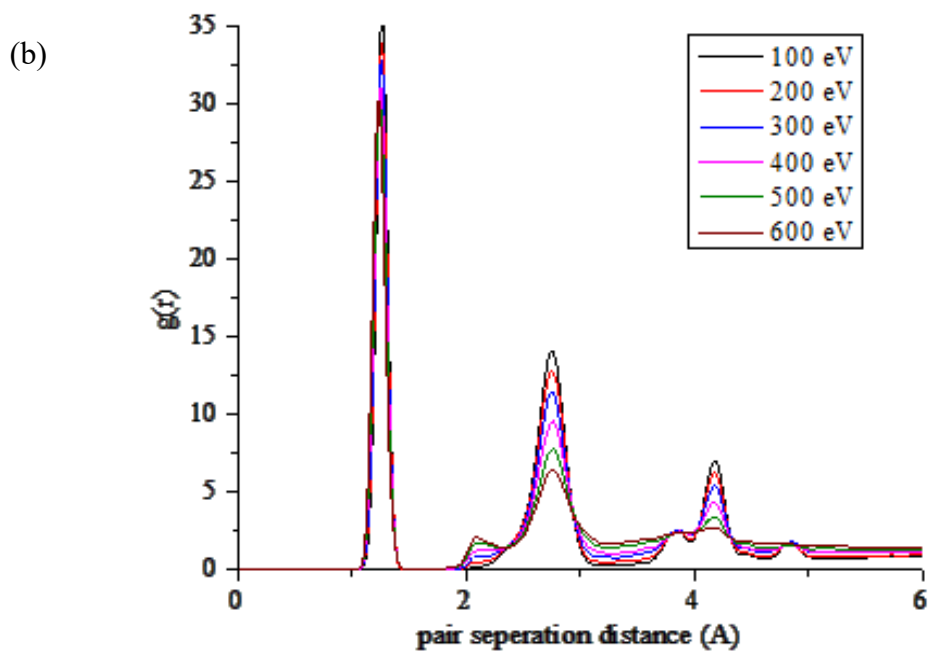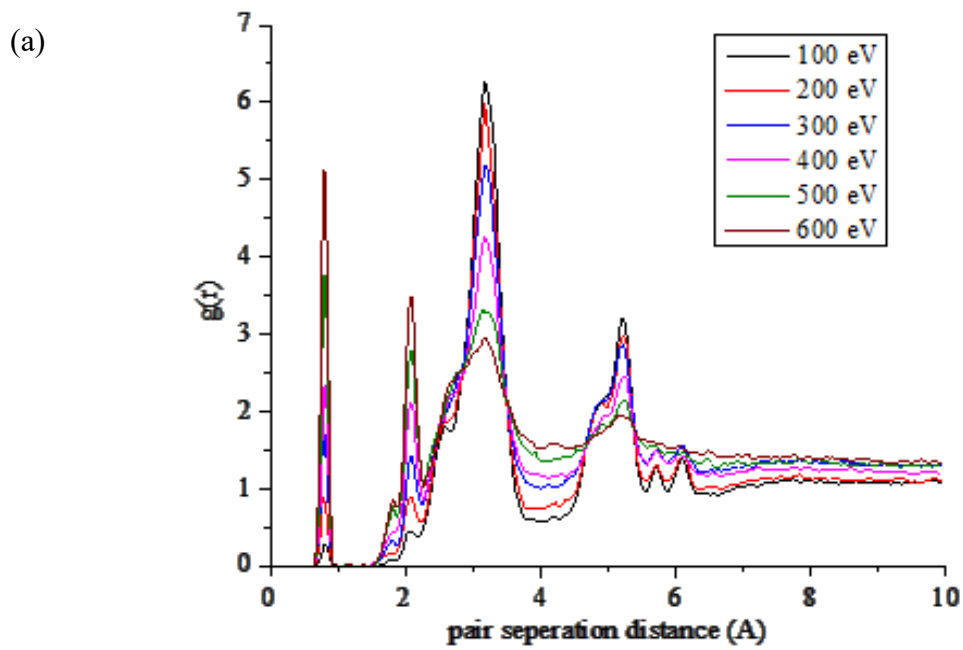
Figure 23. PDF of (a) HH and (b) BH pair after equilibration at room temperature for different argon energy.

the fact that when the icosahedra were broken and in the newly formed and smaller clusters, the

CC bond length is smaller than the CC bond length in the icosahedra.
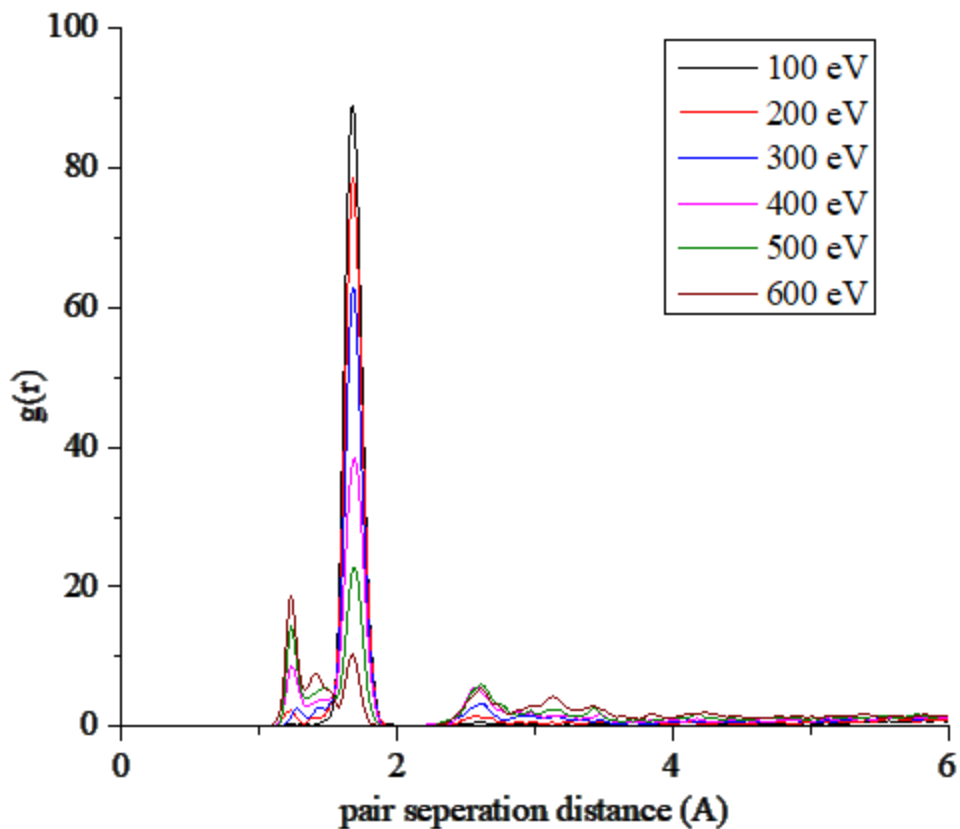
Figure 24. PDF of CC pair after equilibration at room temperature for different argon energy

Species Calculation. In this part of our studies, we analyzed the formation of species due

to bombardment. We showed earlier that, when a high-energy argon atom collides with an

orthocarborane, different kinds of species and clusters form. Here we quantitatively and

qualitatively studied the formed species. We will refer to different simulation during the

discussion as the kinetic energy of argon atoms at the beginning of the bombardment. For

instances, the particular simulation for which the bombardment was started with assigning 400 eV kinetic energy to all of the 25 argon atoms will be referred to as a 400 eV simulation.

We have calculated bond order values to determine chemical bonds. The bond order calculations were performed using the built-in method of ReaxFF in LAMMPS (reax/c/species). Figure 25 shows the initial species count for all of the simulations of argon bombardment. In the beginning, we put 1000 orthocarborane molecules and our species count further verifies the results obtained from the opted method.
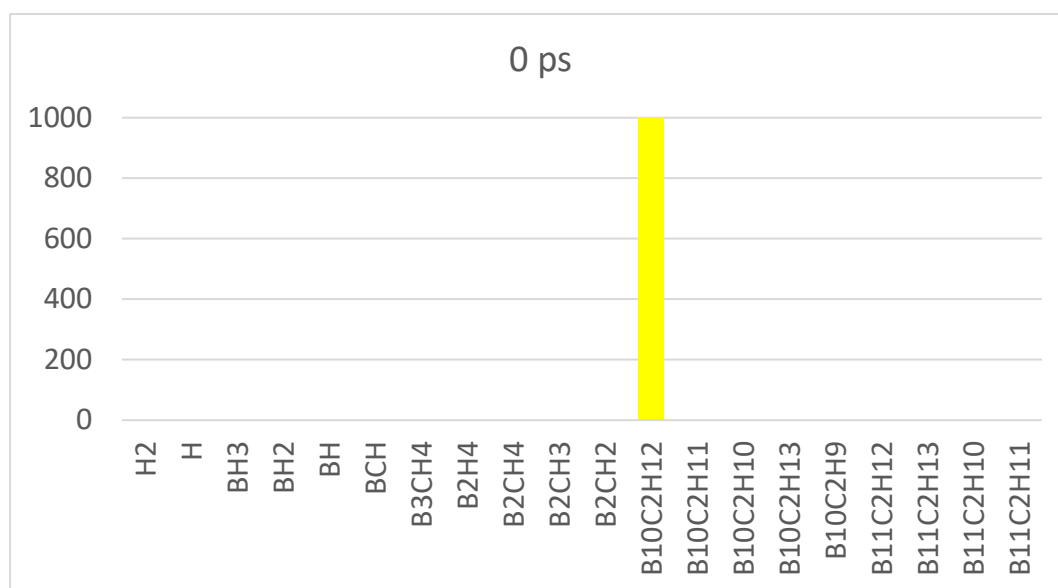
Figure 25. Initial species count for all of the simulations of argon bombardment.

Figure 26 shows the most common species found including small clusters, free radicals, orthocarborane and bigger clusters at a different time for 600 eV. 600 eV is the highest kinetic energy we have used for argon and we found within 1 ps a considerable amount of hydrogen in the simulation cell. The figure indicates most of the hydrogen produced at the beginning and the number grew slowly but consistently over time. More than 300 molecules of hydrogen (more than 5% of total hydrogen) were found after 5 ps of bombarding and the quantity was unchanged
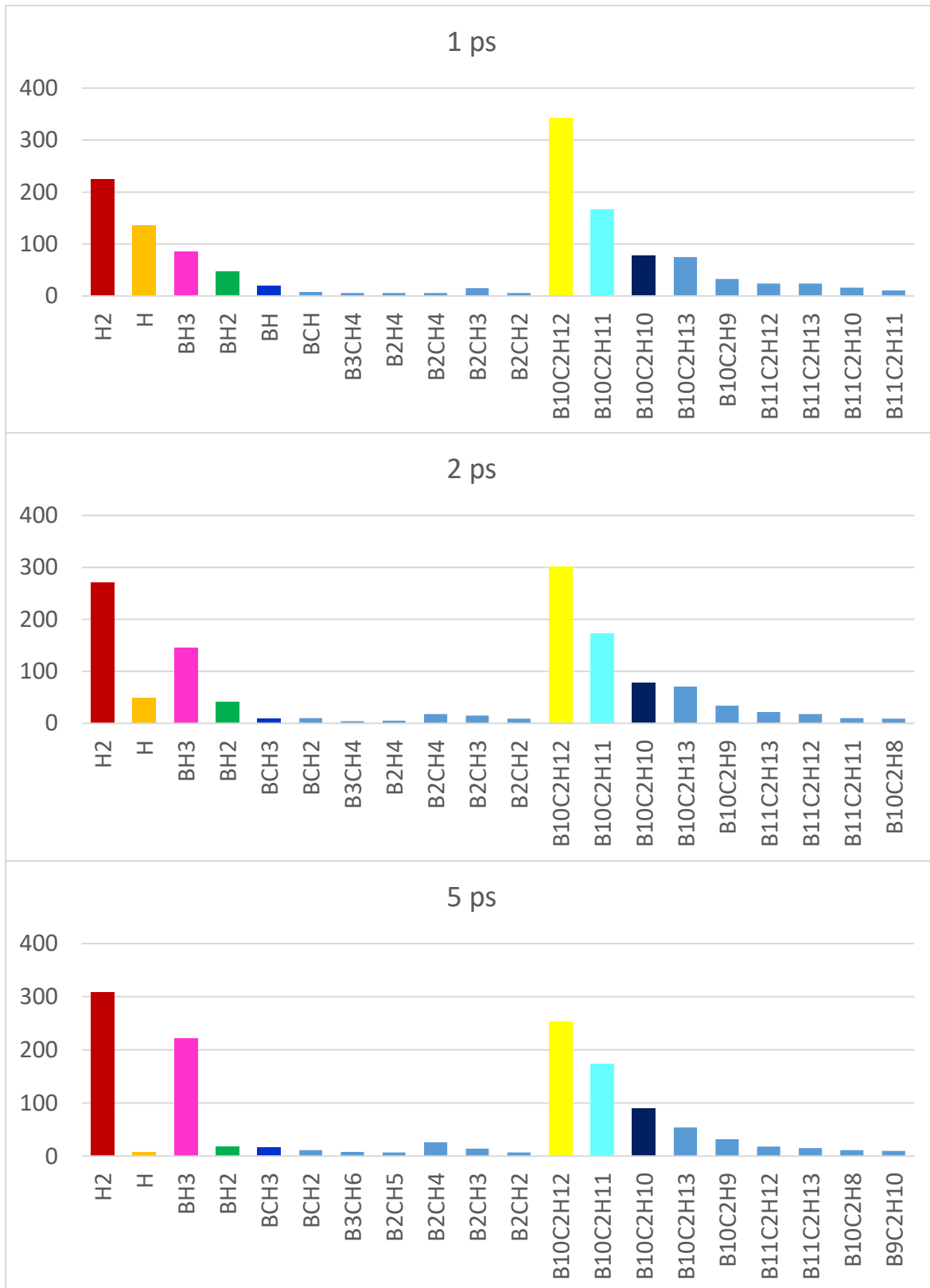
Figure 26. Different species count at different times for 600 eV
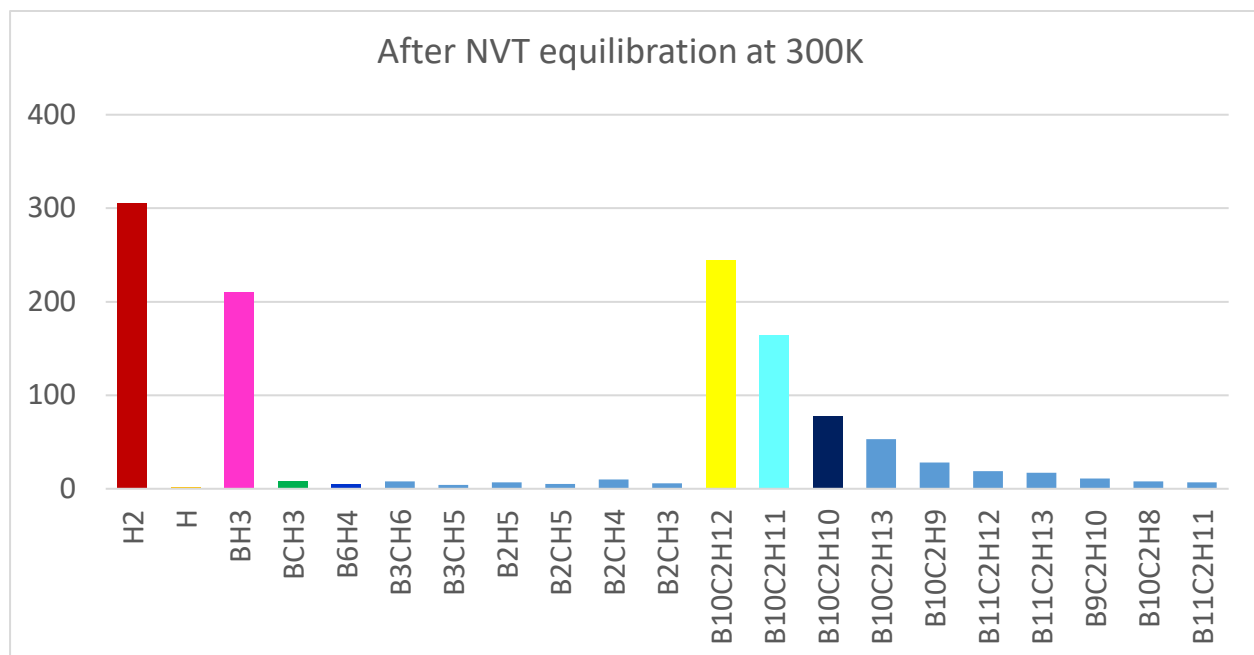
Figure 26 (continued). Different species count at different times for 600 eV

after equilibration at room temperature. Whereas, initially lots of isolated H atoms were found

which are chemically very active, therefore very unstable. The number of H decreased drastically

and disappeared at the end of NVT. The trend of BH_3 was similar to H_2 and consistent at all time.

However, the active free radicals like BH and BH_2 followed the trend of H atoms and

disappeared after equilibration. Most likely, species like BH and BH_2 connected with free H and

ended up transforming into BH_3. Similarly, two hydrogen atoms produce H_2 molecules.

Metastable species like BCH, B_2CH_2, B_3CH_3, B_2CH_4, B_3CH_4, and others found in small numbers.

Most likely, clusters like BCH and BCH_2 formed from direct collisions between argon and

orthocarborane. The others were created depending on the availability of isolated B, C or H

atoms and small radicals in the vicinity of BCH and BCH_2. Analyzing the trend of the bigger

clusters, we observed the number of orthocarborane dropped to around 33% of its initial count

within 1 ps. Most likely, the molecules lost few of the hydrogens and hence the other common

clusters like $B_{10}C_2H_{11}$, $B_{10}C_2H_{10}$, and $B_{10}C_2H_9$ evolved. The loss of hydrogen could happen due to direct collisions or very active species like B, BH, C, and CH pulled out hydrogen when came close enough to the orthocarborane molecules. The second phenomenon is verified from the outcomes of the study of the interaction between free radicals and orthocarborane.

Figure 27 shows the complete time evolution during the bombardment for some of the important free radicals, molecules, and clusters. Now it is more obvious how the different active species evolved after the initiation of high energy ion bombardment. Additionally, how quickly their numbers declined refers to the stability and reactiveness of corresponding species. In figure 27a, we see the number of B, H, BH, and BH_2 first grew and then declined at a different rate. All of these are chemically reactive species. On the other hand, H_2 and BH_3 which are chemically stable. Therefore, their numbers increased consistently over time. Without sufficient external kinetic disturbance, they remained intact following formation. At equilibrium, BH_3 forms a stable 2D planar structure [92]. Figure 27b shows some of the most common bigger clusters including orthocarborane molecule. It should be noted that the species counts are plotted in logarithmic scale. We investigated the correlations between the species that shown later part of this section.

Figure 28 shows similar data for 400 eV simulation. The trend is very similar to 600 eV. However, as the argon energy is less than before, a smaller number of orthocarborane molecules were damaged. Consequently, the number of other species were less for the corresponding time frame. After 5 ps around 45% orthocarborane were intact. Stable species like BH_3 and H_2 were almost 50% less compared to 600 eV. Similarly, we found some smaller clusters like BCH_2, BCH_2, B_3CH_6 and so on. Again, the bigger clusters like $B_{10}C_2H_{11}$, $B_{10}C_2H_{10}$, $B_{10}C_2H_9$, $B_9C_2H_9$ and others were found in almost identical trend as 600 eV in different time frames.

a)

b)
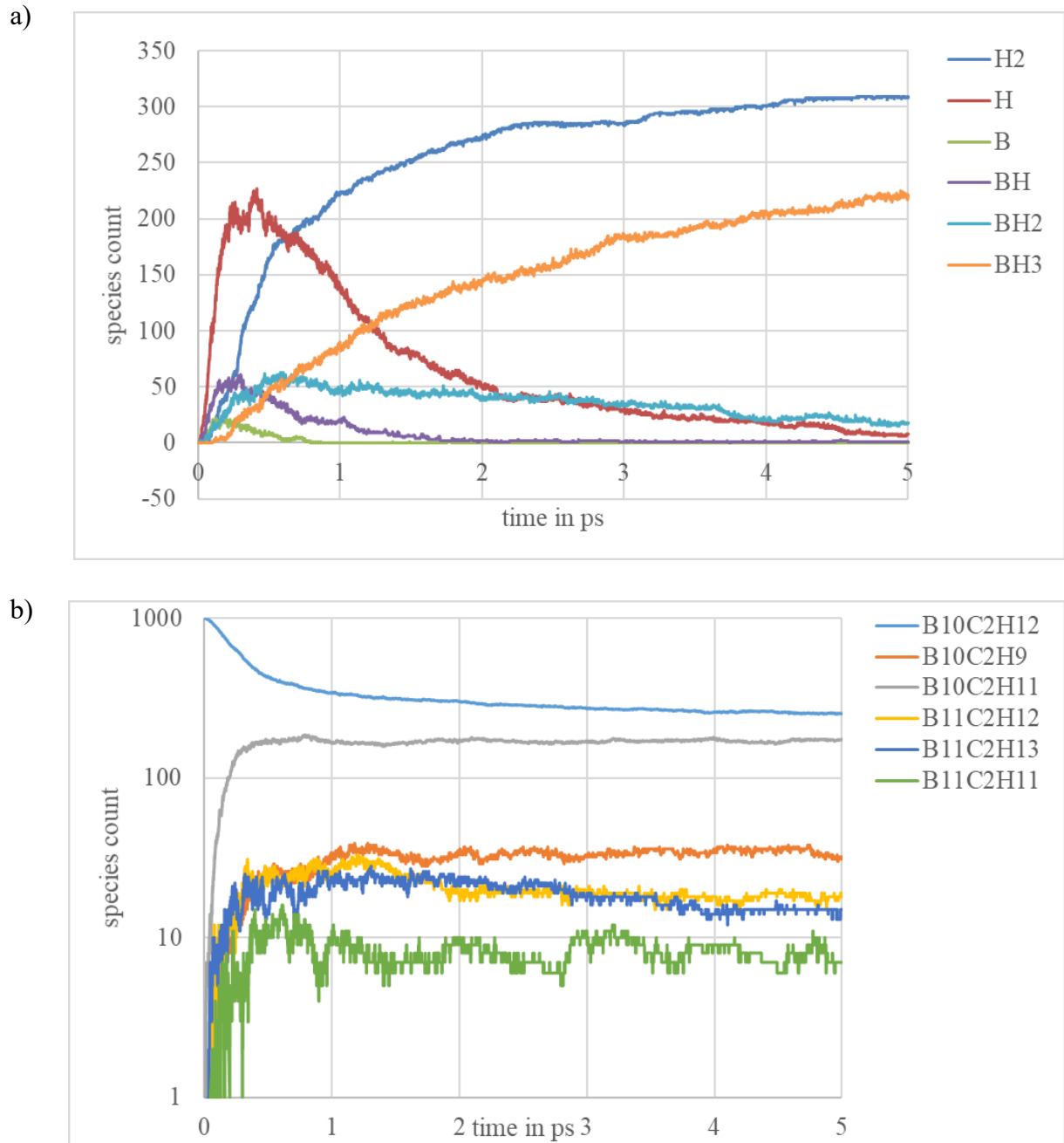
Figure 27. Time evolution of different species for 600 eV: a) smaller species, b) bigger clusters

Species Data Analysis. As it is shown in previous section that during bombardment the types of found species are of wide varieties. Additionally, with time new types of species formed

and lots of unstable and metastable species disappeared. Primarily our goal was to find the

correlation between the argon energy and formed species and hence finding a relationship with
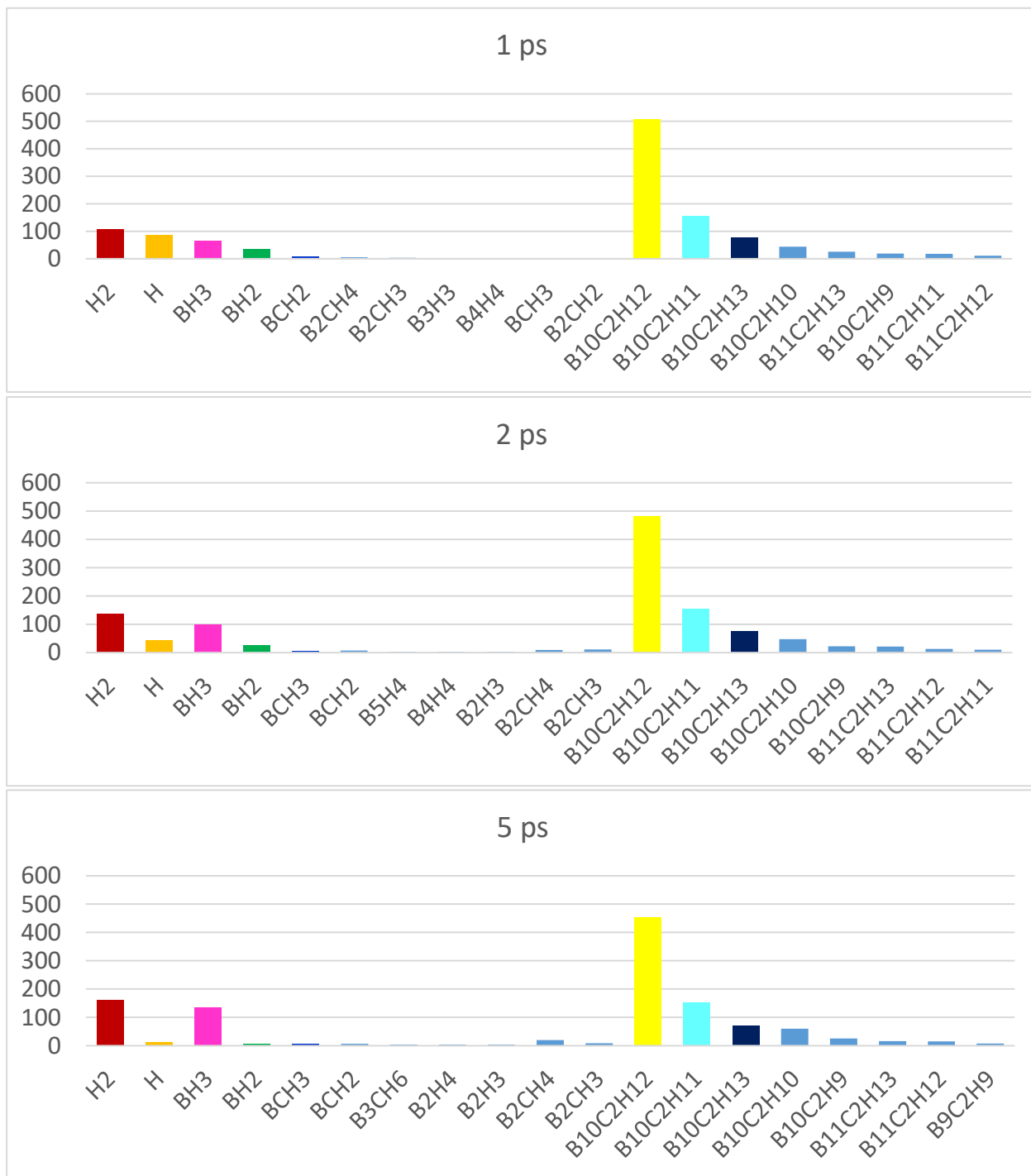
Figure 28. Different species count at different times for 400 eV
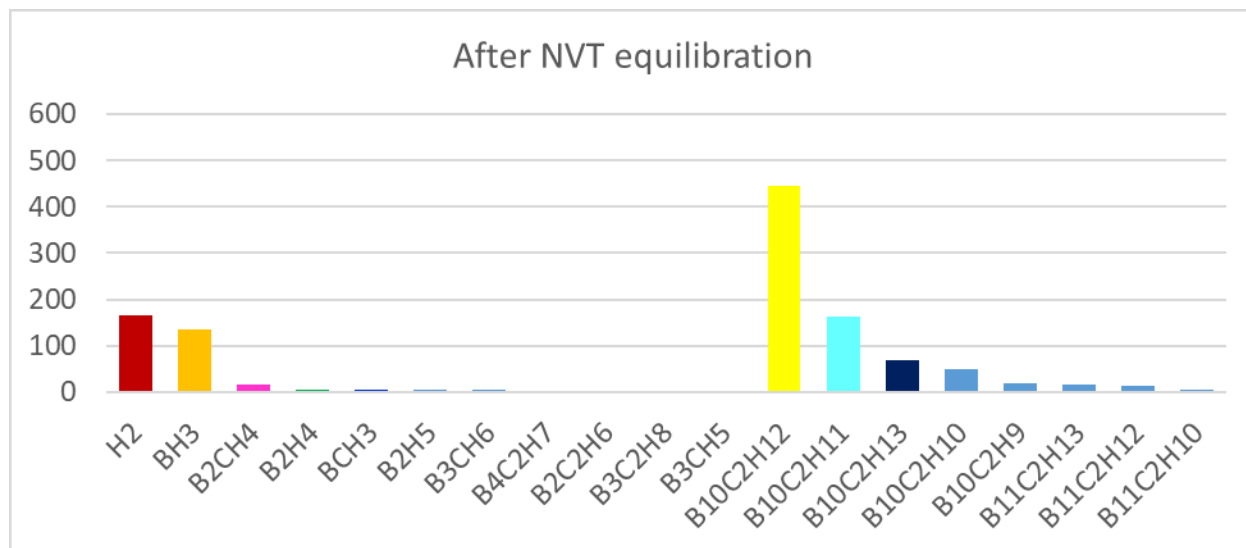
Figure 28 (continued). Different species count at different times for 400 eV

the final product. This is because for different simulations we only varied the argon energy. The

number of orthocarborane and Ar were kept same. However, the obtained correlation only with

argon energy failed to predict the outcomes up to the expected accuracy. One can argue that the

formation of the species happened solely due to the ion bombardment on orthocarborane

molecules, at certain stage of the simulation the formation of new species also greatly impacted

by the presence of other species. This is true in the sense that most of the kinetic energy of the

bombarding ions was transferred to the molecules within first few ps. Later, the chemical

reactions between the temporary species played the role of formation of other species.

We took some of the most common species throughout the bombardment along with

argon energy and calculated the correlation between them. We chose $B_{10}C_2H_{11}$, $B_{10}C_2H_{10}$,

$B_{10}C_2H_{12}$ (orthocarborane), H_2, BH_3 and argon energy to calculated how the species count

correlated with each other and with time. These calculations were done using the software called

WEKA [93]. It is mostly used for data mining purpose [94]–[97]. WEKA is an open source code

embedded with several machine learning algorithms. It also has a collection of mathematical approaches like linear regression, multilayer perception to find correlation. We have used the linear regression method with full training sets for our study. Figure 29 shows the actual and predicted data obtained using this approach for orthocarborane molecules. From the visualization we see the predicted data are in good agreement with the actual data.
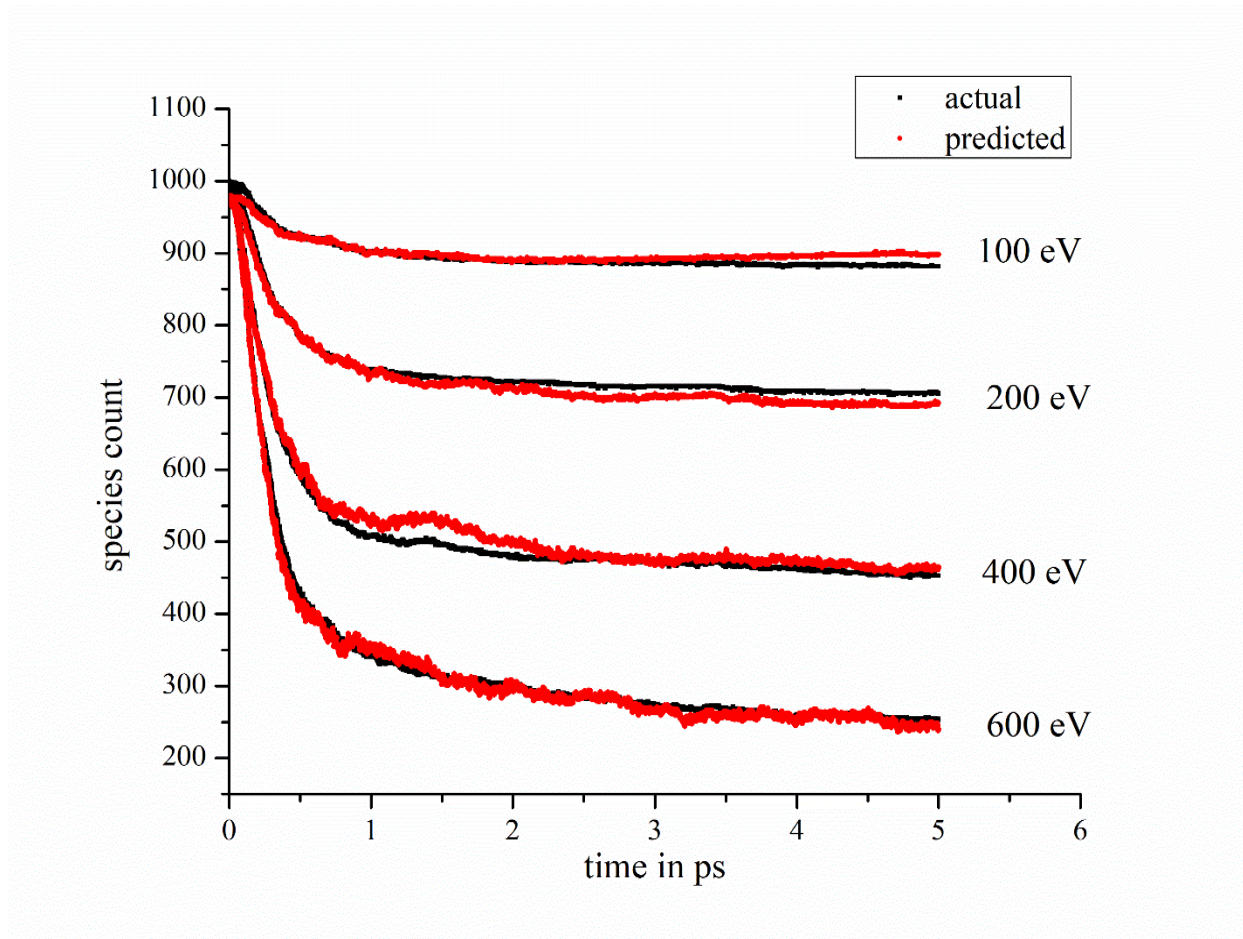
Figure 29. Correlation between the time of evolution of the number of orthocarborane and other parameters.

The following linear regression model describes the correlation with the other parameters.

$$B10C2H12 = 0.0002 \text{ X Timestep } -1.7942 \text{ X } B10C2H10 -1.7962 \text{ X } B10C2H11 -0.219 \text{ X } BH3 -0.7727 \text{ X } H2 + 979.2717$$

56

It should be noted that there were lot more other species which might not significant individually but altogether they had nontrivial impact. The number of all other species negatively related with the number of orthocarborane. We expected the timestep should be also inversely related with the number. However, from the graph we see the nonlinear relationship between timestep and the number of orthocarborane and after 1 ps the curve became almost flat with time. As we consider the total 5ps of the data the impact of timestep became very small in the regression model. Table 2 shows the statistical outcomes of the regression model.

Table 2. Summary of the statistical results of the regression models of orthocarborane

Parameters	values
Correlation coefficient	0.9986
Mean absolute error	9.89
Root mean squared error	12.1883
Relative absolute error	4.6783%
Root relative squared error	5.2269%
Total Number of Instances	40004

Similar to orthocarborane figure 30 shows the actual and predicted data for two other important species H_2 and BH_3 respectively. The linear regression models are as follows

$H2 = 0.0043$ X Energy - 0.0002 X Timestep - 0.4473 X B10C2H12 + 0.7928 X B10C2H10 - 1.021 X B10C2H11 + 0.4576 X BH3 + 444.2851

$BH3 = 0.0037$ X Energy + 0.0005 X Timestep - 0.1763 X B10C2H12 - 1.6066 X B10C2H10 - 0.0652 X B10C2H11 + 0.6362 X H2 + 160.4969
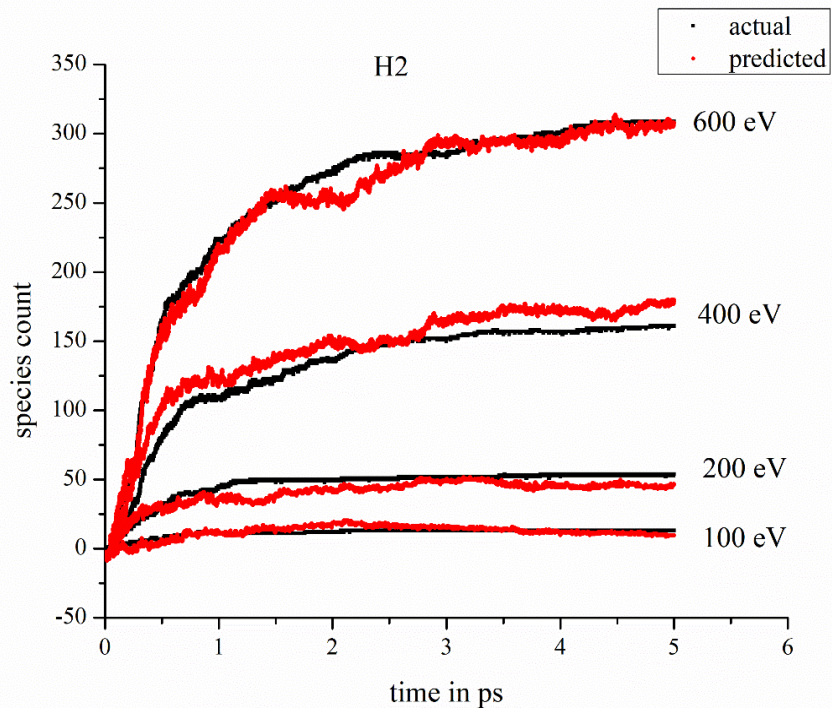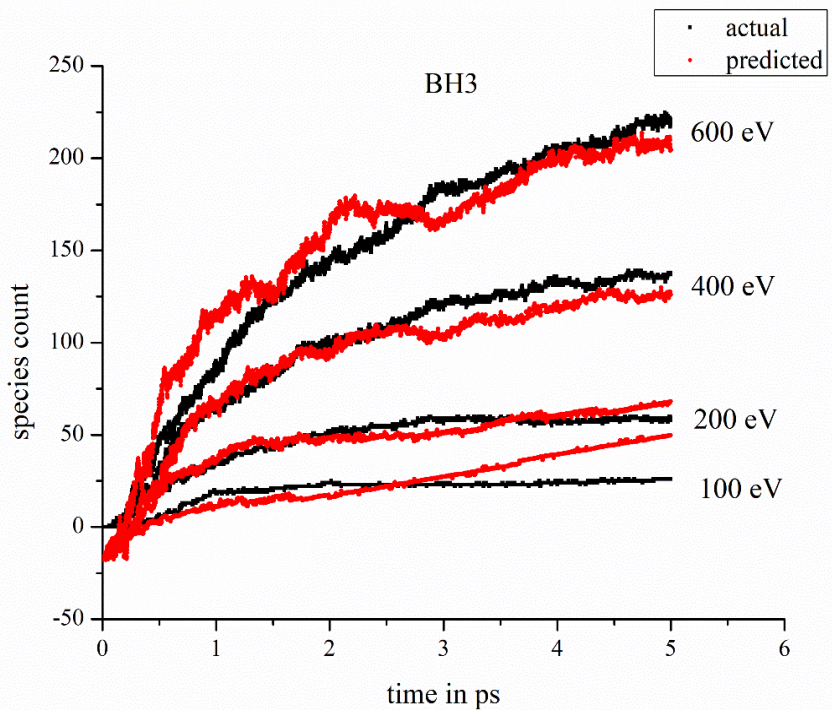
Figure 30. Correlation between the time of evolution of the number of a) H_2, b) BH_3 and other parameters.

The impact of timestep is very small for both of the models- identical to orthocarborane. The impact of energy and other species is consistence for both of them. The number of orthocarborane and others significant bigger clusters are negatively related with the number of BH_3 and H_2. Whereas, the relationship between themselves is positive. This is true in the sense that both of them increased simultaneously with time and argon energy. Additionally, formation of either one did not directly impede the formation of the other one. Table 3 shows the statistical outcomes of the regression models.

Table 3. Summary of the statistical results of the regression models of H_2 and BH_3.

	H_2	BH_3
Correlation coefficient	0.9959	0.9839
Mean absolute error	7.3201	8.5937
Root mean squared error	9.272	10.9331
Relative absolute error	8.2811%	16.4169%
Root relative squared error	9.0877%	17.8482%
Total Number of Instances	40004	40004

Orthocarborane with Free Radicals

It is mentioned before in the computational details that in this step of our study we analyzed the interaction between common free radicals and orthocarborane molecules. For the sake of discussion, we will name our structures as follows. B2000 refers to the structure which has a random mixture of 1000 isolated boron and 400 isolated carbon atoms with 1000 orthocarborane molecules. As all of the structures has 1000 orthocarborane and the ratio of B and

C in free radicals always kept 5 to 1 no of boron hydrogen is enough to refer to a particular

structure. Similarly, BH1000 refers to the structure having 1000 BH and 200 CH radicals with

orthocarborane. At the same way, others can be named as BH_22000 or BH_3500 and so on.

In figure 31, the time evolution of species counts of the simulations is shown for the structures

B500, B1000 and B2000. For B500 and B1000 we observed the ratio of BH radicals were

roughly around 1 to 2 within the first 5 ps of equilibration which is the same as the initial ratio.

However, the ratio for BH_2 and BH_3 were closer to 2 to 3. This was because when the number of

isolated atoms was high, they found each other quickly instead of taking out hydrogen atoms

from the orthocarborane molecules. Almost no CH or CH_2 was found as highly active carbons

either connected with isolated boron or other carbon atoms first or very quickly merged into the

icosahedral structure instead of pulling out hydrogens from them. We observed a significant

number of carbon atoms connected with only one boron (shown as series name CB). We also

found species like carbon atoms connected with only another carbon atom or carbon connected

with another boron and hydrogen and so on. A brief discussion about these species is presented

later. If we look into the figure 31c compared to the initial large number of isolated boron and

carbon atoms the BH, BH_2 free radicals were significantly lower and they attenuated much

quicker than the previous two cases. This supports the fact that when there were too many active

species compare to the size of the simulation cell and a number of orthocarborane molecules, and

those active species got to connect with each other first to create stable or metastable species.

Surprisingly, we observed, som e attenuation in BH_3 which we did not observe before as BH_3

molecule is itself a stable molecule. This was very interesting because we observed for this

simulation most of the BH_3 formed right at the beginning but at that moment there were lot other

isolated boron and carbon atoms also which were very eager to find other species to create
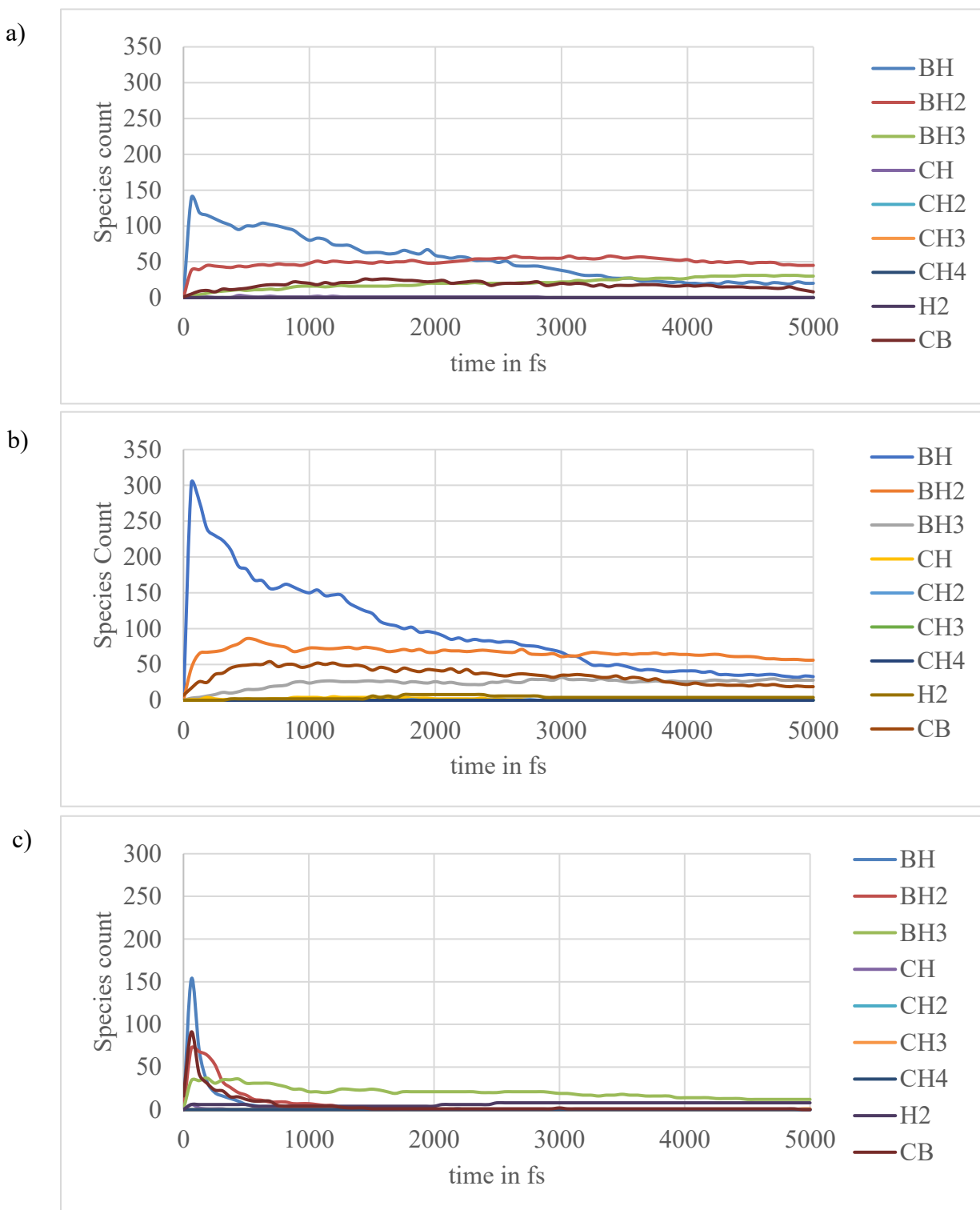
Figure 31. Time evolution of species for orthocarborane with different number of free boron and carbon atoms at 300K: a) B500, b) B1000, c) B2000

bonds. Those were active enough to do the chemical reaction with BH_3 whenever came closer and formed metastable species including B_2H_3 and BCH_3.

Figure 32 shows the time evolution of common species for B2000 structure at 800K (experimentally highest temperature was used over 700K [27]. The key difference between room temperature and the higher temperature was the initial number of BH and BH_2 radicals. They formed in much higher in number for 800K and it was also noticeable that those radical also decayed quickly as they were too many of them. The number of BH_3 after 5 ps was much higher than in room temperature. However, that number steadily increased with time as for higher temperature, the highly vibrating isolated boron atoms were less likely to find three hydrogen
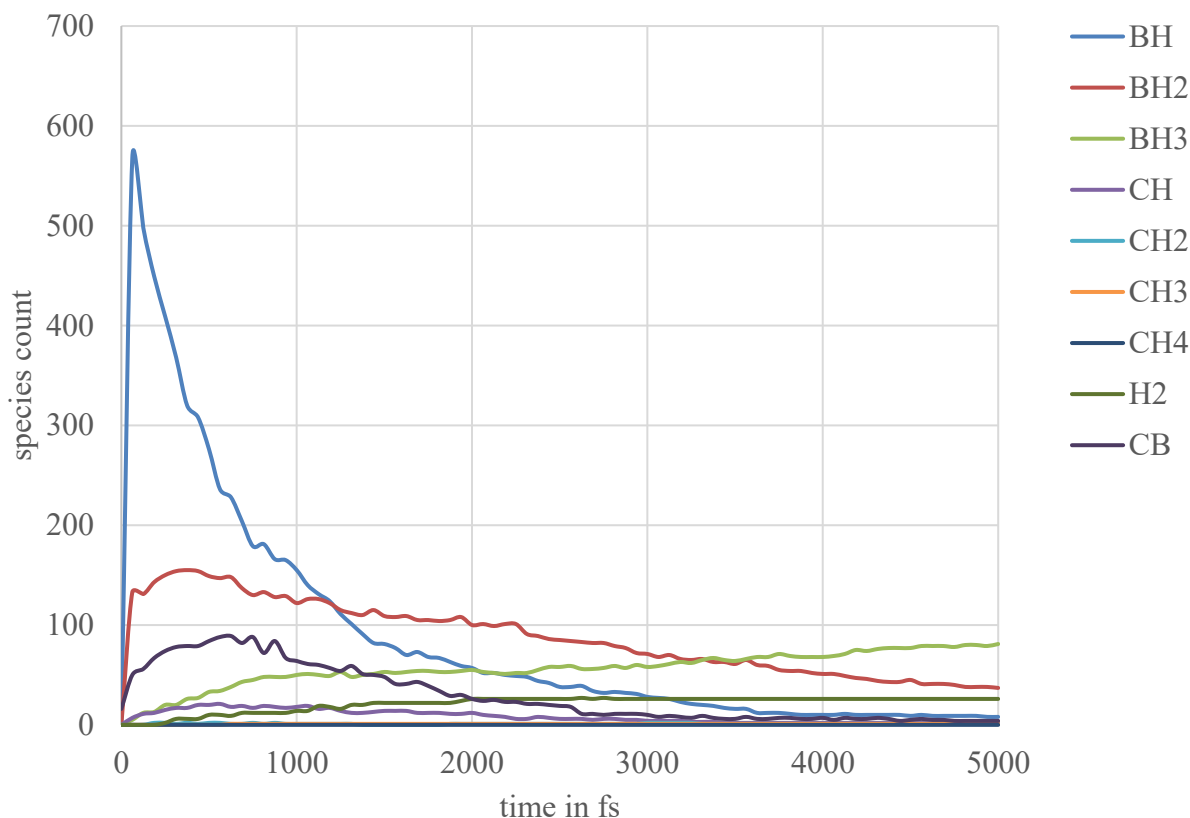
Figure 32. Time evolution of species for orthocarborane with free boron and carbon atoms at 800K for structure B2000

atoms initially. All of the species except showed in the figure 30, H_2 and BH_3 disappear after 25 ps.

We carried out some cluster analysis after equilibrating the structures for 250 ps at different temperature. In figure 33 cluster analysis is shown at 300K for B50, B500 and B2000. At the beginning of the equilibration, there were only clusters of 24 atoms which is obviously the orthocarborane molecules and. All of the figures here we observed the dominant number of clusters are with 24 molecules, but their number drastically decreased with an increasing number of initially added active radicals. For figure 33a the number of the cluster with 24 molecules were just above 900 which refers almost all of the molecules were not affected as there were only a few free B and C initially. And no significant number of bigger clusters were observed. For the figure 33b cluster with 24 molecules were around 500 and we found a considerable number of bigger clusters but still mostly between 22 to 27 molecules. However, for the figure 33c though dominant peaks were around 24 but the number was just above 140. And larger clusters of widely varying sizes were found which indicated aggregation.

In figure 34 the most common 10 species are shown at different times of equilibration at room temperature for structure B1000. These datasets provide a brief detail about the varieties of created species and their time evolution. Orthocarborane molecules were excluded from the histogram plots. Figure 34 shows how drastically the number of B and C declined over time during equilibration at room temperature for structure B1000. Within 0.5 ps almost 75% isolated boron and around 40% carbon declined of their initial numbers. In the course of time, boron produced BH, BH_2, BH_3 mostly. However, as carbon mostly merged into icosahedral species, wide varieties of icosahedral species were created with C_3, like $B_{10}C_3H_{12}$, $B_{11}C_3H_{12}$, $B_{12}C_3H_{12}$, and others. Isolated boron and carbon pulled the hydrogen out from orthocarborane and left

63
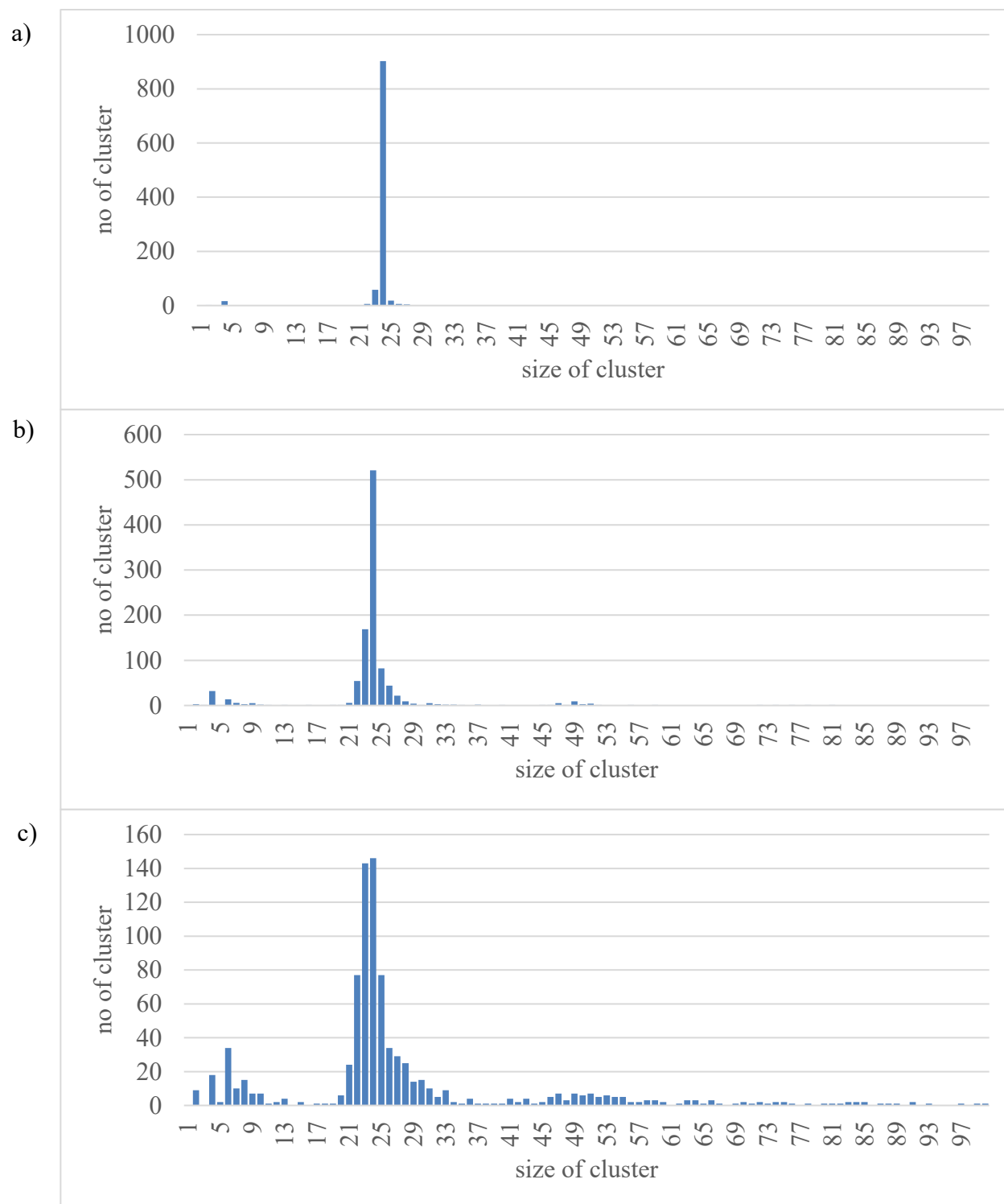
Figure 33. Cluster analysis for orthocarborane with free boron and carbon after equilibration: a) B50, b) B500, c) B2000

mostly $B_{10}C_2H_{11}$ species. Therefore, the number of $B_{10}C_2H_{11}$ increased gradually until there were B, BH, and C were present. A good number of BC species was found, but as they are very active
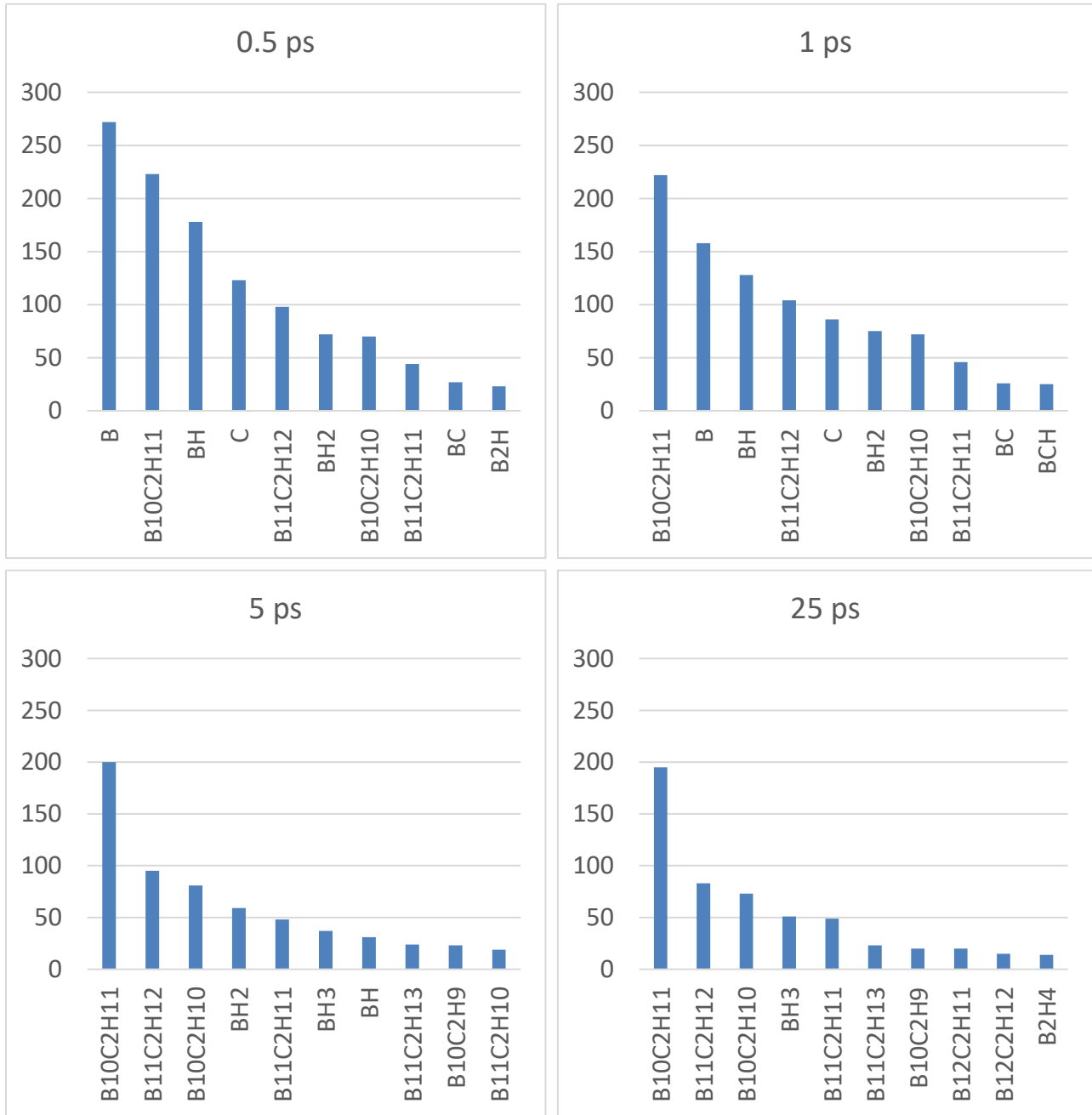
Figure 34. Different species count at different times for structure B1000

65

species as well, they disappeared quickly. A considerable amount of boron also merged in the icosahedral species. That leads to the creation of species with 11 or 12 boron atoms. After 25 ps of equilibration, we observed $B_{11}C_2H_{12}$, $B_{11}C_2H_{11}$, $B_{11}C_2H_{13}$, and $B_{12}C_2H_{12}$ species in top 10 species list.

Figure 35 shows similar data for the structure BH1000. The declination of BH was also quick but not as quick as B for the B1000 structure. Around 65% BH and 40% CH were declined within 0.5 ps for BH1000 structure. Similar to B1000, BH radicals pulled out hydrogens from orthocarborane and became BH_2, BH_3 and more. Therefore, we observe also a high amount of $B_{10}C_2H_{11}$ and $B_{10}C_2H_{11}$. However, some of the BH and CH merged into the icosahedra and produced species like $B_{11}C_2H_{10-12}$, $B_{10}C_3H_{12}$, $B_{11}C_3H_{12,}$ and others. C_3 clusters were not found in abundance as B_{11} or B_{12} clusters as initially, CH was low in number. Metastable species B_2H_2 were high in number at the beginning but they disappeared at the end as they are chemically very active. Some of them turned into less active metastable or stable species including $B_2H_{3,}$ B_2H_4, and B_2H_6. Another notable species BCH_2, which was available within 0.5 ps of equilibration. Formation of BCH_2 is possible in numerous ways: a) B finding a CH_2, b) C finding one BH_2, c) merging of BH and CH radicals. However, BCH_2 itself is metastable, after 25 ps it disappeared completely. For BH1000 structure we found 100 BH_3 after 25 ps, which is exactly double the number for B1000 structure.

For the structure of BH_21000, as shown in figure 36, we observed BH_2 declined at a much slower rate compared to B and BH in the structures B1000 and BH1000 respectively. Less than 45% of BH_2 declined in the first 0.5 ps. Even after 25 ps, almost 10% of BH_2 remained in the final stage of equilibration. This is very much expected as BH_2 is much less active compared to B and BH. Similarly, we found a notable number of CH_2 at the end of equilibration. However,
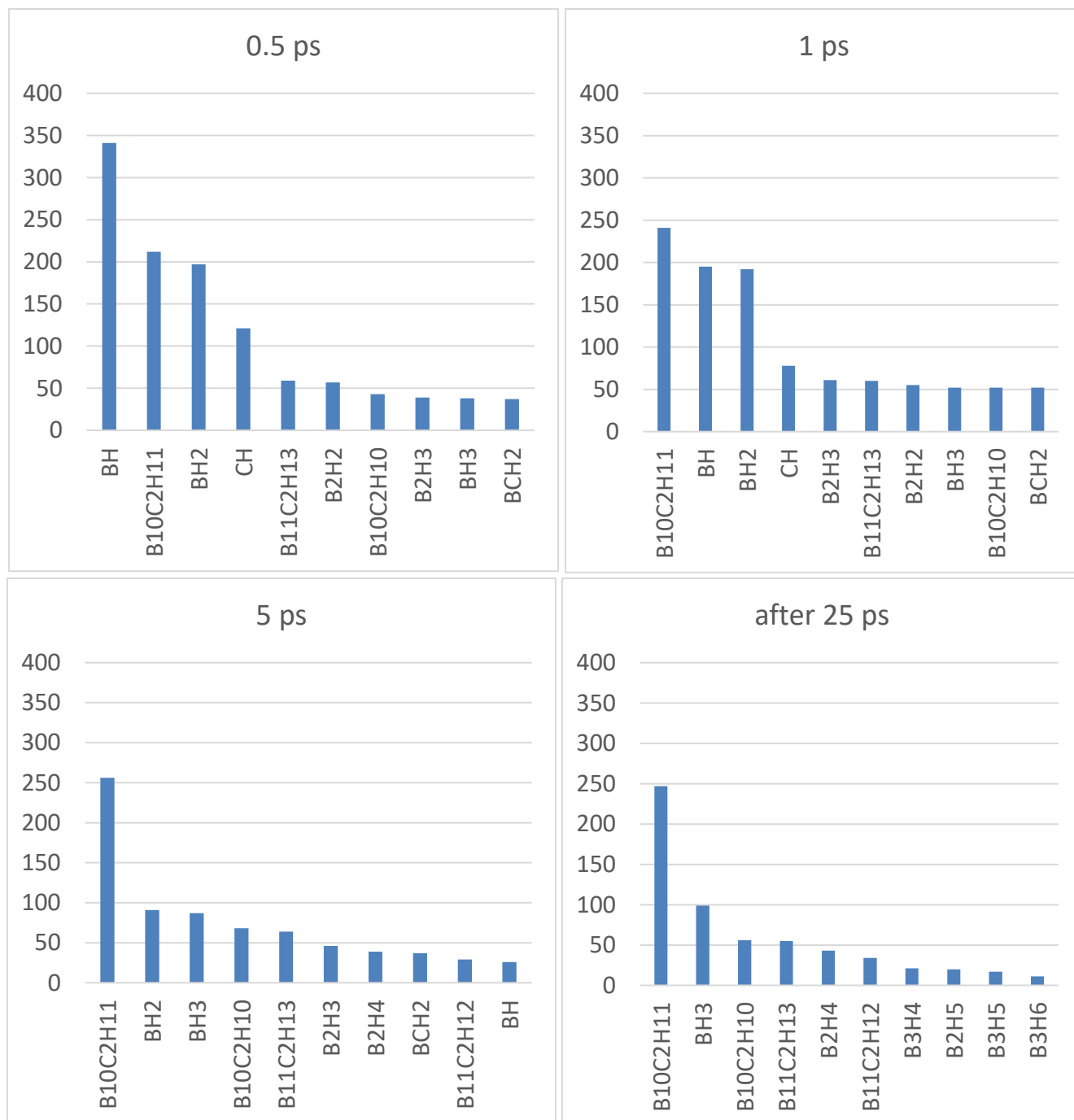
Figure 35. Different species count at different times for structure BH1000

we observed B_2H_4 molecules at every stage of equilibration as shown in the figure 36, which was

formed most likely due to the dimerization of two BH_2. B_2H_4 or diborane tetrahydride is also

known as diborane(4) [98], [99]. Diborane (4) emerged early in the equilibration process and the
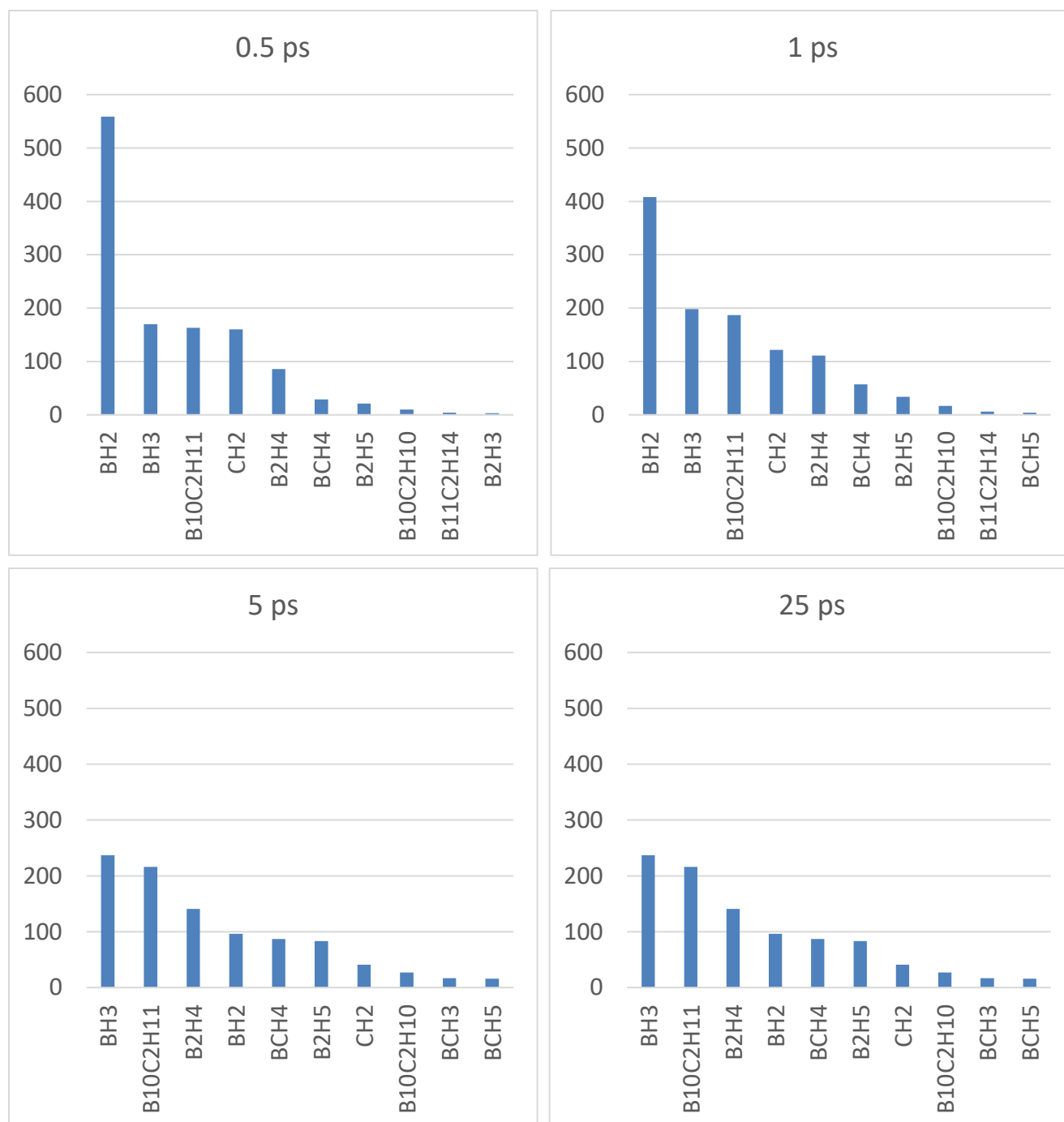
Figure 36. Different species count at different times for structure $BH_2 1000$

gradual increase of the number indicates the stability of the molecule. Similarly, one BH_2 and CH_2 formed BCH_4 by merging together. However, no C_2H_4 was found in whole equilibration process. As the added species initially had higher hydrogen content at the end of equilibration

most of the common species had a higher atomic percentage of hydrogen. Apart from previously described species, there were a lot more of BH_3 compare to B1000 and BH1000. There were also species with higher than 50 at. % hydrogen, like BCH_5, BCH_4, BCH_3, and B_2H_5 after 25 ps. Nevertheless, we found $B_{10}C_2H_{11}$ and even $B_{10}C_2H_{10}$ at end of equilibration which indicates some of the BH_2, and CH_2 radicals were able to pull out hydrogen from the orthocarborane molecules.

In the last part of this systematic studies, we equilibrated 1000 orthocarborane with different numbers of BH_3 and CH_3 radicals. Compared to previously discussed structures obviously, orthocarborane with BH_3 and CH_3 structures have the highest at % of hydrogen. Additionally, the added species are less active (CH_3) and almost inactive (BH_3). Therefore, at room temperature, not much chemical reaction happened for $BH_3$1000 structure, as shown in figure 37. No change observed compare to the initial structure after 0.1 ps. After 0.5 ps, few BH_3 and CH_3 merged together and produced BCH_6. Throughout the equilibration process, these three were the only species found apart from the orthocarborane. The number of BCH_6 increased slowly but steadily. After 25 ps around 65% of initial CH_3 were declined in number. No C_2H_6 was found which was not expected. Most likely there were not enough CH_3 at the beginning and they hardly could find each other to get connected during the equilibration. On the other hand, BH_3 species were in abundance and most likely CH_3 found them and produced BCH_6. At room temperature, CH_3 were not active enough to pull out hydrogen from the orthocarborane. Therefore, the total number of orthocarborane throughout the equilibration process was the same.

Figure 38 depicts how the number of orthocarborane declined in the course of time during equilibration for different structures. As it is mentioned earlier that for BH_3 and CH_3 no. of orthocarborane molecules were remain unchanged which we observe in figure 38. For other
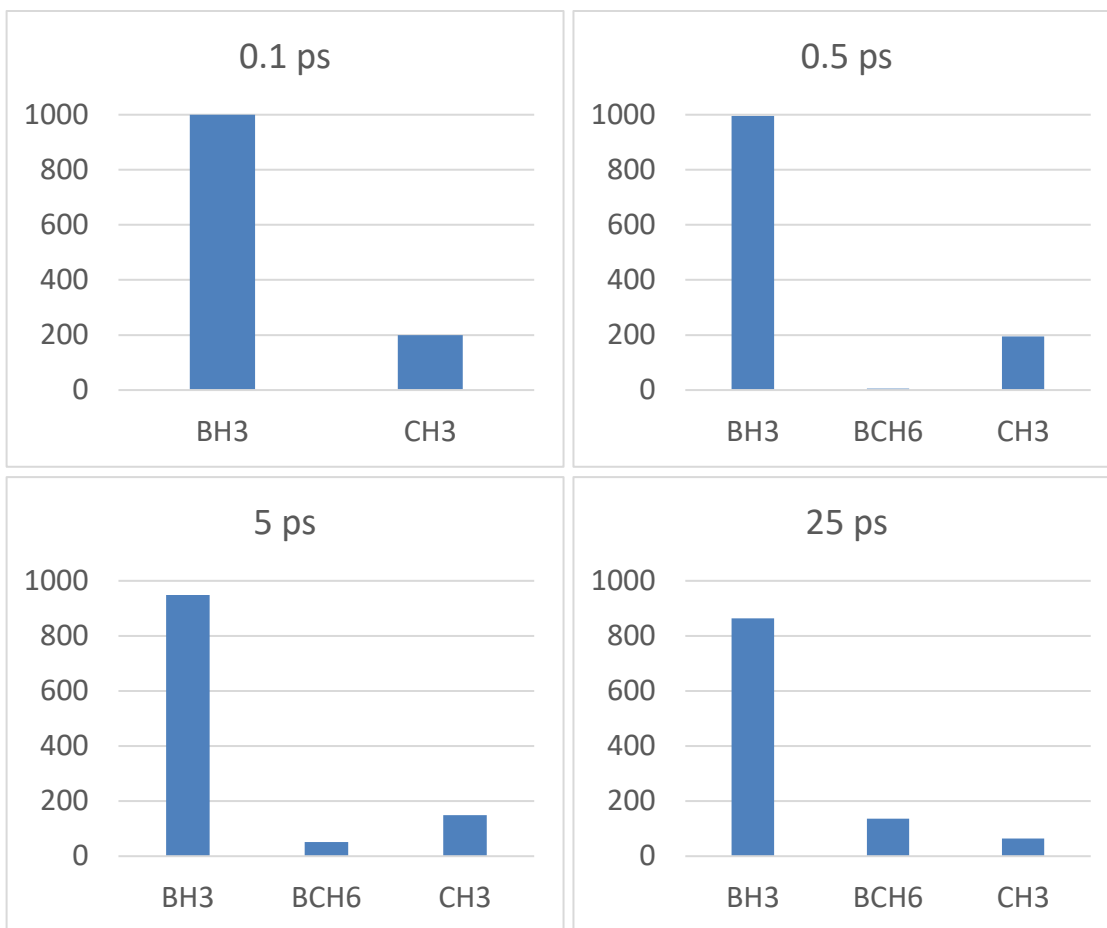
Figure 37. Different species count at different times for structure $BH_3$1000

structures, we observe how the curves changed with respect to the initial species. The more active the species are, the quicker decay occurred in the numbers. These results support our previous analysis and provide a summary of the speed of the chemical reaction in the equilibration processes.

Amorphous Hydrogenated Boron Carbide

In this part of our study, we analyze the impact of the hydrogen content in the densification process at different temperatures in zero pressure. As the atomic percent of

hydrogen attached to the icosahedral structure is inversely proportional to the amount of available active sites, the density would accordingly decrease as the amount of hydrogen is increased.

Initial and final structures of 25% hydrogenated B_{11}C-CBC are shown in figure 39 after equilibration for 12.5 ps at room temperature (300K). At the beginning of the equilibration, obviously, there was no connection between the species as we created the structure with minimum 2.0 A distance between the units. The units have random placement and random 3D orientation. From figure 39b we see after equilibration how the species connected with each other and formed clusters. This was possible due to the availability of the active sites in the icosahedral structure. The active CBC chains created a bond with hydrogen-free boron and
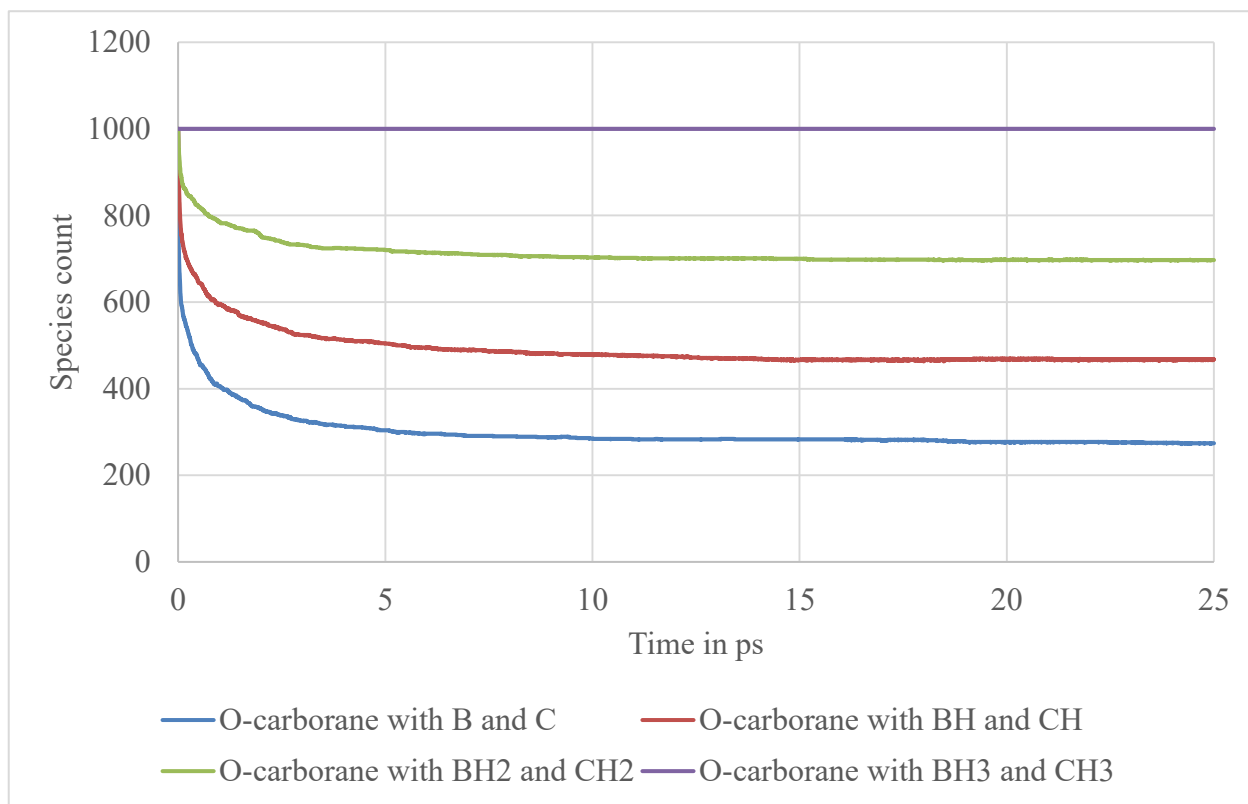
Figure 38. Time evolution of number of orthocarborane with different free radicals
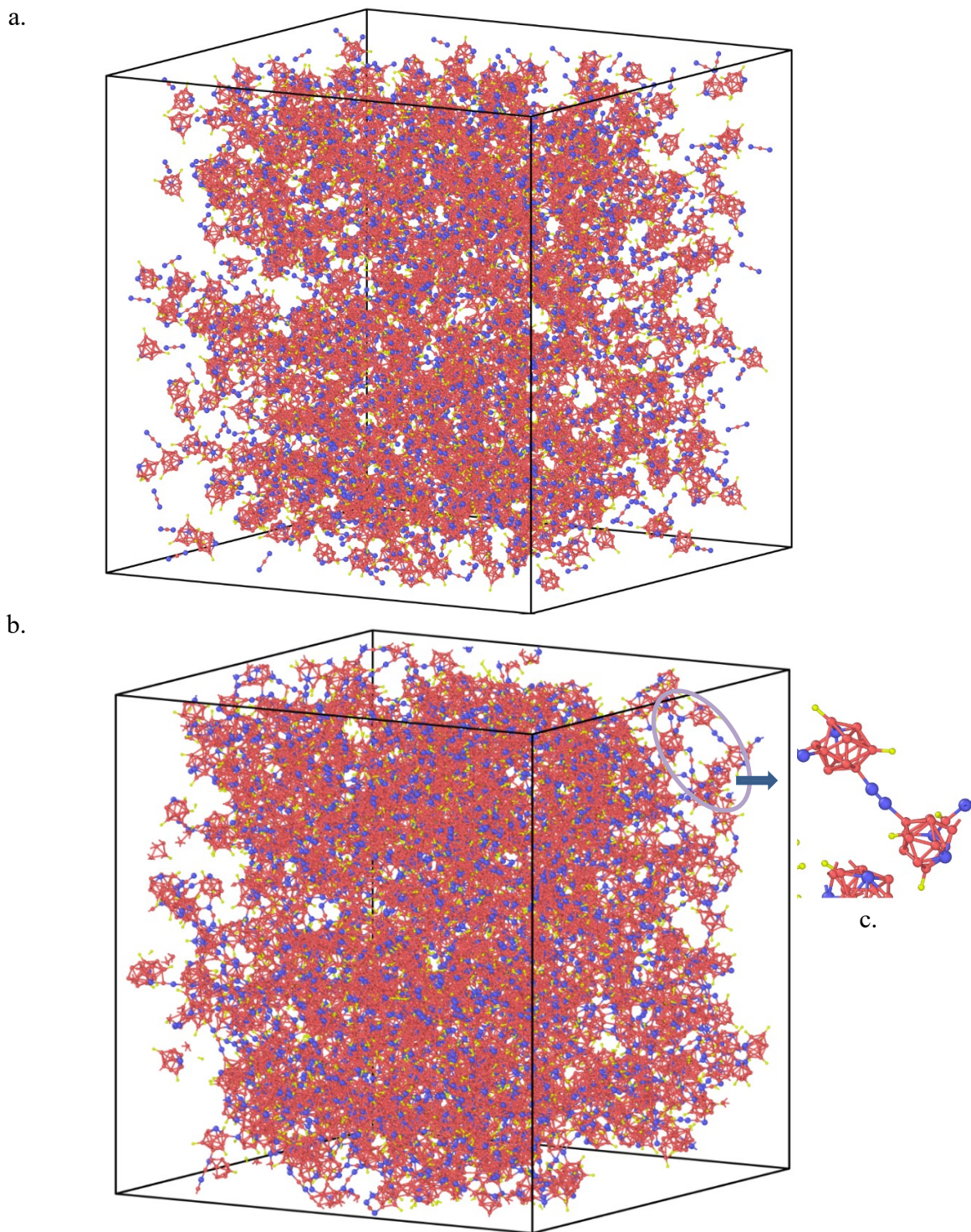
Figure 39. Equilibration of 25% hydrogenated $B_{11}C$-CBC: a) initial structure, b) after 50 ps c) zoomed in view of inter-icosahedral connection via CBC chain.

carbon atoms of the icosahedra. Some of the CBC chains also made bonds between themselves and created longer chains. Similarly, some neighboring icosahedra created bonds between themselves. In figure 39c a zoomed in view is presented that shows an example of how the icosahedral species are connected with each other. While performing species calculation we found only a single species: $B_{12000}C_{3000}H_{3000}$. This indicates that there was no isolated chain or icosahedron in the final structure. For 50% hydrogenated we also obtained the same results while performing species calculation. Figure 40 compares the species for 75% and 100% hydrogenated (addressed as structure C and D respectively) $B_{11}C$-CBC structures. For structure C only a few initial icosahedral species were present after equilibration, whereas for structure B the number is
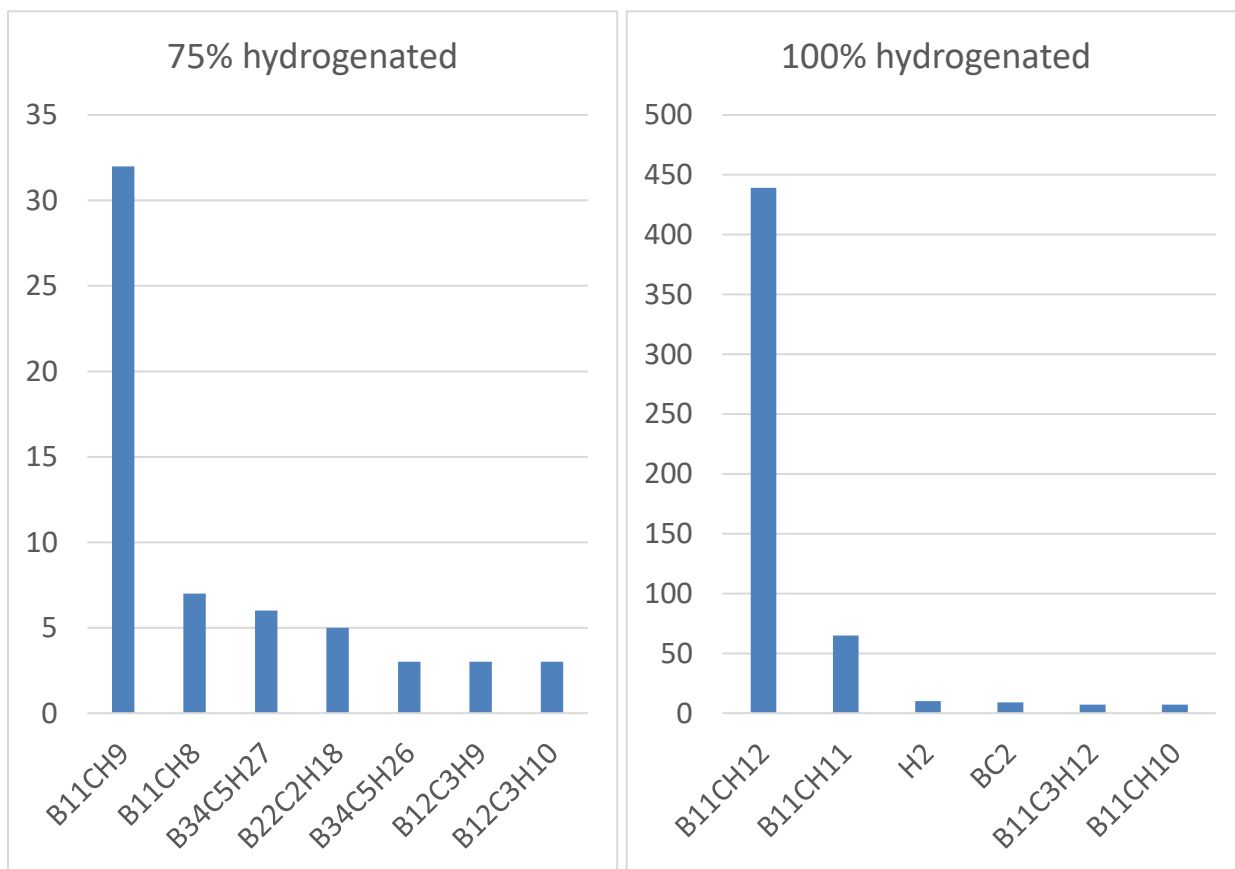
Figure 40. Species calculation for 75% and 100% hydrogenated $B_{11}C$-CBC structures

almost 45% of the initial. Another important aspect of structure A is, we found a cluster of more than 16000 atoms $B_{8169}C_{2148}H_{6087}$. Additionally, there were other clusters with several hundred atoms. However, in structure B, there were mostly small clusters with below 100 atoms and only a few having more than that. No big cluster of over 1000 atoms was found.

In figure 41 the volume changes over time are shown for different hydrogen content at room temperature (300K). We can see when the active sites were abundantly available in the icosahedra structures, the densification would readily proceed, and subsequently a stable volume if the agglomerates are obtained. On the other hand, when all (100%) icosahedral structures are hydrogenated, the densification fails to occur and the structures continue to expand even at a lower temperature.
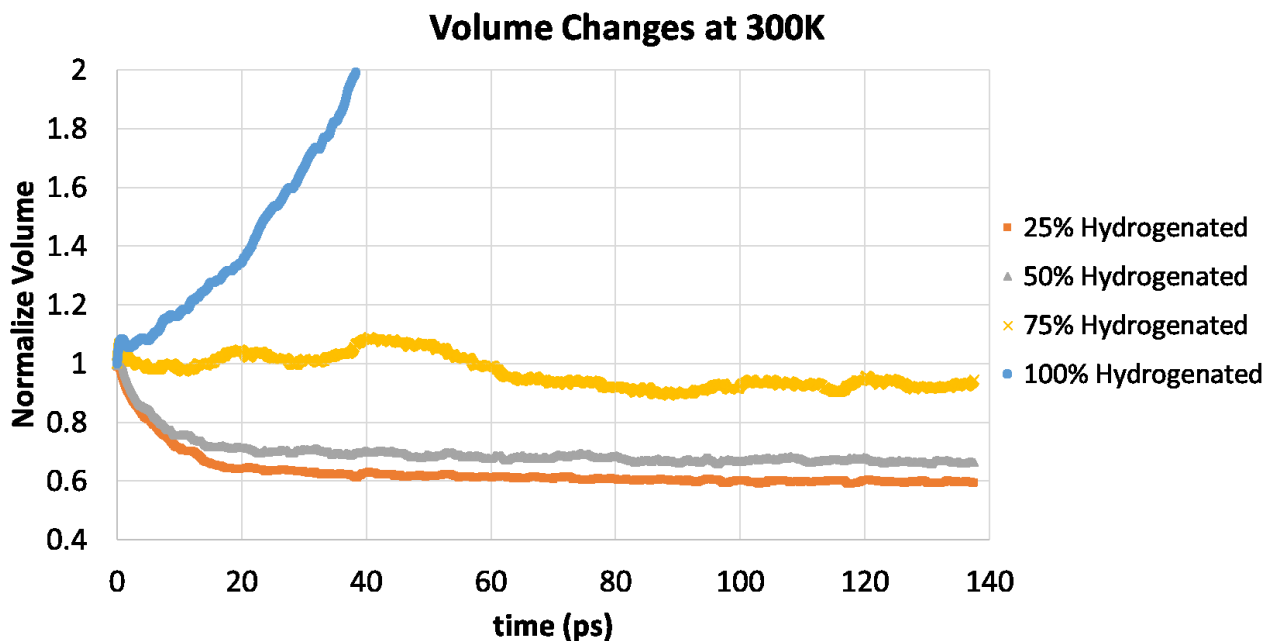
Figure 41. Volume changes with time for structures with different hydrogen content

CONCLUSION

We have successfully modeled the argon bombardment process using a reactive force field (ReaxFF) molecular dynamics simulation. By varying the energy of argon atoms, we systematically determined the amount of hydrogen gas and various types of gaseous species produced. The time evolution of PDF analysis allowed us to monitor the decomposition of orthocarborane molecules as a result of the bombardment. In addition, we have successfully identified the free radicals formed that greatly contribute to the densification process. Using bond order calculation, we tracked every types of species for any timesteps. Hence, the interactions between common free radicals and orthocarborane have been studied extensively. The modeling provides a better understanding of the impact of the hydrogen content toward the densification process which would presumably affect the mechanical properties of the thin film. As the argon energy effectively controls the amount of hydrogen gas formation and thus the densification process, we can, therefore, fine-tune the final hydrogen content within the thin film through a careful design in the initial power input. Thus, our work should provide importance guidance for synthesizing better quality films.

REFERENCES

[1]   F. Thevenot, "Boron carbide—a comprehensive review," *J. Eur. Ceram. Soc.*, vol. 6, no. 4, pp. 205–225, 1990.

[2]   A. N. Caruso *et al.*, "The all boron carbide diode neutron detector: Comparison with theory," *Mater. Sci. Eng. B*, vol. 135, no. 2, pp. 129–133, 2006.

[3]   D. K. Bose, K. U. Nair, and C. K. Gupta, "Production of high purity boron carbide," *High Temp. Mater. Process.*, vol. 7, no. 2–3, pp. 133–140, 1986.

[4]   L. M. Han, Y. Xu, J. Z. Xie, M. S. Zhou, and S. Chooi, "Use of boron carbide as an etch-stop and barrier layer for copper dual damascene metallization." Google Patents, 05-Mar-2002.

[5]   A. N. Caruso, "The physics of solid-state neutron detector materials and geometries," *J. Phys. Condens. Matter*, vol. 22, no. 44, p. 443201, 2010.

[6]   R. A. M. Keski-Kuha, G. M. Blumenstock, C. M. Fleetwood, and D.-R. Schmitt, "Effects of space exposure on ion-beam-deposited silicon-carbide and boron-carbide coatings," *Appl. Opt.*, vol. 37, no. 34, pp. 8038–8042, 1998.

[7]   H. Hu and J. Kong, "Improved thermal performance of diamond-copper composites with boron carbide coating," *J. Mater. Eng. Perform.*, vol. 23, no. 2, pp. 651–657, 2014.

[8]   Y. Chen, Y.-W. Chung, and S.-Y. Li, "Boron carbide and boron carbonitride thin films as protective coatings in ultra-high density hard disk drives," *Surf. Coatings Technol.*, vol. 200, no. 12–13, pp. 4072–4077, 2006.

[9]   S. Veprek, "Large-area boron-carbide protective coatings for controlled thermonuclear research prepared by insitu plasma CVD," *Plasma Chem. plasma Process.*, vol. 12, no. 3, pp. 219–235, 1992.

[10]   A. K. Suri, C. Subramanian, J. K. Sonber, and T. S. R. C. Murthy, "Synthesis and consolidation of boron carbide: a review," *Int. Mater. Rev.*, vol. 55, no. 1, pp. 4–40, 2010.

[11]   S. Hayun, S. Kalabukhov, V. Ezersky, M. P. Dariel, and N. Frage, "Microstructural characterization of spark plasma sintered boron carbide ceramics," *Ceram. Int.*, vol. 36, no. 2, pp. 451–457, 2010.

[12]   J. E. Zorzi, C. A. Perottoni, and J. A. H. Da Jornada, "Hardness and wear resistance of B4C ceramics prepared with several additives," *Mater. Lett.*, vol. 59, no. 23, pp. 2932–2935, 2005.

[13]   M. W. Chen, J. W. McCauley, J. C. LaSalvia, and K. J. Hemker, "Microstructural

characterization of commercial hot-pressed boron carbide ceramics," *J. Am. Ceram. Soc.*, vol. 88, no. 7, pp. 1935–1942, 2005.

[14] A. K. Bandyopadhyay, F. Beuneu, L. Zuppiroli, and M. Beauvy, "The role of free carbon in the transport and magnetic properties of boron carbide," *J. Phys. Chem. Solids*, vol. 45, no. 2, pp. 207–214, 1984.

[15] C. Wood and D. Emin, "Conduction mechanism in boron carbide," *Phys. Rev. B*, vol. 29, no. 8, p. 4582, 1984.

[16] S. Lee, J. Mazurowski, G. Ramseyer, and P. A. Dowben, "Characterization of boron carbide thin films fabricated by plasma enhanced chemical vapor deposition from boranes," *J. Appl. Phys.*, vol. 72, no. 10, pp. 4925–4933, 1992.

[17] G. M. Blumenstock and R. A. M. Keski-Kuha, "Ion-beam-deposited boron carbide coatings for the extreme ultraviolet," *Appl. Opt.*, vol. 33, no. 25, pp. 5962–5963, 1994.

[18] A. O. Sezer and J. I. Brand, "Chemical vapor deposition of boron carbide," *Mater. Sci. Eng. B*, vol. 79, no. 3, pp. 191–202, 2001.

[19] H. Suematsu *et al.*, "Preparation of polycrystalline boron carbide thin films at room temperature by pulsed ion-beam evaporation," *Appl. Phys. Lett.*, vol. 80, no. 7, pp. 1153–1155, 2002.

[20] S. Sasaki *et al.*, "Thermoelectric properties of boron-carbide thin film and thin film based thermoelectric device fabricated by intense-pulsed ion beam evaporation," *Sci. Technol. Adv. Mater.*, vol. 6, no. 2, p. 181, 2005.

[21] R. B. Billa, T. Hofmann, M. Schubert, and B. W. Robertson, "Annealing effects on the optical properties of semiconducting boron carbide," *J. Appl. Phys.*, vol. 106, no. 3, p. 33515, 2009.

[22] V. K. Alimov *et al.*, "Characterization of aB/C: H films deposited from different boron containing precursors," *J. Nucl. Mater.*, vol. 196, pp. 670–675, 1992.

[23] V. M. Sharapov *et al.*, "Boronization of Russian tokamaks from carborane precursors," *J. Nucl. Mater.*, vol. 220, pp. 730–735, 1995.

[24] D. Zhang, D. N. McIlroy, W. L. O'Brien, and G. De Stasio, "The chemical and morphological properties of boron–carbon alloys grown by plasma-enhanced chemical vapour deposition," *J. Mater. Sci.*, vol. 33, no. 20, pp. 4911–4915, 1998.

[25] A. N. Caruso, R. B. Billa, S. Balaz, J. I. Brand, and P. A. Dowben, "The heteroisomeric diode," *J. Phys. Condens. Matter*, vol. 16, no. 10, p. L139, 2004.

[26] D. L. Schulz *et al.*, "Characterization of a-B5C: H prepared by PECVD of orthocarborane: Results of preliminary FTIR and nuclear reaction analysis studies," *J. Non. Cryst. Solids*, vol. 354, no. 19–25, pp. 2369–2371, 2008.

[27] B. J. Nordell *et al.*, "The influence of hydrogen on the chemical, mechanical, optical/electronic, and electrical transport properties of amorphous hydrogenated boron carbide," *J. Appl. Phys.*, vol. 118, no. 3, p. 35703, 2015.

[28] R. Lazzari, N. Vast, J. M. Besson, S. Baroni, and A. Dal Corso, "Atomic structure and vibrational properties of icosahedral B 4 C boron carbide," *Phys. Rev. Lett.*, vol. 83, no. 16, p. 3230, 1999.

[29] Z. Gamba and B. M. Powell, "The condensed phases of carboranes," *J. Chem. Phys.*, vol. 105, no. 6, pp. 2436–2440, 1996.

[30] R. H. Baughman, "NMR, calorimetric, and diffraction study of molecular motion in crystalline carboranes," *J. Chem. Phys.*, vol. 53, no. 10, pp. 3781–3789, 1970.

[31] L. A. Leites, "Vibrational spectroscopy of carboranes and parent boranes and its capabilities in carborane chemistry," *Chem. Rev.*, vol. 92, no. 2, pp. 279–323, 1992.

[32] D. Byun, B. R. Spady, N. J. Ianno, and P. A. Dowben, "Comparison of different chemical vapor deposition methodologies for the fabrication of heterojunction boron-carbide diodes," *Nanostructured Mater.*, vol. 5, no. 4, pp. 465–471, 1995.

[33] S. Adenwalla, P. Welsch, A. Harken, J. I. Brand, A. Sezer, and B. W. Robertson, "Boron carbide/n-silicon carbide heterojunction diodes," *Appl. Phys. Lett.*, vol. 79, no. 26, pp. 4357–4359, 2001.

[34] K. Park *et al.*, "Electronic structure and vibrational spectra of C 2 B 10-based clusters and films," *Phys. Rev. B*, vol. 73, no. 3, p. 35109, 2006.

[35] P. Lunca-Popa *et al.*, "Evidence for multiple polytypes of semiconducting boron carbide (C2B10) from electronic structure," *J. Phys. D. Appl. Phys.*, vol. 38, no. 8, p. 1248, 2005.

[36] E. Rühl *et al.*, "Photofragmentation of the closo-Carboranes Part II: VUV Assisted Dehydrogenation in the closo-Carboranes and Semiconducting B10C2H x Films," *J. Phys. Chem. A*, vol. 114, no. 27, pp. 7284–7291, 2010.

[37] D. Feng *et al.*, "Photofragmentation of closo-Carboranes Part 1: Energetics of Decomposition," *J. Phys. Chem. A*, vol. 112, no. 15, pp. 3311–3318, 2008.

[38] O. I. Buzhinskij *et al.*, "Plasma deposition of boron films with high growth rate and efficiency using carborane," *J. Nucl. Mater.*, vol. 313, pp. 214–218, 2003.

[39] B. J. Alder and T. E. Wainwright, "Phase transition for a hard sphere system," *J. Chem. Phys.*, vol. 27, no. 5, pp. 1208–1209, 1957.

[40] A. van Duin, *ReaxFF User Manual*, no. December. 2002.

[41] H. C. Andersen, "Molecular dynamics simulations at constant pressure and/or temperature," *J. Chem. Phys.*, vol. 72, no. 4, pp. 2384–2393, 1980.

[42] T. Schlick, *Molecular modeling and simulation: an interdisciplinary guide: an interdisciplinary guide*, vol. 21. Springer Science & Business Media, 2010.

[43] S. Plimpton, "Fast parallel algorithms for short-range molecular dynamics," *J. Comput. Phys.*, vol. 117, no. 1, pp. 1–19, 1995.

[44] W. Bao and Q. Du, *Multiscale Modeling and Analysis for Materials Simulation*, vol. 22. World Scientific, 2012.

[45] L. Sandoval and H. M. Urbassek, "Finite-Size Effects in Fe-Nanowire Solid− Solid Phase Transitions: A Molecular Dynamics Approach," *Nano Lett.*, vol. 9, no. 6, pp. 2290–2294, 2009.

[46] Z. X. Wen, J. P. Wang, Y. W. Wu, K. J. Zhou, and Z. F. Yue, "Atomistic simulation analysis of the effects of void interaction on void growth and coalescence in a metallic system," *Curr. Appl. Phys.*, vol. 18, no. 6, pp. 744–751, 2018.

[47] N.-L. Li, W.-P. Wu, and K. Nie, "Molecular dynamics study on the evolution of interfacial dislocation network and mechanical properties of Ni-based single crystal superalloys," *Phys. Lett. A*, vol. 382, no. 20, pp. 1361–1367, 2018.

[48] K. T. Ramesh, "High rates and impact experiments," *Springer Handb. Exp. solid Mech.*, pp. 929–960, 2008.

[49] A. I. Duff, M. W. Finnis, P. Maugis, B. J. Thijsse, and M. H. F. Sluiter, "MEAMfit: A reference-free modified embedded atom method (RF-MEAM) energy and force-fitting code," *Comput. Phys. Commun.*, vol. 196, pp. 439–445, 2015.

[50] P. Brommer, A. Kiselev, D. Schopf, P. Beck, J. Roth, and H.-R. Trebin, "Classical interaction potentials for diverse materials from ab initio data: a review of potfit," *Model. Simul. Mater. Sci. Eng.*, vol. 23, no. 7, p. 74002, 2015.

[51] P. Brommer and F. Gähler, "Potfit: effective potentials from ab initio data," *Model. Simul. Mater. Sci. Eng.*, vol. 15, no. 3, p. 295, 2007.

[52] S. Plimpton, P. Crozier, and A. Thompson, "LAMMPS-large-scale atomic/molecular massively parallel simulator," *Sandia Natl. Lab.*, vol. 18, p. 43, 2007.

[53] J. Stadler, R. Mikulla, and H.-R. Trebin, "IMD: a software package for molecular dynamics studies on parallel computers," *Int. J. Mod. Phys. C*, vol. 8, no. 05, pp. 1131–1140, 1997.

[54] H. Watanabe, M. Suzuki, and N. Ito, "Huge-scale molecular dynamics simulation of multibubble nuclei," *Comput. Phys. Commun.*, vol. 184, no. 12, pp. 2775–2784, 2013.

[55] H. Watanabe, M. Suzuki, and N. Ito, "Efficient implementations of molecular dynamics simulations for lennard-jones systems," *Prog. Theor. Phys.*, vol. 126, no. 2, pp. 203–235, 2011.

[56]   "MDSPASS." [Online]. Available: http://www.cmsm.iis.u-tokyo.ac.jp/software_en.html.

[57]   A. M. Iskandarov, S. V Dmitriev, and Y. Umeno, "Temperature effect on ideal shear strength of Al and Cu," *Phys. Rev. B*, vol. 84, no. 22, p. 224118, 2011.

[58]   J. D. Gale, "GULP: A computer program for the symmetry-adapted simulation of solids," *J. Chem. Soc. Faraday Trans.*, vol. 93, no. 4, pp. 629–637, 1997.

[59]   D. A. Case *et al.*, "The Amber biomolecular simulation programs," *J. Comput. Chem.*, vol. 26, no. 16, pp. 1668–1688, 2005.

[60]   B. R. Brooks *et al.*, "CHARMM: the biomolecular simulation program," *J. Comput. Chem.*, vol. 30, no. 10, pp. 1545–1614, 2009.

[61]   J. C. Phillips *et al.*, "Scalable molecular dynamics with NAMD," *J. Comput. Chem.*, vol. 26, no. 16, pp. 1781–1802, 2005.

[62]   L. Martínez, R. Andrade, E. G. Birgin, and J. M. Martínez, "PACKMOL: a package for building initial configurations for molecular dynamics simulations," *J. Comput. Chem.*, vol. 30, no. 13, pp. 2157–2164, 2009.

[63]   T. P. Senftle *et al.*, "The ReaxFF reactive force-field: development, applications and future directions," *npj Comput. Mater.*, vol. 2, p. 15011, 2016.

[64]   R. G. Parr, "Density functional theory of atoms and molecules," in *Horizons of Quantum Chemistry*, Springer, 1980, pp. 5–15.

[65]   E. Runge and E. K. U. Gross, "Density-functional theory for time-dependent systems," *Phys. Rev. Lett.*, vol. 52, no. 12, p. 997, 1984.

[66]   R. Car and M. Parrinello, "Unified approach for molecular dynamics and density-functional theory," *Phys. Rev. Lett.*, vol. 55, no. 22, p. 2471, 1985.

[67]   G. Kresse and J. Furthmüller, "Software VASP, vienna (1999)," *Phys. Rev. B*, vol. 54, no. 11, p. 169, 1996.

[68]   "Gaussian.com | Expanding the limits of computational chemistry." .

[69]   P. Blaha, K. Schwarz, G. K. H. Madsen, D. Kvasnicka, and J. Luitz, "wien2k," *An Augment. Pl. wave+ local orbitals Progr. Calc. Cryst. Prop.*, 2001.

[70]   J. Hutter *et al.*, "CPMD MPI für Festkörperforschung, and IBM Zurich Research Laboratory." Stuttgart, 1995.

[71]   X. Gonze *et al.*, "First-principles computation of material properties: the ABINIT software project," *Comput. Mater. Sci.*, vol. 25, no. 3, pp. 478–492, 2002.

[72]   J. M. Soler *et al.*, "The SIESTA method for ab initio order-N materials simulation," *J. Phys. Condens. Matter*, vol. 14, no. 11, p. 2745, 2002.

[73]   P. Giannozzi *et al.*, "QUANTUM ESPRESSO: a modular and open-source software project for quantum simulations of materials," *J. Phys. Condens. matter*, vol. 21, no. 39, p. 395502, 2009.

[74]   G. Kresse and D. Joubert, "From ultrasoft pseudopotentials to the projector augmented-wave method," *Phys. Rev. B*, vol. 59, no. 3, p. 1758, 1999.

[75]   G. Kresse and J. Furthmüller, "Efficient iterative schemes for ab initio total-energy calculations using a plane-wave basis set," *Phys. Rev. B*, vol. 54, no. 16, p. 11169, 1996.

[76]   G. Kresse and J. Furthmüller, "Efficiency of ab-initio total energy calculations for metals and semiconductors using a plane-wave basis set," *Comput. Mater. Sci.*, vol. 6, no. 1, pp. 15–50, 1996.

[77]   H. J. Monkhorst and J. D. Pack, "Special points for Brillouin-zone integrations," *Phys. Rev. B*, vol. 13, no. 12, p. 5188, 1976.

[78]   "minimize command — LAMMPS documentation." [Online]. Available: https://lammps.sandia.gov/doc/minimize.html. [Accessed: 26-Jul-2019].

[79]   A. C. F. Wu, M. A. Lieberman, and J. P. Verboncoeur, "A method for computing ion energy distributions for multifrequency capacitive discharges." AIP, 2007.

[80]   V. Georgieva, A. Bogaerts, and R. Gijbels, "Numerical investigation of ion-energy-distribution functions in single and dual frequency capacitively coupled plasma reactors," *Phys. Rev. E*, vol. 69, no. 2, p. 26406, 2004.

[81]   B. D. Jensen, A. Bandyopadhyay, K. E. Wise, and G. M. Odegard, "Parametric study of ReaxFF simulation parameters for molecular dynamics modeling of reactive carbon gases," *J. Chem. Theory Comput.*, vol. 8, no. 9, pp. 3003–3008, 2012.

[82]   J. Braddock-Wilking, S.-H. Lin, and B. J. Feldman, "13 C NMR spectroscopy of amorphous hydrogenated carbon and amorphous hydrogenated boron carbide," *MRS Online Proc. Libr. Arch.*, vol. 555, 1998.

[83]   S.-H. Lin and B. J. Feldman, "Boron carbide icosahedra and the 1280 cm− 1 line in amorphous hydrogenated boron carbide," *Solid State Commun.*, vol. 107, no. 5, pp. 239–242, 1998.

[84]   B. J. Nordell *et al.*, "Tuning the properties of a complex disordered material: Full factorial investigation of PECVD-grown amorphous hydrogenated boron carbide," *Mater. Chem. Phys.*, vol. 173, pp. 268–284, 2016.

[85]   M. M. Paquette, W. Li, M. S. Driver, S. Karki, A. N. Caruso, and N. A. Oyler, "The local physical structure of amorphous hydrogenated boron carbide: insights from magic angle spinning solid-state NMR spectroscopy," *J. Phys. Condens. Matter*, vol. 23, no. 43, p. 435002, 2011.

[86]   Q. An and W. A. Goddard III, "Atomistic origin of brittle failure of boron carbide from large-scale reactive dynamics simulations: suggestions toward improved ductility," *Phys. Rev. Lett.*, vol. 115, no. 10, p. 105501, 2015.

[87]   A. C. T. Van Duin, S. Dasgupta, F. Lorant, and W. A. Goddard, "ReaxFF: a reactive force field for hydrocarbons," *J. Phys. Chem. A*, vol. 105, no. 41, pp. 9396–9409, 2001.

[88]   K. Chenoweth, A. C. T. Van Duin, and W. A. Goddard, "ReaxFF reactive force field for molecular dynamics simulations of hydrocarbon oxidation," *J. Phys. Chem. A*, vol. 112, no. 5, pp. 1040–1053, 2008.

[89]   G. R. Desiraju and G. W. Parshall, "Crystal engineering: the design of organic solids," *Mater. Sci. Monogr.*, vol. 54, 1989.

[90]   Y. L. Slovokhotov, I. S. Neretin, and J. A. K. Howard, "Symmetry of van der Waals molecular shape and melting points of organic compounds," *New J. Chem.*, vol. 28, no. 8, pp. 967–979, 2004.

[91]   A. Annen, M. Saß, R. Beckmann, A. Von Keudell, and W. Jacob, "Structure of plasma-deposited amorphous hydrogenated boron-carbon thin films," *Thin Solid Films*, vol. 312, no. 1–2, pp. 147–155, 1998.

[92]   K. Kawaguchi, "Fourier transform infrared spectroscopy of the BH3 v3 band," *J. Chem. Phys.*, vol. 96, no. 5, pp. 3411–3415, 1992.

[93]   M. Hall, E. Frank, G. Holmes, B. Pfahringer, P. Reutemann, and I. H. Witten, "The WEKA data mining software: an update," *ACM SIGKDD Explor. Newsl.*, vol. 11, no. 1, pp. 10–18, 2009.

[94]   E. Frank *et al.*, "Weka-a machine learning workbench for data mining," in *Data mining and knowledge discovery handbook*, Springer, 2009, pp. 1269–1277.

[95]   I. Russell and Z. Markov, "An introduction to the Weka data mining system," in *Proceedings of the 2017 ACM SIGCSE Technical Symposium on Computer Science Education*, 2017, p. 742.

[96]   I. H. Witten, E. Frank, M. A. Hall, and C. J. Pal, *Data Mining: Practical machine learning tools and techniques*. Morgan Kaufmann, 2016.

[97]   E. Frank, M. Hall, L. Trigg, G. Holmes, and I. H. Witten, "Data mining in bioinformatics using Weka," *Bioinformatics*, vol. 20, no. 15, pp. 2479–2481, 2004.

[98]   M. A. Vincent and H. F. Schaefer III, "Diborane (4)(B2H4): the boron hydride analog of ethylene," *J. Am. Chem. Soc.*, vol. 103, no. 19, pp. 5677–5680, 1981.

[99]   L. A. Curtiss and J. A. Pople, "Theoretical study of B2H+ 4 and B2H4," *J. Chem. Phys.*, vol. 90, no. 8, pp. 4314–4319, 1989.

APPENDIX

LAMMPS Input Scripts

Structural Minimization Scripts

```
# REAX potential for HCB system

units           real

atom_style        charge

read_data         data.BCH

# ---------- Calling the potential file-------------------------------

pair_style        reax/c lmp_control

pair_coeff        * * ffield.reax.hcb B CH

#----------------------------------------------------------------------

mass            1 10.811

mass            2 1.008

#---------------------Thermo and loop -------------------------------------

thermo          10

thermo_style      custom step temp pe etotal press vol pxx pyy pzz lx ly lz xy xz yz

neighbor          0.3 bin

neigh_modify      every 1 delay 0 check no

restart          10000 restart.*.dens17

fix             3 all qeq/reax 1 0.0 10.0 1e-6 param_bch.qeq

timestep          0.05

dump            1 all atom 10 dump_structural_minimization.dat

minimize          0.0 1.0e-8 5000 100000
```

NVT Simulation Scripts

```
#simulation NVT
```

```
units  real

boundary   p p p

atom_style  charge

read_data   data.BCH

########################################################hybrid potentials

pair_style hybrid reax/c lmp_control lj/cut 11.0

pair_coeff  * * reax/c ffield.reax.hcb B C H NULL

##lj

pair_coeff  1 4 lj/cut 0.150885 3.4265

pair_coeff  2 4 lj/cut 0.115303 3.385

pair_coeff  3 4 lj/cut 0.13283 3.054

pair_coeff  4 4 lj/cut 0.23983 3.4

#mass

mass 1 10.811

mass 2 12.0107

mass 3 1.00794

mass 4 39.948

##############################################################################

velocity  all create 2.0 893267 rot yes dist gaussian

neighbor  0.3 bin

neigh_modify    every 1 delay 0 check yes

restart 10000 restart.*.dens17

#----------------------Thermo and run --------------------------------------

thermo   100

thermo_style custom step temp pe etotal press vol pxx pyy pzz lx ly lz xy xz yz

dump          1 all custom 100 dump_NVT_600_eV.reax.amorphous_b4cH id type q x y z

fix           1 all qeq/reax 1 0.0 10.0 1e-6 param_bch.qeq

fix           4 all reax/c/species 1 1 10 species_600_eV.out element B C H Ar
```

fix   2 all nvt temp 300 300 100.0

timestep   0.25

run   100000

unfix 3

undump 1

##################################### SIMULATION DONE

print "All done"

NPT Simulation Scripts

#simulation NPT

units real

boundary   p p p

atom_style charge

read_data   data.BCH

###hybrid potentials

pair_style hybrid reax/c lmp_control lj/cut 11.0

pair_coeff * * reax/c ffield.reax.hcb B C H NULL

##lj

pair_coeff 1 4 lj/cut 0.150885 3.4265

pair_coeff 2 4 lj/cut 0.115303 3.385

pair_coeff 3 4 lj/cut 0.13283 3.054

pair_coeff 4 4 lj/cut 0.23983 3.4

#mass

mass 1 10.811

mass 2 12.0107

mass 3 1.00794

mass 4 39.948

##

velocity all create 2.0 893267 rot yes dist gaussian

```
neighbor  0.3 bin

neigh_modify    every 1 delay 0 check yes

restart 10000 restart.*.dens17

#----------------------Thermo and run -------------------------------------------

thermo   100

thermo_style custom step temp pe etotal press vol pxx pyy pzz lx ly lz xy xz yz

dump        1 all custom 100 dump_NVT_600_eV.reax.amorphous_b4cH id type q x y z

fix         1 all qeq/reax 1 0.0 10.0 1e-6 param_bch.qeq

fix         2 all reax/c/species 1 1 10 species_600_eV.out element B C H Ar

fix         3 all npt temp 300.0 300.0 100.0 iso 0.0 0.0 1000.

timestep    0.25

run   100000

unfix 3

undump 1

###################################### SIMULATION DONE

print "All done"
```

Argon Bombardment Script

```
#simulation of PKA damage 600 eV

units  real

boundary       p p p

atom_style  charge

read_data data.BCHAr

#######################################################hybrid potentials

#############################################################################ReaxFF
Potential

pair_style hybrid reax/c lmp_control lj/cut 11.0

pair_coeff  * * reax/c ffield.reax.hcb B C H NULL

##lj

pair_coeff  1 4 lj/cut 0.150885 3.4265
```

pair_coeff 2 4 lj/cut 0.115303 3.385

pair_coeff 3 4 lj/cut 0.13283 3.054

pair_coeff 4 4 lj/cut 0.23983 3.4

#mass

mass 1 10.811

mass 2 12.0107

mass 3 1.00794

mass 4 39.948

##
#########

velocity all create 2.0 893267 rot yes dist gaussian

neighbor 0.3 bin

neigh_modify   every 1 delay 0 check yes

restart 5000 restart.*.dens17

#Outputs and Run

thermo   100

thermo_style custom step temp pe etotal press vol pxx pyy pzz lx ly lz xy xz yz

dump   1 all custom 100 dump_total_600_eV.reax.amorphous_b4cH id type q x y z

fix   1 all qeq/reax 1 0.0 10.0 1e-6 param_bch.qeq

fix   4 all reax/c/species 1 1 10 species_600_eV.out element B C H Ar

fix   2 all nvt temp 2 2 100.0

timestep   0.05

run   5000

#Starting PKA run

#First unfix

unfix   2

##

group PKA1 id == 24001

group PKA2 id == 24002

group PKA3 id == 24003

group PKA4 id == 24004

group PKA5 id == 24005

group PKA6 id == 24006

group PKA7 id == 24007

group PKA8 id == 24008

group PKA9 id == 24009

group PKA10 id == 24010

group PKA11 id == 24011

group PKA12 id == 24012

group PKA13 id == 24013

group PKA14 id == 24014

group PKA15 id == 24015

group PKA16 id == 24016

group PKA17 id == 24017

group PKA18 id == 24018

group PKA19 id == 24019

group PKA20 id == 24020

group PKA21 id == 24021

group PKA22 id == 24022

group PKA23 id == 24023

group PKA24 id == 24024

group PKA25 id == 24025

###
####

velocity PKA1 set -0.093421963 0.4946317 -0.189871321 units box

velocity PKA2 set -0.139243516 0.347723005 -0.386185521 units box

velocity PKA3 set -0.399808671 0.231396691 -0.275767835 units box

velocity PKA4 set -0.514487782 -0.15490504 -0.027313939 units box

velocity PKA5 set -0.04688941 0.291898419 0.449484148 units box

velocity PKA6 set 0.235841762 -0.241773637 -0.418764221 units box

velocity PKA7 set 0.148291693 -0.28918918 0.428740591 units box

velocity PKA8 set 0.331223185 0.422913633 0.029573001 units box

velocity PKA9 set -0.201536712 -0.256911739 0.427572933 units box

velocity PKA10 set -0.331223185 0.370791828 0.205533267 units box

velocity PKA11 set -0.451201104 -0.227714197 -0.184399321 units box

velocity PKA12 set 0.37372317 0.04716364 -0.384117019 units box

velocity PKA13 set 0.465917886 -0.243794817 0.113683389 units box

velocity PKA14 set -0.47935762 0.240534278 -0.042412684 units box

velocity PKA15 set 0.435247611 0.306832639 -0.076501968 units box

velocity PKA16 set 0.456246172 0.285050829 0.00497558 units box

velocity PKA17 set 0.5376679 0.010226022 0.015746691 units box

velocity PKA18 set -0.07487452 0.027882498 0.532029767 units box

velocity PKA19 set 0.393465097 0.289130711 0.225893668 units box

velocity PKA20 set 0.338571622 -0.354569871 -0.221559845 units box

velocity PKA21 set 0.446018595 0.197370991 0.22704935 units box

velocity PKA22 set -0.111855581 0.46464158 0.247054312 units box

velocity PKA23 set -0.359989344 0.356232135 -0.181509338 units box

velocity PKA24 set -0.345816927 -0.224461303 0.345640099 units box

velocity PKA25 set -0.451201104 -0.227714197 -0.184399321 units box

##
#####

fix   2 all nve

run   100000

unfix 2

undump 1

################################### SIMULATION DONE

print "All done"

VASP INCAR for Structural Minimization

SYSTEM = B_C_H unit cell

  PREC = Accurate   # Low Medium High Normal Single Accurate, accuracy of the calculation, also increase memory, should be used Accurate if very accurate forces as phonons and second derivatives are required

  EDIFF= 1E-4   # EDIFF specifies the global break condition for the electronic SC-loop,can be decreased for accuracy

  ENCUT = 520   # Energy cutoff which sets Plane Wave cutoff in eV, ENMAX from POTCAR, For multicomponent choose the highest of all ENMAX_B=318.614, ENMAX_C=400.000,ENMAX_H=250.000, For volume relaxation increase ENCUT by 30%

  NGX = 60

  NGY = 60

  NGZ = 60

  NELM = 100   # No. of Electronic Minimization steps, sets the maximum number of electronic SC (selfconsistency) steps which may be performed, default 60, no need to change,

  NELMIN = 2   # specifies the minimum number of electronic SCF steps, no need to change, default 2.

  ALGO = Fast   # default Normal;specify the electronic minimisation algorithm; Normal-Davidson | VeryFast-RMMDIIS | Fast-Davidson &RMMDIIS and many more

  ISPIN=2   # 1-non spin polarized calculation 2-spin polarized calculations ;specifies spin polarization

  #Ionic Relaxation IOM:

  NSW = 100   # default NSW =0; max number of steps for IOM

  IBRION = 2   # -1 if NSW=1,0 , 0-MD, 1- quasi newton(usually the best choice) , 2-conj-grad, 3-damped MD (starting with bad guess); Algorithm for ionic relaxation same as algo for electronic relaxation

  NBLOCK = 1   # default 1, minimal computational overhead to determine the DOS and pair correlation function

  ISIF = 3   # 0 for IBRION=0 (MD) 1= position change,no shape& volume 2=no vol or shape change 3=position,cell & vol all change, 4=only no vol change, 5=vol& position no change, 6=Only positon no change 7= position &shape fix; determines whether the stress tensor

is calculated and which principal degrees-of-freedom are allowed to change in relaxation and molecular dynamics runs.

#Note: volume changes should be done only with an increased energy cutoff, i.e., ENCUT=1.3×max(ENMAX) or PREC=High

SMASS = -3   #controls the velocities during an ab-initio molecular dynamics run (IBRION=0)

LREAL = Auto   # .TRUE. or .FALSE. ;projection in reciprocal space, good for large cells

LWAVE = .FALSE. # .TRUE. or .FALSE. ;determines if WAVECAR is written

LORBIT = .FALSE.

LPEAD = .FALSE.

LCALCPOL = .FALSE.

LCALCEPS = .FALSE.

EFIELD_PEAD = 0.0 0.0 0.0

LEFG = .FALSE.

ISMEAR = -5   # default 1, N with N>0-MP method 0-Gaussian -1-Fermi -2-From WAVECAR -3-From INCAR -4-Tetrahedron no corr -5-Tetrahedron Blochl Corr ;Sets the smearing method for the Fermi level, Only for metals, Not for insulators and SM,

SIGMA = 0.2   # default 0.2, specifies width of smearing eV

PACKMOL Script for Building Initial Configuration

tolerance 2.0

filetype xyz

output data.XYZ

structure orthocarborane_unit.XYZ

  number 1000

  inside cube 0. 0. 0. 90

end structure

structure Ar.XYZ

  number 25

inside cube 0. 0. 0. 90

end structure

Script for NCPac.exe for Species Tracking

600_ev_100ps_10_ps.xyz   - name of xyz input file

1   - write out to screen

0   - read in surface data 5th column

1   - Periodic Boundaries

102 102 102   - x,y,z cell length (Angstrom) (used if in_pbc_option=1)

0.015339809   - g(r) spacing (Angstrom)

2.0 2.0 1.4 2.0 1.5 1.2   - NN cutoffs eg.1-1,1-2,1-3..,2-2,2-3,..,3-3,..

1 11 2   - First frame, last frame, frames between analysis

-10.0 -10.0 -10.0   - VMD output padded particle x,y,z location

0   - FILTER CLUSTERS

1   - Cluster size minimum below which removal

0   - SURFACE LAYER FIND & ANALYSIS

55.0   - Cone angle beyond which defines surface particles

3000   - No of points in spherical point distribution

0   - Q6 ORDER ANALYSIS

0.7   - q6(i).q6(j) min value to classify as similarily 'bonded'

1   - output Q6 ORDER for visualization

1   - STRUCTURAL UNIT ANALYSIS

1 0 0 1   - BH free raical

1 0 0 2   - BH2

1 0 0 3   - BH3 molecule

1 1 0 2	- B2H4
2 0 0 2	- CH2
2 0 0 3	- CH3
2 0 0 4	- CH4
3 1 0 0	- HB
3 0 1 0	- HC
3 0 0 1	- two time of H2 molecule

0	- FRACTAL DIMENSION ANALYSIS
30	- Maximum box division

0	- LINDEMANN INDEX
4	- No. of frame for time average
1	- output particle Lindemann index to xyz file